METROLOGY OF GaN ELECTRONICS USING MICRO-RAMAN SPECTROSCOPY

A Thesis
Presented to
The Academic Faculty

By

Thomas E. Beechem III

In Partial Fulfillment
Of the Requirements for the Degree
Doctor of Philosophy in Mechanical Engineering

Georgia Institute of Technology

December, 2008

Metrology of GaN Electronics Using Micro-Raman Spectroscopy

Approved By:

Dr. Samuel Graham, Advisor
School of Mechanical Engineering
Georgia Institute of Technology

Dr. Srinivas Garimella
School of Mechanical Engineering
Georgia Institute of Technology

Dr. Nazanin Bassiri-Gharb
School of Mechanical Engineering
Georgia Institute of Technology

Dr. Dan Green
Infrastructure Product Line
RFMD® Inc.

Dr. Alan Doolittle
School of Electrical and Computer Engineering
Georgia Institute of Technology

Dr. Suresh Sitaraman
School of Mechanical Engineering
Georgia Institute of Technology

Date Approved: November 13, 2008

PREFACE

The near ubiquitous presence of high speed internet access around the globe and the associated plunging capital costs of information has, as the distinguished author Thomas Friedman rightly stated, "flattened the world" [1]. Barriers such as geography, time, and language are eroding as the streaming of information incessantly laps against these previously impervious monoliths. No longer are individuals strictly beholden to the hierarchical structures of nation-state, university, and corporation but are instead empowered through access to, now, many of the same tools and resources previously available only as part of these structures. As a consequence, collaboration between groups seemingly orthogonal to one another just a decade ago is currently not only possible, but common. These collaborative processes, in turn, have moved work, progress, and innovation from centuries worn vertical "silos" spanning "top to bottom" and "bottom to top" into to a new hybridized horizontal coupling of effort in which the roles of the individual in the group, and even the group in general, are becoming ever less defined due to the pervasive interconnectedness of networks both social and literal.

A similar coupling and interconnectedness is occurring in physical structures as well due to the continually decreasing length and times scales at which devices are designed and operate. At these smaller scales, energy ceases being defined solely as thermal, mechanical, electrical, or chemical in origin but is instead a "total potential" defining the wavefunction of the system as a whole. In this situation, a single environment (e.g., thermal, electrical, etc.) becomes less and less relevant as it is the *interactions* between environments that determine the response as much as their individual presence.

Extending capability then necessitates understanding the coupling between environments as much as the environments themselves. With such a perspective, this effort moves away from exclusive "silos" of analysis towards a more inclusive approach centered on "flattening" the characterization of devices operating in this distinctly horizontal manner.

ACKNOWLEDGEMENTS

The nature of the technical at times diminishes the role of person and personality limiting the "who" in their production of the "what." Here at the Georgia Institute of Technology, and in particular the Woodruff School of Mechanical Engineering, I am thankful and appreciative that from the echo of my first footfall in Atlanta, I have been regarded first as a person with capabilities instead of a capability in the form of a person. This fact has manifested itself over and over again in my interactions, collaborations, and conversations with the faculty and staff, each of whom made me feel, in contrast to many of my fellow alumni who have "got out," that I am now pleasantly "leaving" Tech. Therefore, I think it is right and proper that I point out those whose time investment and effort have especially contributed to this positive sentiment.

First, I would like to recognize the work of Ms. Terri Keita and Glenda Johnson in the Woodruff School's Student Services Office who have tirelessly fielded and resolved all of my questions, concerns, and procedural uncertainties throughout my time here. Although they, no doubt, have numerous such inquiries each day, their conversation and banter always served as a pleasant pause and made my trek through the red tape of academia much more tenable. In addition, I would also like to thank the faculty with whom I have had the opportunity to develop a relationship including both those serving as part of this committee - Dr. Nazanin Bassiri-Gharb, Dr. Alan Doolittle, Dr. Srinivas Garimella, and Dr. Suresh Sitaraman - and those whom I have gotten to know in a more informal fashion - Dr. Peter Hesketh, Dr. Michael Leamy, Dr. Farrokh Mistree, Dr. Wayne Whiteman, and Dr. Zhoumin Zhang. I recognize each of them for their

dedication, work ethic, and passion for the topics they pursue as well as their willingness to invest a portion of their very limited time in an incessantly questioning, overly wordy, and incorrigibly energetic graduate student. I earnestly thank each of them.

Over a year and a half ago, I had the opportunity to demonstrate our group's Raman capabilities to Dr. Dan Green of RFMD® Inc. Little did I believe at the time that this demonstration would grow into a collaboration that would evolve into the great bulk of my thesis. I am then indebted and thankful for Dan's willingness to work so closely with us throughout the majority of these past months. He has been constantly available for questions, free with his resources, and extremely patient as we dove into questions more in line with academic inquiry than those centered solely on his objectives. I have enjoyed working with, and getting to know him, while at the same time appreciating the insight he has provided into research within the industrial setting.

I did not so much decide to attend Georgia Tech as I chose to work under Dr. Samuel Graham. I have been constantly affirmed in this decision throughout the three and a half years of my time here. He has been constantly reasonable, open, and available. Willing to debate, open to discussion, and trusting in his graduate students, I cannot imagine working, or wanting to work with, anyone else. I will always be grateful for not only the independence he allowed, but more importantly, his ability to motivate while at the same respecting the delicate balance needed to fulfill each of my roles as student, husband, son, and brother.

The wealth of talent, in personality as well as ability, within the student body here at Tech is astounding. From my first days, I have been continually amazed at the interplay between the graduate students residing in the Love Building. Questions fly about,

ranging in topic from politics and policy to solid state and quantum theory. Opinions are valued, substantiated ones even more so. Laughter is common, as is teamwork. Rivalry between students and research groups has not been apparent and for all these things I am thankful. Therefore, I think it is right that I recognize each of those personalities, both in our own group and those outside, who have helped in weaving such a splendid tapestry of my daily routine over this season of my life: Adam Christensen (who deserves special recognition for both his simulation expertise and friendship that have undoubtedly enhanced this study), Ashante Petty, Abe Greenstein, Andrew Cannon, Ashish Sinha, Brent Nelson, Carter Dietz, Erik Sunden, Joe Charest, Jungchul Lee, Konrad Rykaczewski, Keunhan Park, Mark Meacham, Marcus Eliason, Mark Gleva, Minseok Ha, Namsu Kim, Robert Cross, Soumyadipta Basu, Sukwon Choi, Vishwanath Subramaniam, Yeny Hudiono, and Yongjin Kim.

Additionally, I would like to single out - even though he will likely glower at me for doing so - Roderick Jackson. Roderick and I have traveled complementary paths during our time at Tech - interviewing with Dr. Graham simultaneously, arguing during Quals, and eventually sharing an office. All the while, Roderick has constantly pushed me to improve myself through his example, probing questions, discussion, and input on any topic. I consider it an honor to call him a friend and colleague.

As this document serves as the culmination of my formal education, I would like to recognize a couple of teachers who have especially aided me throughout the journey. Beginning at a small Catholic grade school in Kentucky, this trip began in earnest when I was given a mathematics textbook in 5th grade by Mrs. Linda Bolan and told to go to the cafeteria by myself and "figure it out." I am thankful not only for the confidence she had

in me to actually go and do just this, but also for the opportunity to learn how to teach myself and think apart from the group - skills that I now use each and every day. Subsequently at Covington Catholic High School, I only realized how much I enjoyed these challenges through the dualistic excitement and logic that Mr. Charles Parrott brought with him each day to class. His energy and ability to translate the abstract of mathematics into matter of fact practicalities allowed me to see that the questions surrounding engineering were ones that I indeed found interesting. And yes Mr. Parrott, much of calculus, though clearly not all, does now seem as easy as basic algebra.

Personally, I have been blessed numerous times over with tremendous support during my graduate studies both back home and here in Atlanta. I am surrounded by a marvelous family that said it was "OK" to leave at an extremely hard time. Thank you to Caleb, Michaela, Troy, John, Kelly, Paula, Irwin, and my mom, Marianne, for being happy at my opportunity rather than seeing my move to Atlanta as an act of escape. Thanks to each one of you for being so willing to share yourselves through the phone rather than face to face. I appreciate and value both the whole of our family and every person who makes it up. A second helping of thanks goes to my brother, John, who subjected himself to learning more about crystal lattices than he ever wanted to know while proofreading this document. His effort and involvement has, without question, improved my work and I am extremely happy to have had him with me during this process. In addition, my parents deserve special recognition for instilling in me, from my first day of school, the intense value that is education. Thank you to my mom, in particular, for the huge sacrifices she made to allow me to attend not only the best

schools but also the ones I wanted. A special nod to my dad for is incessant belief in me and his continual encouragement that stays with me even now.

Here in Atlanta, our lives have been infinitely enriched by the home that we've found at Trinity Vineyard. Trinity has been our family here in the south and one that we will miss dearly. Thanks to each of you for showing us what a Christian community can and continues to be. In particular, our lives have been significantly touched by the friendship and love of you: Matt, Margo, Anna, Jill, and now Micah. I cannot tell you how much your sharing, friendship, help, and hospitality has meant and the degree to which you are valued. You have brought a special joy to Eryn and myself, and in that, you will always hold a central part of our hearts.

Finally, I owe an immeasurable debt of appreciation to my wife Eryn who uprooted her life with me over three years ago and left all that was easy, normal, and comfortable. Now it is at this point in most theses that the phrase "could not have done this without you" is inserted and so it is. When I first started reading other theses during my research (I always peruse the acknowledgement section: guilty pleasure), I found the phrase a bit stale, formulaic, and empty. Another sentence easily banded behind your "appreciation of the committee members' time and guidance." Yet because of my experience, I now realize that the phrase is anything but empty and lifeless, but rather is so universally applied because it is so unmistakably real. You really cannot do this without someone.

And for me, Eryn is that someone. She has taken on the demands of our household, our friends, and even our family to let me work, to be consumed with thoughts about work, to relax when I'm not at work, all the while being subject to the emotions of not only the finishing of one job but the commencement of another. I will never be able to

thank or love her enough for the limitless worth that are these things. She is of unbounded value to me, and I am undeniably fortunate to share my life with her.

TABLE OF CONTENTS

LIST OF TABLES

LIST OF FIGURES

NOMENCLATURE

A'	Stress free calibration of peak position with temperature
$AlGaN$	Aluminum Gallium Nitride
b	Concentration of a species in the virtual crystal
C	Calibration factor relating Stokes to anti-Stokes intensity ratio to temperature
C_{VC}	Specific heat of virtual crystal
c_{VC}	Velocity of a phonon mode in virtual crystal
D	Calibration constant relating stress to the shift in the Stokes Peak
D'	Depth of interface
DMM	Diffuse Mismatch Model
d_{AlGaN}	Thickness of AlGaN barrier layer
d_{kij}	Piezoelectric modulus tensor
E	Electric Field/Elastic Modulus
e	Elementary electron charge (C)
e_L	Polarization vector of incident radiation during a Raman measurement
e_s	Polarization vector of scattered radiation during a Raman measurement
E_F	Fermi Level
GaN	Gallium Nitride
G	Calibration constant linking temperature and Stokes to anti-Stokes intensity ratio
H	Calibration constant linking temperature and Stokes to anti-Stokes intensity ratio

h_{int}	Thermal boundary conductance
HEMT	High electron mobility transistor
I-V	Current-Voltage device characteristics
I_{AS}	Anti-Stokes Intensity
I_S	Stokes Intensity
K	Spring constant
K_{VC}	Thermal conductivity of the virtual crystal
K_1	An arbitrary Constant
K_2	An arbitrary Constant
k_B	Boltzmann Constant
LPP	Longitudinal optical phonon-plasmon mode
$\overline{m}$	Reduced mass
M	Parameter describing the relative importance of lateral heat losses to axial conduction in Si Microheater
MEMS	Microelectromechanical systems
MOCVD	Metal organic chemical vapor deposition
n	Number of data points in a measurement
n_s	2DEG concentration (cm^{-2})
N_o	Number of phonons at equilibrium
nGaN	n-type doped gallium nitride
P	Dipole moment of a material
p	Constant of phonon deformation potential
P_{max}	Maximum power delivered by a transistor device while operating in class-A conditions
pGaN	p-type doped gallium nitride

PDP	Phonon deformation potentials
Q	Parameter describing the relative importance of Joule heating to axial conduction in Si Microheater
q	Constant of phonon deformation potential
$q^{'}$	Time dependent change in lattice spacing
q_o	An arbitrary amplitude of vibration
r	Constant of phonon deformation potential
R	Raman tensor
S	Scattering efficiency
S_{ijkl}	Elastic compliance tensor
t	Time
T	Temperature
TBC	Thermal boundary conductance
T_o	Reference temperature
u	Displacement
$\ddot{u}$	Acceleration
V_B	Breakdown voltage
$VCDMM$	Virtual Crystal Diffuse Mismatch Model
V_{Kn}	Knee voltage
ΔE_C	Conduction band offset

Greek Characters

α	Electrical polarizability of a material/Thermal expansion coefficient of material
α_o	Electrical polarizability of the material at equilibrium lattice spacing
α_a	Thermal expansion parallel to a-axis of crystal

α_c	Thermal expansion parallel to c-axis of crystal
α_{1-2}	Transmission ratio between side 1 and 2
β	Phonon deformation potential linking a change in peak position to strain
δX	95% Confidence interval for an arbitrary component, X
Λ_{VC}	Mean free path of a phonon mode in the virtual crystal
ε	Strain
ε'	Dielectric constant
ε_o	Permittivity of free space (F/m)
ε_D	Energy of species that interacts with the excited carrier in Raman event
ε_i	Incident energy of radiation before scattering with a surface
ε_g	Ground state energy of a species before scattering
ε_L	Excited energy of a carrier after scattering with incident radiation
ε_m	Intermediate energy state of excited carrier during a Raman event.
ε_{ij}	Strain tensor
$\Delta\varepsilon$	Energy band
$e\phi_B$	Schottky barrier height
Γ	Linewidth of the Raman signal
$\hbar$	Planck's Constant divided by 2π
λ	Eigenvalue of the secular equation
σ_{pol}	Polarization due to both spontaneous and piezoelectric effects (C/m^2)

σ_{st}	Standard deviation of a data set
σ_{kl}	Stress tensor
τ	Scattering time of a phonon mode
ω	Frequency
ω_o	Equilibrium peak position
ω_R	Frequency of incoming radiation
$\omega_{\max}$	Cut-off frequency of a Debye solid
ω_p	Arbitrary frequency of vibration
ω_{tot}	Frequency of a vibration subject to both temperature and stress
ω_s	Frequency of a vibration after being subjected to stress
2DEG	Two-Dimensional Electron Gas

SUMMARY

Possessing a wide band gap and large break down field, gallium nitride (GaN) is of interest for a host of high power, high frequency applications including next generation cellular base stations, advanced military radar, and WiMAX networks. Much of this interest stems from the continued development of the AlGaN/GaN high electron mobility transistor (HEMT) that is capable of operating at sizable power densities and switching speeds. The same fields responsible for this performance, however, also elicit acute device heating and elastic loads. These induced thermomechanical loads limit both performance and reliability thus necessitating continued improvement in the management and characterization of the coupled environments. In response, this study establishes a new implementation of Raman spectroscopy capable of simultaneously measuring the operational temperature and stress in a HEMT using only the Stokes response. First, the linewidth (FWHM) of the Stokes signal is utilized to quantify the operating temperature of a HEMT independent to the influences of stress. Second, a new method, incorporating the use of the linewidth and peak position in tandem, is developed to estimate the biaxial thermoelastic stress that arises during device operation. With this capability, the HEMT's resultant load is assessed, highlighting the large role of the residual stress on the total mechanical state of the device. Subsequently, this same linewidth is leveraged to identify the distinct effect that electrical carriers have on the thermally relevant decay of longitudinal optical phonon modes. Further investigation of the lattice transport then concludes the study by way of an analytical treatment describing the significant influence of interfacial disorder on the energy transport at GaN/substrate boundaries.

CHAPTER 1

INTRODUCTION

1.1 Gallium Nitride (GaN) Power Electronics, Temperature, and Stress

Due to its wide bandgap, large breakdown field, and high electron mobility, gallium nitride (GaN) is extremely attractive for an array of both high power and high frequency applications [2]. With both commercial and military applications totaling a worldwide market of $4 billion dollars in 2006 alone, GaN is being developed for a variety of utilizations ranging from phased array radar systems, solid state light sources, wireless base stations, and even WiMAX broadband [3-7]. Of particular interest is the continued development of the AlGaN/GaN high electron mobility transistor (HEMT) that is capable of both large power densities (>30 W/mm) and switching speeds (>160 GHz) [8, 9]. Although these performance metrics illustrate the potential of GaN devices, widespread realization of their use has been limited, in part, due to reliability concerns [10]. These reliability concerns stem from degradation mechanisms that significantly reduce the output power of the transistor within its first hours of operation [11-15]. While the degradation mechanisms themselves are not unequivocally specified, and in fact are the subject of much research, there is evidence indicating that increases in either temperature or stress during operation negatively impacts not only this rate of failure but so too the overall performance of the device [16-21].

The dependence of the AlGaN/GaN HEMT to the dual effects of both temperature and stress evolves from the nature of the material system itself and, in particular, the strength of its piezoelectric response. In such a device, shown schematically in Figure 1, a thin layer of aluminum alloyed gallium nitride (AlGaN) is grown atop a thicker region of GaN causing strain to develop due to the mismatch in lattice constants between the materials. As each of the materials demonstrates a large piezoelectric response, this strain induces a sizable polarization within each layer. The total polarization of the layers is then augmented due to the presence of a spontaneous contribution stemming from the lack of inversion symmetry in the wurtzite crystal arrangement of both the AlGaN and GaN [23]. In response to the entirety of the polarization, a macroscopic electric field is formed causing free carriers to be transported to the region of minimum potential in the system. It is at the interface between the two layers that this minimum occurs and as a consequence free carriers aggregate therein forming what is known as a two-dimensional

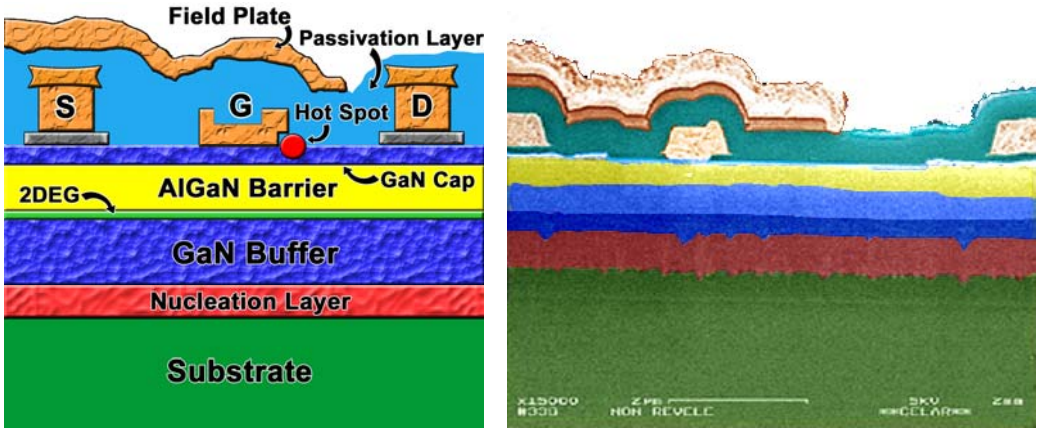

Figure 1. Schematic representation (left) and an enhanced SEM image (right) of a typical GaN based HEMT (Note: thicknesses are not to scale in either portrayal). Piezoelectric and spontaneous polarizations present in the AlGaN and GaN layers induce free carriers to the interface of these layers forming the 2DEG that gives rise to the device's substantial capability. (SEM figure adapted from work of Burgaud *et al.* [22])

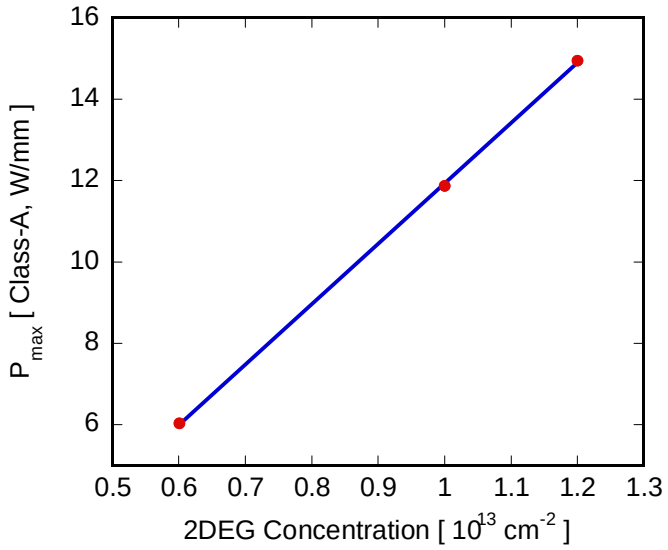

Figure 2. Dependence of the maximum power on the concentration of carriers in the 2DEG of an AlGaN/GaN HEMT. Results are calculated based on the published results of Wu *et al.* [26, 27] indicating that increases in 2DEG concentration correlate directly to heightened device performance.

electron gas (2DEG) [24]. In a GaN system, these polarizations are comparatively large causing the carrier concentration within the newly formed 2DEG to be substantial ($\sim 10^{13}$-10^{14} electrons/cm^2) [24, 25]. Since the electronic performance of a device is limited only by the number of carriers and their ability to be transported, these high concentrations, and the large polarizations causing their formation, are central to the capability of the device. Furthermore, those parameters affecting these polarizations, namely the temperature and stress, will then be a major determinant in the performance of the HEMT as well.

Qualitatively, the dependence of device performance on temperature and stress may be illustrated through consideration of three representative HEMTs fabricated by Wu *et al.* [26, 27] having varying aluminum concentrations in the barrier layer. By increasing the amount of aluminum in the AlGaN layer, the degree of both the spontaneous and

piezoelectric polarization is enhanced, thereby heightening the 2DEG concentration in the channel. Through comparison of the reported current voltage characteristics (I-V) of these devices, the maximum power of the device is observed to scale with the level of carrier concentration in the 2DEG as is seen in Figure 2 [28] and further supported by the simulations of references [29] and [30]. In light of these results, much of the device's dependence upon temperature and stress may then be demonstrated solely through calculation of the 2DEG's concentration as a function of these parameters.

To facilitate calculation of the 2DEG's concentration as a function of temperature and stress, the analytical predictions of Ambacher *et al.* [25, 31] are employed. Using this method, the 2DEG concentration is predicted according to the expression given below:

$$n_s = \frac{\sigma_{pol}}{e} - \left(\frac{\varepsilon_o \varepsilon'}{d_{AlGaN} e^2} \right) \left(e\phi_B + E_F - \Delta E_C \right) \tag{1}$$

where n_s is the 2DEG concentration in units of carriers per cm^2, σ_{pol} is the total polarization including both spontaneous and piezoelectric effects, and e is the elementary electron charge. The final term accounts for those factors resisting the formation of the 2DEG where ε_o and ε' are the absolute and relative permittivity, respectively. d_{AlGaN} is the thickness of the barrier, $e\phi_B$ is the Schottky barrier located at the gate contact of the transistor, E_F is GaN's Fermi level, and finally, ΔE_C is the conduction band offset between the GaN and AlGaN layers. Using this relation and the parameters reported in reference [32], the effect of stress on the 2DEG concentration was calculated by imposing an equivalent "external" strain on the materials such as that which could occur due to compromised packaging or mounting procedures. The application of the simulated compressive stress reduces the concentration of the 2DEG (Figure 3) to such an extent

that the maximum power (P_{max}) may be reduced by up to 3% with just 210 MPa of load, thus emphasizing the distinct coupling of the electrical and mechanical effects on the performance of the HEMT.

Coupling of the thermal and electrical effects must be considered as well due to the 2DEG's significant dependence upon temperature. Using a similar procedure to the one described above, the effect of elevated temperature on the channel concentration was examined by assuming thermomechanical coupling of the device to a silicon carbide (SiC) substrate while incorporating the temperature dependent properties given in reference [33]. Once again, the examined parameter (temperature) has a distinct effect on the 2DEG concentration and hence the device performance as well. However, unlike that seen with respect to stress, assuming no relaxation occurs in the AlGaN barrier, a heightened thermal load causes an increase in the 2DEG concentration due to the more acute tensile strain in the alloyed layer, which arises with thermal expansion. Nonetheless, the result indicates a distinct coupling of the thermal environment to the

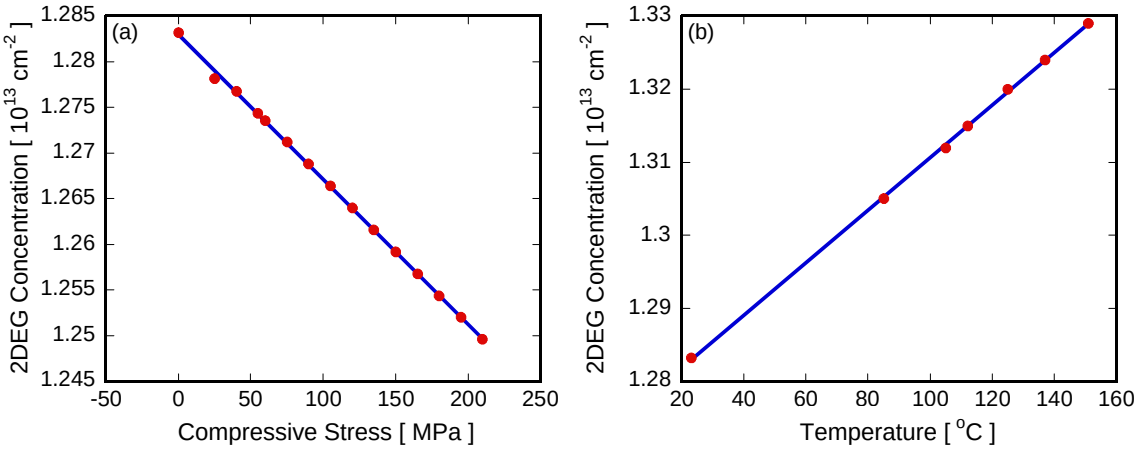

Figure 3. The dependence of the 2DEG concentration to the effects of (a) compressive stress and (b) temperature. Both temperature and stress significantly change the concentration thereby altering device performance due to their presence.

electrical characteristics of the device. This fact, taken in conjunction with the observed mechanical dependence, highlights the inherent and critical coupling of each type of physical phenomena in an AlGaN/GaN high electron mobility transistor.

In view of these conclusions, HEMT operation must be viewed in the guise of a "3-D" coupled field feedback loop in which, as was illustrated, the electrical characteristics of the device are determined by the thermo-mechanical conditions. The thermo-mechanical environment, however, is also primarily determined by the electrical output of the device due to joule heating, thermoelastic, and inverse piezoelectric effects, each of which evolve with current flow. Thus, when these results are taken in their totality, each environment acts to influence the others, and therefore, operation must be viewed in the "loop" of their coupling. As a consequence, it is this interplay between temperature (thermal), stress (mechanical), and electrical output that will inherently determine the capability, potential, and optimal performance of an AlGaN/GaN HEMT.

Not only is the level of performance in the transistor influenced by the thermo-mechanical environment but so too is the device's long term viability. For example, the reliability of AlGaN/GaN transistors is inversely related to the device's operational temperature as degradation has been observed to follow an Arrhenius relationship [34]. Stress plays a role in the degradation as well, owing to defects that form at a rate proportional to the magnitude of the elastic load [12, 35, 36]. Reliability then, like performance, is intimately linked to the level of temperature and stress in the system.

Owing to this dual dependence of both performance and reliability to the level of temperature and stress in the HEMT, it is imperative that these parameters be accurately quantified and measured during the operation of the device. The measurement and

prediction of these parameters is not trivial, however, due to the device's small length scales (~1 μm) as well as the large gradients and coupled nature of the phenomena being measured. Nonetheless, it remains critical that techniques be developed that meet these challenges in order that device performance be monitored, mean time to failure predicted, simulations verified, and mechanisms limiting reliability be understood. In response, this study develops such methods, thereby allowing for fresh insight into the operation of the AlGaN/GaN HEMT, in addition to providing a new tool to be incorporated in the analysis of both GaN and other material systems. To properly frame the approach, subsequent sections first provide context into the scope of the problem through a discussion of the theory behind both temperature and stress measurements along with descriptions of those techniques most often used to analyze microdevices. Thereafter, the utility of Raman spectroscopy in the analysis of microdevices, and GaN devices in particular, is introduced. With this motivation, the chapter ends with an outline of the study as a whole.

1.2 The Measurement of Temperature in GaN Devices

1.2.1 Theory

At its most fundamental level, temperature is a measure of average atomic motion or energy. Direct monitoring of this motion is intractable and hence the overwhelming majority of temperature measurements are instead indirect in nature. These indirect methods monitor not the temperature itself, but rather, a separate temperature dependent phenomenon. The dependent phenomena, in turn, arise as the major energy carriers, photons, electrons, and phonons; themselves have a statistical population dependent upon

the temperature. Thus, it is not surprising that oftentimes the nature of their interaction is temperature dependent as well. As a consequence, mensuration of temperature most often centers on the monitoring of the interaction between these energy carriers.

In semiconductor devices, these interactions are observed most often in one of three distinct manners, namely, through direct contact of a probe with the device, or in the measurement of the electrical, or optical response of the device during operation [37]. Regardless of the manner employed, the ***ideal*** temperature measurement has a spatial resolution capable of identifying even the smallest temperature gradients while simultaneously having a temporal resolution fine enough to capture the entirety of salient transient behavior. In addition, the measurement itself should have little or no effect on device function while being easily utilized in a diverse range of packaging architectures. As there is no single technique capable of meeting each of these criteria, semiconductor characterization is then a balance of amenities and liabilities as is shown in the following sections.

1.2.2 Direct Contact Techniques of Temperature Measurement

Contact methods capitalize upon the thermal equilibration that occurs between a probe and the material of interest in order to investigate the temperature of a device. Through proper calibration of a particular thermal dependence of the probe, a dependence which may be optical in nature (liquid crystal thermography) but is most often electrically derived (e.g., thermocouple/Seebeck Effect), temperature is measured based on the heat flow between sample and probe [38]. Direct contact measurements range in complexity from use of a standard thermocouple to the incorporation of advanced AFM tips capable of sensing temperature with nanometer resolution [39]. For GaN devices,

the small resolution of the AFM approach has allowed for the examination of the effect of both biasing conditions and diamond substrates on temperature evolution [40, 41]. The approach is limited spatially only by the tip size and is ideal for mapping operations, however, its temporal resolution is constrained by the heat transport dynamics between the tip, surrounding medium, and surface. Furthermore, scanning probe methods are directly applicable only when the layer of interest is accessible. With respect to AlGaN/GaN HEMTs, direct contact with the active, heat generating, region is not possible due to the presence of a passivation layer placed atop the device [42]. If this is the case, temperature of the active region may only be acquired through interpretation of the heat flow through this passivation layer. Interpretation is most difficult in this situation, however, due to the complexity of the heat transfer environment in which the tip/interface dynamics, detailed material properties of the layers, and the interfacial heat transfer each act to complicate the analysis. An excellent review of this type of metrology was given by Majumdar in 1999 [43].

1.2.3 Electrical Techniques of Temperature Measurement

While direct contact methods rely on heat transfer to occur until two surfaces are isothermal, electrical methods rely on the changes in the transport of electrons to probe the temperature of the material. In GaN devices, this approach has capitalized upon such phenomena as the temperature dependence of the Schottky barrier and dispersions in the DC I-V characteristics of the device to quantify temperature [17, 44, 45]. Due to the high transport speeds of the electrons, superb temporal resolution is easily obtainable; however, spatial resolution is limited as the acquired data averages between electrical contacts. Yet as only circuit components are needed to obtain a measurement, this type

of measurement is well suited for applications where packaging makes the active surfaces of the device inaccessible.

1.2.4 Optical Techniques of Temperature Measurement

Optical methods monitor the temperature dependence of photons either emitted (spontaneous or stimulated) or reflected from the region of interest. This thermal dependence arises as several parameters affecting this radiation, e.g., the emissivity, reflectivity, as well as the electronic and lattice band structure, are themselves temperature dependent. This has led to a host of different measurement techniques including pyrometry, interferometry, thermoreflectance, and Raman spectroscopy to name just a few of the many methods utilized in the analysis of microdevices. An excellent review over the range of these techniques is provided by Zhang [46].

As the wave nature of the radiation serves as the probe in these methods, most far field applications have spatial resolutions limited only by the wavelength of the monitored photons ranging from 1 μm for visible light to nearly 10 μm for infrared imaging techniques [47, 48]. Theoretically, the temporal resolution of these techniques is limited only by the interaction time between the device and the photons, ~1 fs, however, in practice the resolution is limited by the experimental equipment employed with the best reports being on the order of 20 fs [49]. These methods also rely on an optically viable surface for measurement, a stipulation which is not always fulfilled in multilayered and packaged devices.

In the measurement of GaN devices, optical methods, particularly infrared and Raman thermography, are among the most frequently implemented techniques to measure temperature due to their non-invasive nature and relative ease of implementation [50]. Infrared thermography takes place by first mapping the emissivity of the device through calculation of the radiation leaving the surface at a known temperature. Through incorporation of this acquired emissivity, the temperature of the device during operation may then be deduced via quantification of the emitted radiation acquired from different regions of the device during operation [51]. Particularly advantageous in the measurement of AlGaN/GaN HEMTs, the technique allows for the entirety of the device to be measured simultaneously thereby allowing for a full two dimensional temperature map of the device (see Figure 4) to be acquired in a small amount of time.

Despite the allure of these maps, infrared thermography is limited as the resolution of the technique is constrained to ~5 μm due to the wavelength of the probing infrared radiation. In addition, GaN is transparent to this same infrared radiation and, as such, the signal stemming from this region of interest becomes convoluted with the thermal

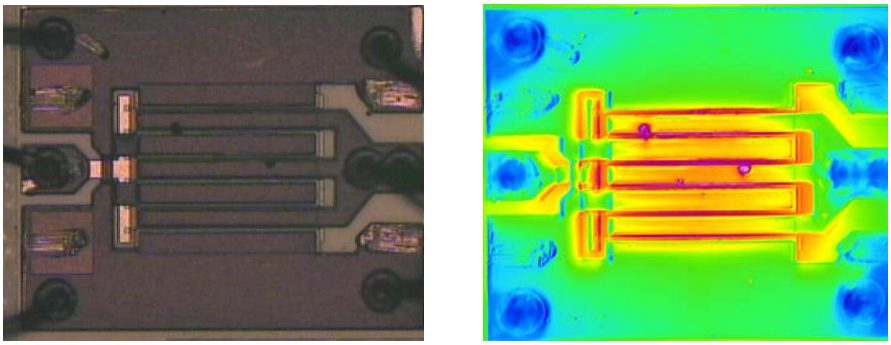

Figure 4. Optical micrograph (left) of an AlGaN/GaN HEMT and its associated temperature distribution during operation (right) as acquired using infrared thermography.

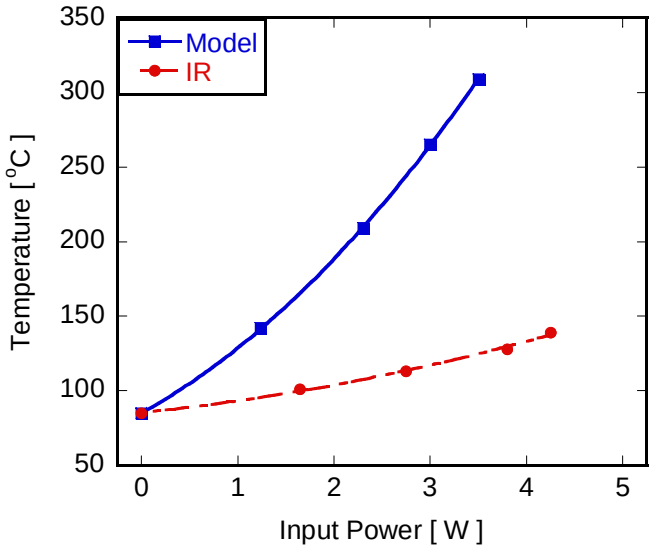

Figure 5. Comparison of temperature in a GaN based transmission line measurement (TLM) device obtained through a finite element model and infrared thermography. Due to the limited spatial resolution and the transparency of GaN in the IR, infrared based measurements oftentimes under predict the magnitude of the temperature [52].

signature of the substrate layers underneath. Due to these considerations, the quantitative values derived from infrared thermography often underestimate the temperature (see Figure 5), thus limiting the technique to qualitative comparisons rather than quantitative investigation [50, 52]. To meet this quantitative deficiency, Raman spectroscopy has been incorporated by several researchers in the investigation of AlGaN/GaN HEMTs due to the technique's ability to more accurately measure temperature with nearly 1 μm resolution [53, 54]. As this method is the chief topic of this study, its further discussion will be left for subsequent sections.

1.3 The Measurement of Stress in GaN Devices

1.3.1 Stress Measurement Theory and Technique

Like the investigation of temperature, the measurement of stress in microdevices is not a directly observable phenomenon. Rather, the observed variation in material response is, in actuality, a response to the material's level of strain. A secondary step must then be undertaken to transform the acquired level of strain into its associated level of stress. This translation of strain into stress frequently occurs either through analytical and numerical methods (e.g., FEA) or the direct calibration of the observed response to strain at a known level of stress [55]. Nonetheless, these measurements rely on the acquisition of strain and then its translation to stress while implicitly resting on the supposition that the entirety of the observed strain is due to elastic sources alone. In GaN devices, however, this supposition is tenuous as both thermal expansion and piezoelectric induced strain are present in addition to elastic effects during operation.

Regardless of these complications, measurements of strain involve the close monitoring of deformation. In order to capture the relevant aspects of this deformation in GaN based electronics, optical techniques are often utilized due to the probing radiation having a wavelength on par with that of the device. These optical techniques may then be divided into two large classes in which the strain is acquired either *ex* or *in situ* to the actual device. In *ex situ* measurements, strain is quantified through minimal interaction with the sample as the reflection of light tracks the movement of one point relative to a reference. Both optical profilometry and interferometry adhere to this basic principle and have been employed in the characterization of GaN films and devices [56, 57]. However, due to the complications associated with increased temperature and the presence of

piezoelectric induced strains in GaN microelectronics, these techniques have been employed only in the quantification of residual stresses present in the material after processing while no analysis has taken place during actual device operation.

In situ techniques, on the other hand, do not monitor positional differences but instead alterations in the scattered light interacting with the sample. This change in scattering occurs due to changes in the interatomic potential that arise when atoms move relative to one another during deformation. With this change in interatomic potential, dispersions of both the electrons and crystal vibrations are modified. As the scattering of the incident radiation is directly dependent upon these dispersions via Bragg's law, their perturbation thus causes a subsequent variation in the scattered radiation thereby allowing for an estimation of the strain [58]. X-Ray diffraction, photoluminescence, as well as the oft applied Raman spectroscopy are each derived from this principle and have been utilized in the mechanical characterization of GaN films and devices [59-62]. Similar to *ex situ* techniques, however, temperature and piezoelectric contributions compromise these methods as well, thus limiting their implementation solely to the quantification of residual, rather than operational, stress levels.

1.4 Raman Spectroscopy to Measure Temperature and Stress

While there is no such probe ideally suited to the analysis of AlGaN/GaN HEMTs, Raman spectroscopy is at the forefront of temperature and stress measurement for this device class due to the technique's ability to non-invasively analyze the material on a length scale in line with that of the transistor. The technique has been utilized to investigate the magnitude and distribution of both temperature and residual stress due to a variety of factors including device geometry, substrate, and defects [50, 56, 57, 63-69].

Due to this broad swath of capability along with its frequent implementation, the technique must be considered central to the characterization of AlGaN/GaN HEMTs. Consequently, further discussion of Raman spectroscopy, its principles and methods of implementation is warranted.

1.4.1 Physical Basis of the Raman Technique

Similar in approach to any optical method, Raman spectroscopy takes place through bombardment of a surface with radiation while concomitantly observing the photonic energy reaching a detector. In Raman spectroscopy, the energy that reaches the detector has been "changed" through scattering with the sample volume. The nature of this scattering, and hence the degree to which the radiation is "changed," depends upon the distribution of phonons and electrons within the material lattice. These distributions, in turn, are both temperature and stress dependent making the interactions, and hence the resulting Raman scattered radiation, dependent upon these parameters as well. Thus the key to examining the temperature or stress dependence of the Raman scattered radiation is to understand the interaction between the incident radiation and the material lattice.

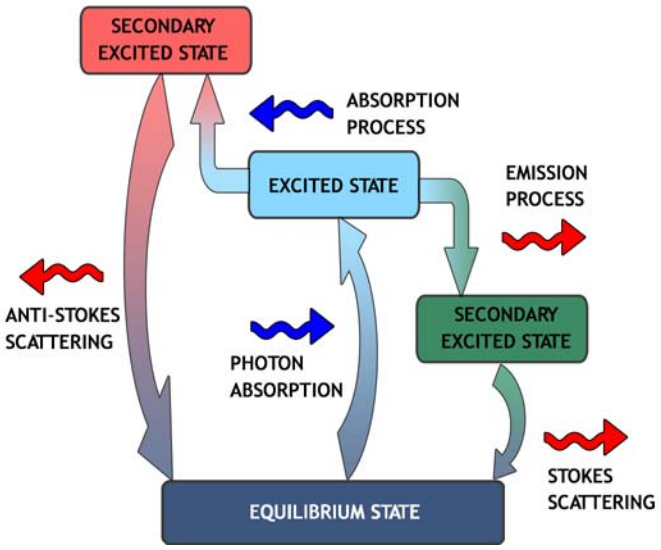

Figure 6. Process flow diagram of Raman scattering where 3 separate events give rise to the detected inelastic scattering. Through observation of the change in radiation incident and emitted from the surface, deductions can be made with respect to the interaction of the light with the crystal lattice.

Upon impingement of incident radiation to a surface, a photon with energy ε_i, may either be reflected, absorbed, or transmitted. In Raman spectroscopy, the concern rests solely upon an interaction in which this photon is absorbed by either an electron or, in a dramatically more unlikely case, a phonon [70]. As part of this event, the absorbing species (i.e., the electron or phonon) is promoted from its equilibrium state of energy, ε_g, to an excited virtual state of energy, ε_L, resulting in a non-equilibrium distribution of the excited entity (see Figure 6). Seemingly simultaneously, thermalization will occur whereby this excited entity will "relax" back to its equilibrium state and distribution. Most often this occurs directly thereby inducing the "re-emission" of a photon of energy equal to that which was incident (ε_L-ε_g= ε_i) in a process known as Rayleigh scattering.

In a small statistical subset of these occurrences, however, an intermediate event takes place by which the excited species either absorbs or emits an additional energy carrier (i.e., phonon or electron) in the process of thermalizing as is shown in Figure 6 . As a consequence of this intermediate event, the types of which are summarized in Table 1, the excited species moves to a secondary non-equilibrium virtual state of energy ε_m that is unequal to either its original ground (ε_g) or excited level (ε_L). Upon relaxation of the excited entity from energy ε_m to its original equilibrium energy $\varepsilon_{g,}$ a "new" photon of energy $\varepsilon_m - \varepsilon_g = \varepsilon_f$ will be emitted. Due to the intermediate reaction, the emitted photon

Table 1. Scattering cascade giving rise to the Raman effect. Although events numbered 3 through 6 are possible, it is generally assumed that events 1 and 2 significantly dominate [70].

	Event 1	Event 1 $\Delta\varepsilon$	Event 2	Event 2 $\Delta\varepsilon$	Event 3	Event 3 $\Delta\varepsilon$	Scattering Type
1	Photon (ε_i) absorption by electron	$\varepsilon_L - \varepsilon_g = \varepsilon_i$	Phonon (ε_D) absorption by electron	$\varepsilon_L+\varepsilon_D=\varepsilon_m$	Electron relaxation and photon emission	$\varepsilon_m - \varepsilon_g = \varepsilon_f$	Anti-Stokes
2	Photon (ε_i) absorption by electron	$\varepsilon_L - \varepsilon_g = \varepsilon_i$	Phonon (ε_D) emission by electron	$\varepsilon_L - \varepsilon_D=\varepsilon_m$	Electron relaxation and photon emission	$\varepsilon_m - \varepsilon_g = \varepsilon_f$	Stokes
3	Photon (ε_i) absorption by phonon	$\varepsilon_L - \varepsilon_g = \varepsilon_i$	Phonon (ε_D) absorption by phonon	$\varepsilon_L+\varepsilon_D=\varepsilon_m$	Phonon relaxation and photon emission	$\varepsilon_m - \varepsilon_g = \varepsilon_f$	Anti-Stokes
4	Photon (ε_i) absorption by phonon	$\varepsilon_L - \varepsilon_g = \varepsilon_i$	Phonon (ε_D) emission by phonon	$\varepsilon_L-\varepsilon_D= \varepsilon_m$	Phonon relaxation and photon emission	$\varepsilon_m - \varepsilon_g = \varepsilon_f$	Stokes
5	Photon (ε_i) absorption by phonon	$\varepsilon_L - \varepsilon_g = \varepsilon_i$	Electron (ε_D) absorption by phonon	$\varepsilon_L+\varepsilon_D=\varepsilon_m$	Phonon relaxation and photon emission	$\varepsilon_m - \varepsilon_g = \varepsilon_f$	Anti-Stokes
6	Photon (ε_i) absorption by phonon	$\varepsilon_L - \varepsilon_g = \varepsilon_i$	Electron (ε_D) emission by phonon	$\varepsilon_L-\varepsilon_D= \varepsilon_m$	Phonon relaxation and photon emission	$\varepsilon_m - \varepsilon_g = \varepsilon_f$	Stokes

will have an energy unequal to that of the incident radiation ($\varepsilon_f \neq \varepsilon_i$) leading to what is known as inelastic scattering and the so called Raman effect. By monitoring the difference between ε_f and ε_i, through the shift between the incident and exiting photon frequencies, a deduction of the intermediate reaction can take place thus providing insight into either the temperature or stress dependent characteristics of the crystal lattice.

The nature of the crystal's dependence on temperature or stress may be illustrated through incorporation of classical theory to describe the interaction between the incident radiation and the lattice. The analysis begins by defining two properties determined by the electronic distribution within a crystal lattice in equilibrium, namely the dipole moment, P, and electric polarizability, α. The electric polarizability is a second order tensor response function that represents the volume and shape of the charge distribution in the lattice. When radiation with electric field, E, is incident on the lattice, the induced dipole moment is given by,

$$P = \varepsilon_o \alpha \mathrm{E} \tag{2}$$

At any finite temperature, the presence of phonons causes the charge distribution, and hence the electric polarizability tensor, to constantly change with time. These changes may be described through a Taylor series expansion of the polarizability about the equilibrium position of the lattice atoms:

$$\alpha = \alpha_o + \frac{d\alpha}{dq'} q' + ... \tag{3}$$

where α_o is the polarizability at the equilibrium lattice spacing and $q' = q_o cos(\omega_p t)$ is the time-dependent change in the lattice spacing due to phonon vibrations with amplitude q_o and frequency ω_p. Realizing that the incoming electric field, $E = E_o \cos(\omega_R t)$, can be

written as an oscillatory function of amplitude E_o and frequency ω_R, using Equation (3), Equation (2) may be written in expanded form:

$$P = \varepsilon_o \alpha_o E_o \cos(\omega_R t) + \frac{d\alpha}{dq'} \varepsilon_o q_o \cos(\omega_p t) E_o \cos(\omega_R t) \quad (4)$$

where ω_p is the frequency of the phonon vibration and ω_R is the vibrational frequency of the incident photon. Applying a trigonometric identity to Equation (4) leads to the following relation,

$$P = \varepsilon_o \alpha_o E_o \cos(\omega_R t) + \frac{d\alpha}{dq'} \frac{\varepsilon_o q_o E_o}{2} \cos\left((\omega_p - \omega_R)t\right) + \frac{d\alpha}{dq'} \frac{\varepsilon_o q_o E_o}{2} \cos\left((\omega_p + \omega_R)t\right) \quad (5)$$

The first term on the right hand side of Equation (5) accounts for Rayleigh scattering of photons. The second and third terms result in Stokes and anti-Stokes Raman scattering, respectively, where the photons are shifted away from their incident frequency ω_R by an amount equal to the optical phonon frequency ω_p [71].

A representative figure of the resulting Raman spectrum illustrating each of these differing scattering components is shown in Figure 7. From Equation (5), it is readily seen that the resulting Raman shift is directly dependent upon this phonon vibrating at ω_p. The temperature and stress dependence of the Raman signal is then an exercise in examining the thermal and mechanical response of this phonon. The following subsections describe the mechanisms by which this behavior may be captured by the Raman signal.

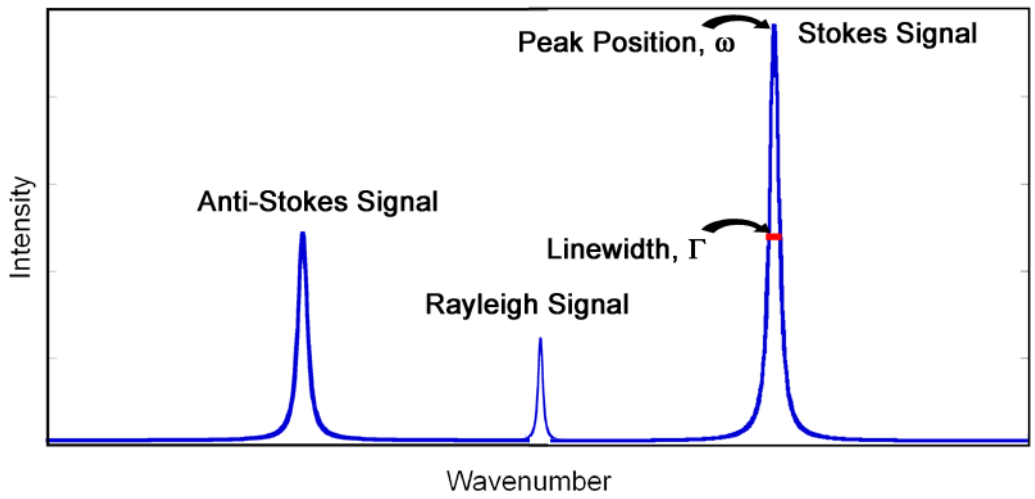

Figure 7. Representative Raman spectrum showing the Rayleigh, Stokes, and anti-Stokes responses. Although in reality the number of Rayleigh events far outweighs those of the Stokes and anti-Stokes variety, its response is mitigated through the use of filters in order to highlight the specific Raman contributions.

1.4.2 Temperature Dependence of the Raman Signal

1.4.2.1 Measurement of Temperature via the Stokes to anti-Stokes Intensity Ratio

At a given frequency shift ($|\omega_R-\omega_p|$), the intensity of a Raman signal will be proportional to the number of phonons at frequency ω_p present to take part in the scattering processes [70]. In an anti-Stokes process, the number of phonons that may be absorbed at a given temperature can be calculated from the Bose-Einstein distribution function described in Equation (6),

$$N_0 = \frac{1}{\exp\left(\hbar\omega_p / k_B T\right) - 1} \tag{6}$$

where $\hbar$ is the modified Planck's constant, and k_B the Boltzmann constant [72]. Similarly for a Stokes process, the total number of phonons will be this equilibrium distribution,

N_o, plus the emitted phonon for a cumulative total of $N_0 + 1$. Thus, the ratio in intensity of these two signals provides a measurement of temperature as delineated in Equation (7),

$$\frac{I_{AS}}{I_S} \cong \frac{N_o}{N_o + 1} \cong G \exp\left(-\hbar\omega_o \Big/ k_B T\right) \tag{7}$$

where G is a calibration factor, while I_{AS} and I_S are the anti-Stokes and Stokes intensities, respectively [73-75].

While the intensity ratio has been utilized in thermometry of III-V materials for over twenty years, its use remains extremely limited [76]. The method inherently requires longer experimental times as both the Stokes and anti-Stokes portions of the spectrum must be acquired. In addition, the precise quantification of intensities is difficult causing the resulting measurements to have larger uncertainties as compared to other Raman based techniques [77, 78]. Due to these factors, few studies have incorporated the method to interrogate GaN based devices. For example, only Aubry *et al.* [63] and Sarua *et al.* [79] have recently implemented the intensity ratio in the analysis of AlGaN/GaN devices .

1.4.2.2 Measurement of Temperature via the Stokes Peak Shift

Quantitative (extensive) measurements, such as those which compare intensities, are difficult to implement as the results will be dependent upon a host of experimental variables that determine signal strength. Consequently, it is desirable to instead analyze a qualitative (intensive) aspect of the acquired signal. In Raman spectroscopy, this is accomplished by examining the manner in which the vibratory aspects of the analyzed phonon change with temperature.

When considering the Raman scattering of photons using visible monochromatic laser light, the conservation of energy and momentum generally require that photons interact with optically coupled phonons near the Brillouin zone center (Γ-Point, see Figure 41), such that ω_p in Equation (5) corresponds to the zone-center optical phonon [73]. Thus, the temperature dependence of the phonons in the vicinity of zone center will help explain the temperature dependence of the Raman response. In general, the phonon vibrational modes and their dispersion can be modeled by considering a spring-oscillator system assuming that the force laws between the atoms or molecules in the lattice are known. The solution for this type of classical oscillator reveals that the resulting lattice vibrational frequencies vary with the interatomic forces [58]. As the lattice is heated or cooled, the equilibrium positions of the atoms are displaced, resulting in an overall volumetric expansion or contraction of the lattice and a change in interatomic forces due to the anharmonicity of the bonds [80]. These changes in the interatomic forces modify the phonon vibrational frequencies that, in turn, are reflected in the resulting variance of the Raman peak position.

In addition to this volumetric contribution, interactions between the phonons themselves augment the frequency shift as well [80]. This occurs as the mere presence of a phonon will alter the equilibrium spacing of the atoms in a lattice. With a change in equilibrium spacing, an associated altering of the interatomic forces will occur. Due to this change in the interatomic forces, the frequency of oscillation of both this and other phonons will be modified, thus affecting the frequency of the Stokes and anti-Stokes scattering. As the phonons responsible for this modification are governed by the Bose-Einstein distribution of thermal occupation, the resulting Raman shift varies due to this

contribution in a completely temperature dependent manner free of the effects of strain [81]. This contribution due to the presence of phonon interaction is typically termed the explicit contribution. The total frequency shift in the Raman signal is then some superposition of the explicit and volumetric contributions. Although either the Stokes or anti-Stokes contribution may be utilized in this analysis, typically the Stokes signal is incorporated as its signal is much stronger than its complement for the temperature range examined in most semiconductor devices.

In contrast to the intensity ratio, the peak position is easy to obtain and allows for a high degree of precision in the measurement of temperature. As a consequence, this spectral feature serves as the work horse for most Raman thermometry measurements. This fact is exemplified with respect to GaN based devices as the method has been utilized to: ascertain the temperature distribution between the gate and drain [82-86], produce a 2D dimensional thermal map of a transistor [54, 68], examine the through thickness thermal gradient [50, 87, 88], investigate the transient response of a HEMT [89, 90], and even to assess the robustness of other thermal measurement techniques [91].

1.4.2.3 Measurement of Temperature via the Linewidth of the Stokes Response

The origin of Stokes linewidth arises due to the Heisenberg uncertainty principle. According to this principle, a measured species, in this case the phonon, may only be measured within a certain energy band ($\Delta\varepsilon$) if its availability to be measured (i.e., lifetime) is finite. This is described mathematically according to the energy-time uncertainty relation:

$$\Gamma \approx \Delta\varepsilon = \frac{\hbar}{\tau} \tag{8}$$

where Γ is the width of the Raman line and τ is the scattering time for a phonon [92]. From Equation (8), one can see that the measured linewidth of a Raman peak will then vary proportionally with scattering time of the phonon mode. The scattering time of this phonon mode is dependent upon a variety of factors including microstructural defects, material boundaries, and, most importantly, other phonons. It is this dominant phonon-phonon scattering that gives rise to the temperature dependence of the linewidth as the number of phonons available for scattering is dependent upon the temperature deferent Bose-Einstein population distribution. As the temperature increases, so too does the number of phonons present, thereby increasing the likelihood of a scattering event. This increased likelihood reduces the phonon lifetime thus increasing the linewidth and allowing the linewidth to be used as a probe of temperature.

Due to its distinct link with scattering, GaN studies incorporating the linewidth have been exclusively centered on the decomposition of different phonon modes [93-96]. Studies with silicon, however, have showed promise for usage of this spectral component in the measurement of temperature [78, 81]. Despite this fact, no studies have yet utilized the linewidth in the thermal analysis of GaN devices.

1.4.3 Stress Dependence of the Raman Signal

To illustrate the effects of stress and deformation on the Raman signal, consider two objects connected by a spring of force constant K. The relative displacement of one mass, u, can be described using the dynamic relation where $\overline{m}$ is the reduced mass of both objects and $\ddot{u}$ is the acceleration of that mass:

$$\overline{m}\ddot{u} = Ku \tag{9}$$

If this spring were harmonic, the frequency, and as such the resulting peak position, of the normal modes could easily be found to be equivalent to $\omega = \sqrt{K/\bar{m}}$ irrespective of the mass' displacement. In reality, the spring connecting the two atoms is anharmonic and hence the force it imparts varies with strain. This variance can be described using Equation (10) where ε is the applied strain:

$$\frac{\partial K}{\partial \varepsilon}\varepsilon = K^1\varepsilon \,. \tag{10}$$

To account for the effect of this anharmonicity, Equation (9) must be modified as follows:

$$\bar{m}\ddot{u} = \left(K + K^1\varepsilon\right)u \,. \tag{11}$$

The solution of Equation (11) allows for the changes of the normal mode vibrations to be solved as a function of strain and, in turn, the dependence of the peak position as well. In practice, material dependent phonon deformation potentials (PDP) are utilized allowing for the modified spring constant to be described as $K^1 = \bar{m} \times f(p,q,r)$ with p, q, and r as the PDP. Specification of this spring constant then allows for Equation (11) to be solved through the following secular equation as was performed originally by Ganesan *et al.* [97]:

$$\begin{vmatrix} p\varepsilon_{11} + q\left(\varepsilon_{22}+\varepsilon_{33}\right) - \lambda & 2r\varepsilon_{12} & 2r\varepsilon_{13} \\ 2r\varepsilon_{12} & p\varepsilon_{22} + q\left(\varepsilon_{11}+\varepsilon_{33}\right) - \lambda & 2r\varepsilon_{23} \\ 2r\varepsilon_{13} & 2r\varepsilon_{23} & p\varepsilon_{33} + q\left(\varepsilon_{11}+\varepsilon_{22}\right) - \lambda \end{vmatrix} = 0 \,. \tag{12}$$

In the above relation, ε_{ij} are the strain tensor components and λ_j are the eigenvalues for phonon polarization modes j. The difference in frequencies of the Raman spectra with

(ω_j) and without strain ($\omega_{o,j}$) can be correlated using these eigenvalues according to the relation:

$$\lambda_j = \omega_j^2 - \omega_{o,j}^2 . \tag{13}$$

In the special case of biaxial strain common in many MEMS and microelectronic thin film devices, $\varepsilon_{12} = \varepsilon_{23}=\varepsilon_{13}=0$, and the secular equation reduces to:

$$\begin{vmatrix} p\varepsilon_{11}+q\left(\varepsilon_{22}+\varepsilon_{33}\right)-\lambda & 0 & 0 \\ 0 & p\varepsilon_{22}+q\left(\varepsilon_{11}+\varepsilon_{33}\right)-\lambda & 0 \\ 0 & 0 & p\varepsilon_{33}+q\left(\varepsilon_{11}+\varepsilon_{22}\right)-\lambda \end{vmatrix} = 0 . \tag{14}$$

The solution of this equation allows for the following simple relation between the shift in the Stokes peak to the level of stress present in the device:

$$\Delta\omega = D\sigma . \tag{15}$$

where D is a calibration constant obtained separately and σ is the stress.

The derivation of Equation (15) demonstrates that the stress sensitivity of the Raman signal arises from a modification in the strength of the interatomic bonds (i.e., springs) in response to an elastic deformation (i.e., strain). With a change in the strength of these bonds, the resulting frequency of the vibrational modes governed by these "springs" is altered as well. This modification is "felt" by that portion of the Raman spectrum probing the energy of these modes, namely the peak position. Notice that the physical causation for the spectral dependence stems from a relative displacement of one atom relative to another irrespective to the source of this displacement. Therefore, as both temperature and elastic stress induce such a displacement, the peak position dependence to each of these effects is then identical in its causation and inherently convoluted in their dual presence.

Due to this dual dependence of the peak position, Raman measurements have been limited to quantifications of only those stress components that may be measured apart from thermal loads. Despite this significant limitation, Raman is frequently incorporated to examine the dependence of the residual stress to such factors as film thickness [66, 98], substrate [99, 100], and surface depth [101]. In addition, the peak position has also been implemented to quantify the stress that evolves in response to the inverse piezoelectric effect [102]. However, as the operational thermoelastic stresses have not been quantified, measurement of the total load in AlGaN/GaN HEMTs has not been possible using Raman or any other technique.

1.5 Limitations in the Analysis of GaN Devices Using Raman Spectroscopy

Upon application of an electric bias on an AlGaN/GaN HEMT, inverse piezoelectric effects immediately induce a strain in direct proportion to the level of field present at a distinct location. Simultaneously, the potential field impels acceleration of the electrons through the device at which point the transistor begins to operate. The transformation of the potential energy of the bias into kinetic energy of the electrons causes a level of heating in the device linked to the resistance of this carrier movement and the number of carriers present at a point in space. The heating, in turn, leads to thermal expansion that serves to enhance the piezoelectric contribution to the total strain. In total, the confluence of these mechanisms elicits a level of both heightened temperature and stress at all locations near the active region of the HEMT. It is, therefore, imperative that the measurement techniques used to measure either of these parameters be then able to distinguish between them. Otherwise, any resulting estimations will be in error as the signals will be convoluted between both thermal and elastic sources.

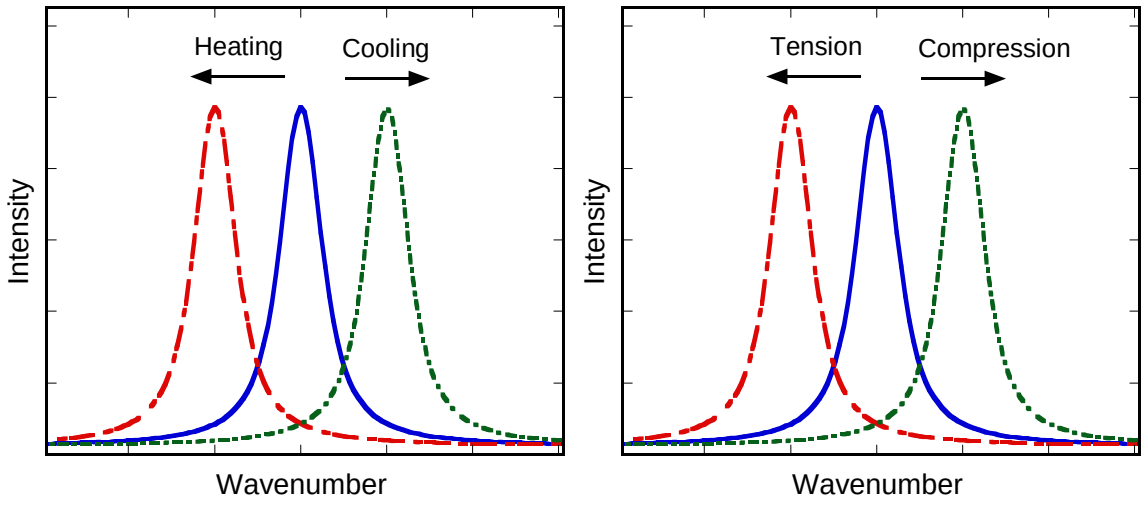

Figure 8. Response of the Raman signal's peak position to the effects of both temperature (left) and stress (right). The peak position shows a dependence to each effect making the measurement of either difficult in their simultaneous presence.

Due to ease of acquisition and lower inherent uncertainties, the peak position is the most frequently implemented method utilized to measure either temperature or stress in GaN devices [103]. Utilization of this spectral component is problematic in the analysis of AlGaN/GaN HEMTs, however, due to the dual presence of both temperature and stress during operation. The complication stems from the nature of the peak position signal, which is derived mainly from the interatomic potential between the atoms. The interatomic potential, and hence the peak position, is modified by any strain regardless of its origin as is shown schematically in Figure 8. Consequently, under combined thermomechanical loading, this change in peak location becomes convoluted due to the simultaneous effects of both temperature and stress relegating the accurate measurement of either parameter impossible. In fact, previous studies have specified errors in the measurement of temperature of up to 40°C due to the presence of stress in GaN transistors [102, 104]. Furthermore, there has been no investigation, Raman or otherwise,

which has experimentally quantified the level of operational stress present in an AlGaN/GaN HEMT as thermal effects inherently mask the elastic response.

1.6 Linewidth of the Stokes Response to Analyze AlGaN/GaN HEMTs

Unlike many other thermometry methods, Raman directly probes the lattice vibrations allowing for information concerning both the stress state and the optical phonon transport within the device to be gleaned in addition to the temperature. Most investigations, however, forfeit much of this additional information and sacrifice substantial accuracy in the very measurement of temperature through sole reliance on just a portion of the Raman response, namely, the Stokes peak position. In response to these challenges, this study focuses on developing a Raman technique capable of both increasing the accuracy of device temperature measurement and sustaining the fidelity of the added lattice information inherently present in the signal through incorporation of an additional spectral component.

Often neglected, the linewidth (FWHM) of the Stokes response offers intriguing capability into meeting these objectives. This aspect of the signal is directly related to the scattering time of the examined phonon mode, and until the most recent past, has been employed exclusively to analyze the lifetime of this lattice vibration [93, 96, 105]. These scattering times are dominated by the population of the phonons themselves; a population governed solely by temperature through the Bose-Einstein distribution. Due to this temperature dependent population, it is possible to utilize the linewidth of the Raman spectrum to measure temperature [106]. In addition, the linewidth's dependence upon the Bose-Einstein phonon distribution also suggests a possible independence of this part of the spectrum to thermoelastic stresses as was reported by Abel *et al.* [78]. Consequently,

increased accuracy in Raman temperature measurements in the presence of stress may be realized through use of this spectral component.

The incorporation of this newly proposed linewidth thermometry method allows for the operational stress in the device to be acquired as well. Specifically, measurement of the temperature using the Raman linewidth allows for the Stokes peak position response to be deconvoluted from its dual dependence upon temperature and stress. The successful use of this deconvolution will enable Raman spectroscopy to be the first technique capable of simultaneously probing the full thermomechanical response in operating electronic devices. Furthermore, the linewidth also allows for insight into the evolution of these measured parameters as it probes the scattering of the phonon, and hence, its transport. Therefore, through implementation of the linewidth new avenues are made available for a thorough *quantitative* description of the thermomechanical environment while offering a fresh glimpse into the *qualitative* nature of how this environment came to be.

1.7 Method and Outline of Study

Specifically, the current study develops the use of the linewidth to overcome the limitations of peak position based Raman measurements in order to more thoroughly investigate the coupled thermo-electro-mechanical loop determining the performance and reliability of AlGaN/GaN HEMTs. The methodology divides this task among two thrusts that leverage linewidth's capability to probe the transistor's response in both a quantitative and qualitative fashion. Quantitatively, device assessment is first examined through investigation of temperature measurements performed in the presence of complex stresses during operation of GaN microelectronics (Chapter 2). Using the

information obtained with respect to the stress dependence of the spectral components, a method to measure the operational thermoelastic stress in a single measurement is then described in Chapter 3. With this new capability, the residual, thermoelastic, and piezoelectric induced stresses are compared to obtain the total load in an AlGaN/GaN HEMTs for the first time.

The secondary thrust of this investigation focuses on the role of lattice transport in the thermal response of GaN devices to aid in the qualitative explanation of the temperature values initially measured. First, the additional lattice information implicitly contained, but frequently ignored, in the Raman spectrum is examined in order to help elucidate the role of phonon/carrier interaction in the dissipation of thermal energy. Utilizing the linewidth to measure the lifetime of a series of phonon modes, the effect of free carrier concentration on the transport of phonons is investigated in Chapter 4 to identify energy bottlenecks that occur during device operation. This study provides not only unique insight into the phonon modes that limit heat dissipation, but also provides critical phonon lifetime data needed for device simulation. Subsequently, Chapter 5 further examines the role of lattice transport through a simulation of heat transport at the interfaces between the active, GaN, region of the device and the underlying substrate through which the majority of the thermal energy flows. The role of disorder at these interfaces and the relative merits of the frequently employed substrates utilized in these devices are examined. The final portion of this study (Chapter 6) serves to summarize the major findings and discusses the conclusions of the study as a whole.

CHAPTER 2

MICRO-RAMAN THERMOMETRY IN THE PRESENCE OF COMPLEX STRESSES IN GAN DEVICES

2.1 Overview and Approach

AlGaN/GaN HEMT device reliability is inversely related to the operational temperature as degradation has been observed to most often follow an Arrhenius relationship [34]. To accurately assess the nature of this thermally induced degradation and predict the resulting mean time to failure, it is then necessary to first acquire an accurate measurement of the temperature itself. While a number of techniques have been utilized in the thermometry of GaN devices, Raman spectroscopy remains one of the most widely incorporated. The 1 μm spatial resolution and relative ease of implementation have offered insight into physical phenomena previously undetectable by methods such as IR thermography [53, 54, 63, 68, 82, 84, 85, 87]. In Raman thermometry, temperature is deduced through analysis of the inelastic energy transfer between light (photons) and lattice vibrations (phonons). As the incident light is invariant with device temperature, all deductions are based upon changes in the phonon behavior of the crystal. Thus any aspect of the phonon that changes with temperature, i.e. its population, lifetime, or energy, can then be used to probe the thermal state of the device.

Temperature measurements using Raman spectroscopy are typically carried out by analyzing changes in the energy of zone-centered optical phonons through analysis of the Stokes peak position. In such an approach, a shift in frequency of the peak is monitored

and subsequently converted to temperature using an appropriate calibration standard. Often, this calibration is acquired by tracking the change of a prominent Raman peak across the temperature range of interest. Practically, this occurs by uniformly heating a sample and following the degree to which the peak shifts due to a known temperature change. Upon calibrating a GaN epilayer structure, however, there is an inherent evolution of thermoelastic stress that arises due to mismatches in the coefficients of thermal expansion between the layers. The extent to which this stress develops, in turn, affects the resulting calibration. In fact, previous research has demonstrated that differences in the Raman calibration of GaN epilayer structures may be attributed to variances in the stress states between the samples [104]. As a consequence, a calibration is strictly valid only if the stress state at which the measurement is taken is identical to that at which the calibration was performed.

Similarly, a peak position based temperature measurement remains strictly valid only if the stress state during the acquisition is identical to that of the calibration. In reality,

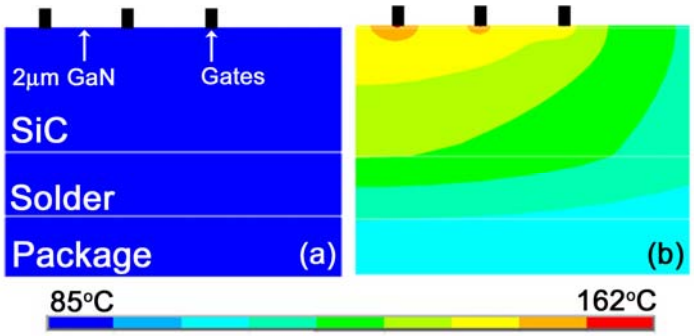

Figure 9. Modeled temperature contours in HEMT device during (a) calibration and (b) operation. Due to the difference in temperature distributions, the stress state during operation will be different than that of calibration. The differing stress states will contribute to errors in the measurement of temperature when utilizing the Stokes peak position.

however, calibration occurs through uniform heating of the sample while a device in operation is subject to localized heating that induces a vastly different stress state (see Figure 9). Hence, device temperature measurements using the Stokes peak shift are then subject to errors induced by the presence of stress as may be visualized in Figure 10.

During a typical measurement, for example, the device is initially investigated at a known reference temperature T_o (Point A). Upon operation of the device, the temperature increases to some temperature T that, independent to the presence of stress, would induce a shift in the Raman response (Point B). However, the presence of compressive stress that arises during sample heating suppresses this peak shift (Point C) resulting in an underestimation in the measurement of temperature. This situation is particularly problematic for electronic devices that often have regions of localized heating (e.g., transistor channels) in which compressive stress states result due to the

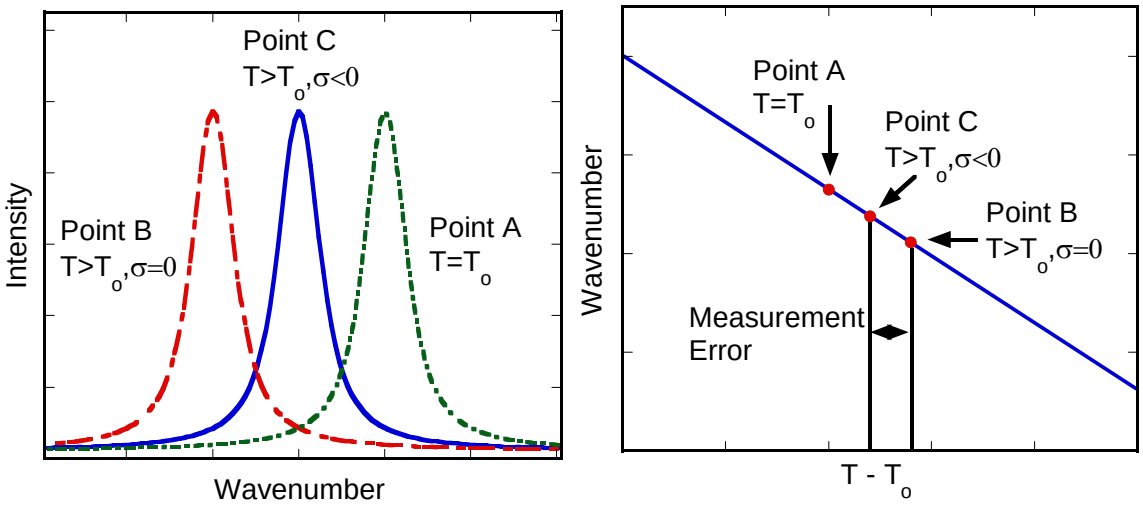

Figure 10. Measurements of temperature using the peak position begin with a reference scan at a known temperature (Point A). With an increase in temperature during calibration, the peak shifts to a lower wavenumber (Point B). During operation of a device, compressive stress reduces the magnitude of this shift (Point C) causing errors in the resulting measurement of temperature.

thermal expansion constraints provided by the cooler surrounding material. Thus, peak position based Raman thermometry of electronics is subject to under estimations in the measurement of temperature due to these compressive stresses.

The extent of this under estimation is directly proportional to the degree to which the stress state at calibration differs from that of measurement. Therefore, if the deviation between the stress states is minimal, then the errors are small as well. Regardless, it is necessary to consider the stress when making Raman temperature measurements as its presence may yield large, non-negligible, errors [102, 104]. Despite this fact, while some investigations have been performed with respect to both MEMS and GaN devices, the impact of evolving stress states on Raman thermometry has received limited attention in the literature [78, 82, 104, 106, 107].

Stress independent Raman measurements may be accomplished by examining the solely temperature dependent phonon population through analysis of the ratio between the Stokes and anti-Stokes intensities [108, 109]. Although theoretically simplistic, the extensive nature of this measurement makes both calibration and experimentation quite difficult in practice [110]. In addition, the integration time is at least double that of a standard Stokes analysis making the approach time intensive as well as tedious. In light of these considerations, the ideal Raman spectral component for thermal measurements would provide both the stress insensitivity of the Stokes/anti-Stokes ratio with the speed of the Stokes peak position measurement.

To this end, recent investigations have focused on performing temperature measurements utilizing the lifetime of the phonon through analysis of the linewidth of the Stokes response. This aspect of the spectrum is stress insensitive in silicon based devices

thus allowing for thermal evaluation even in the presence of an evolving thermoelastic stress [106]. However, in GaN based devices, it is unclear whether this same insensitivity will remain as stress no longer stems solely from thermally induced effects but also due to piezoelectric contributions that may affect both the energy and the lifetime of the phonon. Such ambiguity demands that the full nature of the Raman response be examined with respect to these dual stress effects in order to develop an accurate temperature measurement technique independent of their presence.

In response to these aforementioned issues, this study presents an examination of the Raman response of the E_2^{High} phonon mode in GaN to the effects of both mechanical and inverse piezoelectric induced stress. For each of the induced stresses, the dependence of the Stokes peak position, linewidth, and Stokes/anti-Stokes intensity ratio is examined. With knowledge of the spectral dependencies, temperature measurements that account for these stress effects were performed on two differing GaN device architectures through the use of both the Stokes linewidth and the ratio of Stokes to anti-Stokes intensities. Comparisons between measurements and a 3-D finite element model were then made in order to validate the experimental results.

2.2 Device Technology

GaN devices utilized in this study are provided by RFMD® Inc. The devices are based on an undoped AlGaN/GaN heterostructure epitaxially grown on an optimized GaN buffer layer that itself was grown on a semi-insulating silicon carbide (SiC) substrate. A transmission line measurement device (TLM) was then created on this epilayer stack by patterning a source and drain using Ti/Al based ohmic contacts. In the case of the TLM devices, these contacts are separated by a 20 μm channel that serves as

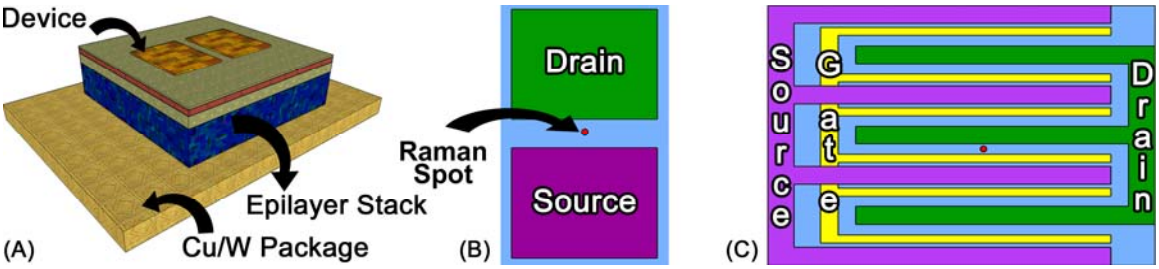

Figure 11. Schematic showing layout of (a) the entirety of the package (b) TLM and (c) HEMT including location of the Raman spot.

the active region of the device. A high electron mobility transistor (HEMT) was also fabricated on the same epilayer stack using similar source and drain contacts along with an additional 0.5 μm long Nickel Schottky barrier gate contact. Further details on the processing and composition of both the TLM and HEMT, each of which are shown schematically in Figure 11, may be found in [111, 112]. Finally, in order to facilitate testing, the devices are wafer bonded to an alloyed copper/tungsten (Cu/W) package.

2.3 Raman Instrumentation and Testing Procedure

All Raman experiments were performed through use of a Renishaw InVia Raman microscope with 180º backscattering geometry and 488 nm Ar^+ laser (see Figure 12). To facilitate the experiment, monochromatic laser light, insured through use of a rejection filter, is spatially collimated whereupon it is focused using standard microscopic optics resulting in a beam spot of as little as 1 μm [109]. Upon the radiation's impingement with the surface, on the order of only 1 in 1000 incident photons are scattered by the analyte material. Of this scattered radiation, less than 1% (i.e., 1 out of every 10^6 photons initially incident) actually stems from the Raman signal [113]. This necessitates that much of the radiation collected by the microscope objective be routed through a filter in

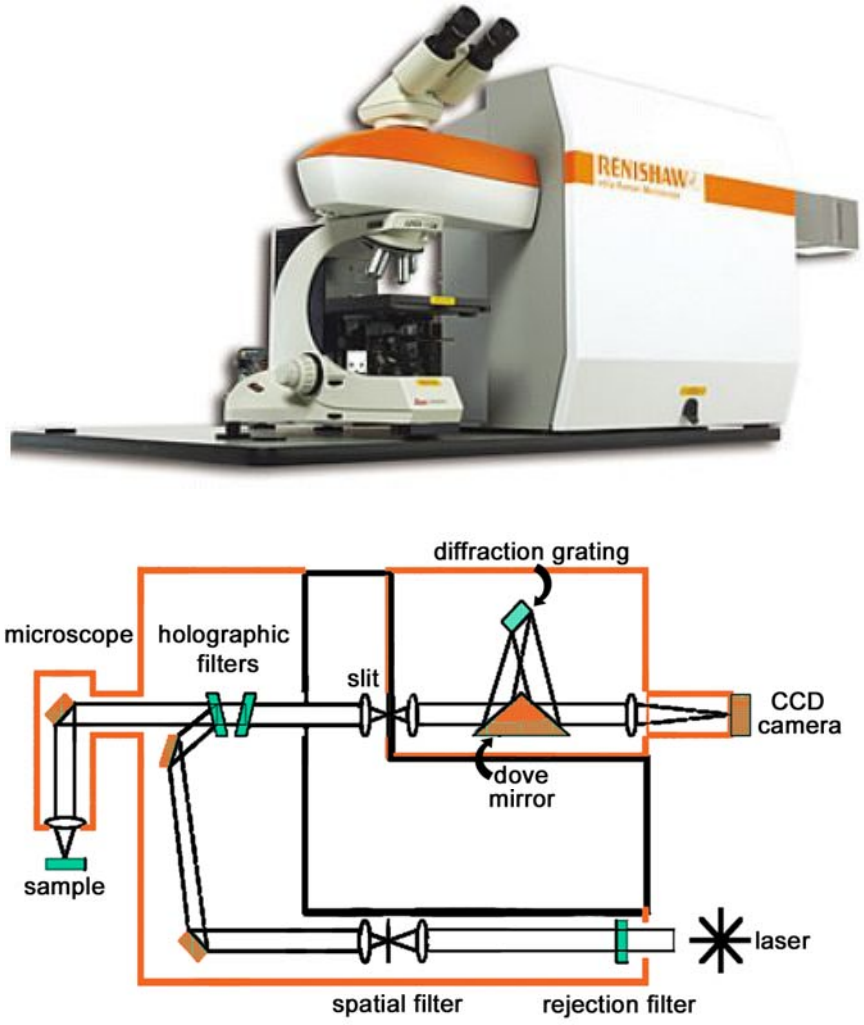

Figure 12. Renishaw InVia system (top) that performs the micro-Raman backscattering experiment, in which light is both scattered and collected via a microscope and subsequently measured utilizing a dispersive grating and CCD device. (Upper image courtesy of Renishaw plc.)

order to negate the overwhelming Rayleigh and reflected signal. After filtering, the resulting Raman radiation passes through a slit that aligns the beam with the dove mirror. The dove mirror, in turn, directs the signal onto a grating that disperses the radiation into its constituent components via Bragg diffraction, thus allowing measurement of the light across the spectrum via a multi-channel CCD collector.

For this study, a spectrometer focal length of 250 mm was employed in combination with a diffraction grating of 3000 lines/mm, allowing for a spectral dispersion of 0.46 cm^{-1}/pixel to be obtained at a slit width of 40 μm. A slit width of 40 μm provides an attractive balance between detection capabilities and signal levels at the expense of some spectral resolution. Even with this expense, however, the resolution is sufficient for detecting Stokes peak shifts to within ±0.037 cm^{-1} from Voigt fits of the isolated E_2^{High} GaN Raman line. A 50X objective with a numerical aperture (NA) of 0.5 and a "long" working distance of 8.6 mm was used to focus the probe laser beam and collect the Raman signature of the samples. Finally, as GaN is semi-transparent for the visible light used as a probe, laser heating of the sample is of minimal consequence.

2.3.1 Calibration of the Raman Spectrum with Temperature

The acquisition of temperature using Raman spectroscopy necessitates an accurate calibration of the Raman response across the entirety of the temperature range of interest. To this end, a TS-1200 Linkam thermal stage (see Figure 13) is utilized to uniformly heat the calibrated species allowing for its response to be monitored at a series of known temperatures. In this manner, temperature is directly correlated to a change in the Raman signal thereby enabling these changes to be utilized as a thermometry probe. Practically, a complication arises in using the stage as the working distance of the objective is less than the distance from the heated surface to this optical component (see Figure 13). It is, therefore, necessary to utilize a spacer to raise the sample to a level within the objective's working distance. This spacer, however, has a non-negligible thermal resistance that induces a difference between the temperature of the crucible and that of the sample being examined. To circumvent this difficulty, the well characterized Raman response of stress

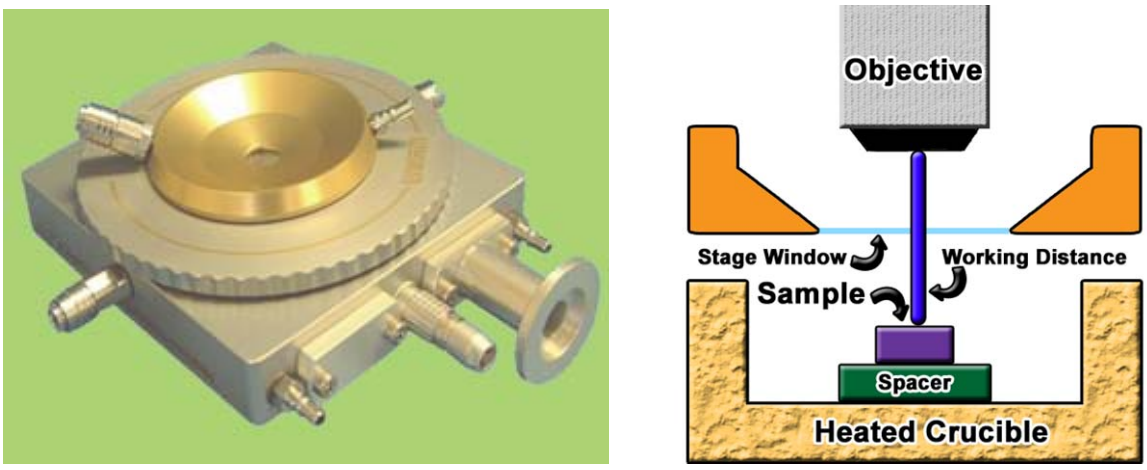

Figure 13. The Linkam TS-1200 heated stage is pictured (left) along with a schematic of its cross section (right). The stage is implemented to acquire the calibration of a material's Raman's response with temperature. The stage uniformly heats the sample allowing for the response to be acquired at a known condition. (Image adapted from Linkam Scientific Instruments Ltd.)

free silicon was utilized as a surrogate sensor in order to specify the actual temperature of the sample even as it rested on the spacer [114]. In this manner, the Raman response of all spectral components may be calibrated irrespective to the nature of the crucible's thermal environment.

Utilizing this procedure, two sample types were calibrated for this study. In the first, the response of a monolithic crystal is analyzed such that the material response may be analyzed apart from the evolution of any stress. This is particularly useful for the acquisition of the stress free response of the peak position that is utilized to quantify the thermoelastic stress in Chapter 3. With respect to the Stokes/anti-Stokes intensity ratio, however, differences in the optical characteristics of the monolithic sample and the device under test may be large. These differences, in turn, may induce large uncertainties in the resulting measurement of temperature. In response, all temperature measurements in this study were obtained through the calibration of an actual TLM device.

Incorporation of this procedure minimizes both these optical differences as well as any microstructural variations between the calibrated species and the measured device. While the usage of a multilayered device will undoubtedly induce a degree of stress dependence into the peak position calibration, the resulting temperature measurements will still be modified by the evolving stresses due the vastly different elastic states between calibration and device operation (see Figure 9).

Specifically, this type of calibration was obtained through analysis of the GaN E_2^{High} mode at the midpoint of a TLM device from 23°C to 500°C. For each measurement, at least 70 separate spectra were obtained with integration times adjusted such that peak heights remained constant at ~10,000 counts. The acquired spectra were then fit using Voigt profiles in order to calculate the temperature dependency of the Stokes peak, linewidth and ratio of Stokes to anti-Stokes intensities. After all measurements were completed, the dependencies were found to follow the expected linear, parabolic, and

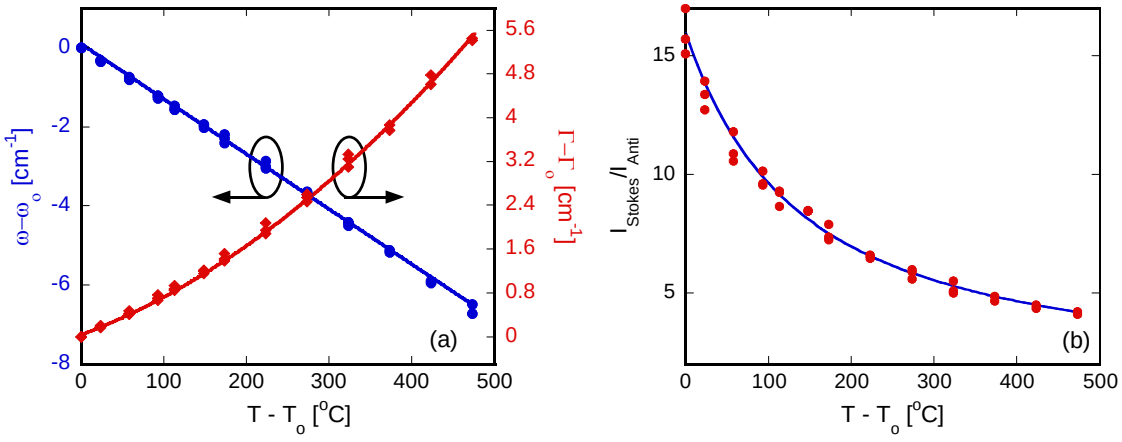

Figure 14. Calibration of (a) Stokes peak position, (b) Stokes linewidth and (c) the ratio of Stokes to anti-Stokes intensity as a function of temperature at the midpoint of a packaged TLM device. Using these curves, any change in a spectral component may be transformed to temperature if stress induced effects are negligible.

exponential trends for the peak position, linewidth, and intensity ratio, respectively, as is shown in Figure 14.

Through fitting of these trends, any change in the spectrum can be correlated to an equivalent change in temperature. With respect to the peak position and linewidth, the temperature measurement is intensive in nature as a relative change from a known reference condition is transformed to an equivalent temperature using the linear and parabolic relationships in Equations (16) and (17) shown below,

$$\omega = A\left(T - T_o\right) + \omega_o \tag{16}$$

$$\Gamma = B\left(T - T_o\right)^2 + C\left(T - T_o\right) + \Gamma_o . \tag{17}$$

In the above equations, ω and Γ are the measured peak position and linewidth at temperature T while ω_o and Γ_o are the reference peak position and linewidth measured at the reference temperature of T_o. A, B, and C are calibration constants, which are given alongside their 95% confidence intervals in Table 2 . In contrast to the spectral

Table 2. Calibration constants and their 95% confidence intervals utilized to transform a spectral change into temperature.

Peak Position		Linewidth		Intensity Ratio	
Calibration Constant		Calibration Constant		Calibration Constant	
A [$cm^{-1}/°C$]	-0.01411 ± 3e-5	**B** [$cm^{-1}/°C^2$]	1.207e-5 ± 2.4e-7	**G**	2.103 ±.029
		C [$cm^{-1}/°C$]	5.95e-3 ± 1.23e-4	**H** [K]	609.1 ±11.7

components described in Equations (16) and (17), the Stokes to anti-Stokes intensity ratio is extensive in nature and hence does not depend on a relative change (i.e., $\omega - \omega_o$). Rather an absolute ratio is related to the temperature through calibration constants *G* and *H* described in Equation (18) below:

$$\frac{I_{Stokes}}{I_{Anti}} = G \cdot e^{\left(-\frac{H}{T}\right)}. \tag{18}$$

2.3.2 Effects of Mechanically Induced Stress on the Raman Spectrum

To quantify the effect of stress on the Raman spectrum, a 4 point bending procedure was performed on the epilayer stack consisting of the SiC, GaN, and AlGaN layers using the testing stage shown in Figure 15. Under increasing levels of tensile stress of up to 360 MPa applied along the basal plane (plane $\perp$ to c-axis) of the GaN crystal, spectra were collected and analyzed with respect to the change in peak position, linewidth, and intensity ratio. While the induced stress was uniaxial rather than biaxial in nature, the Raman response between the different stress states are linked due to the commonality in

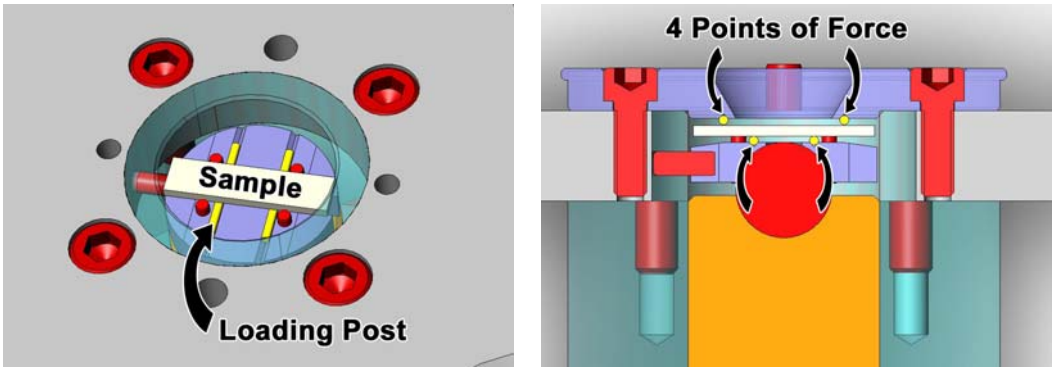

Figure 15. Schematic representation of 4-point bending stage utilized to examine epilayer stack in either mechanically induced tension or compression. (Drawings courtesy of David Schmale at Sandia National Laboratories)

the phonon deformation potential within the basal plane [115].

2.3.3 Effect of Inverse Piezoelectric Loads on the Raman Spectrum

Thermoelastically induced stresses are not the sole contributor to the overall stress state during the operation of GaN transistors as the inverse piezoelectric effect is prevalent as well. Thus to understand the entirety of the stress's effect on the Raman response, a HEMT device was powered under pinch off conditions in order to induce this type of load while simultaneously preventing device heating. The Raman response was then characterized with varying source-drain biases ranging from 10-48 V, which gave rise to varying levels of stress stemming from the inverse piezoelectric effect. With this approach, the Raman response is monitored under loads induced independent of Joule heating as the current is held below 0.02 mA in a manner similar to that of Sarua *et al.* [102].

2.3.4 Device Temperature Measurements

Using the acquired dependencies of the Raman response to temperature and stress, temperature measurements were carried out on both the TLM and 6-finger HEMT during device operation. For all measurements, samples were mounted to a controlled heated stage with a thermal grease compound in order to reduce any contact resistance such that the backside package temperature of the device was maintained at 85 +/- 0.5°C as verified using, once again, Raman thermometry of a stress free sample of silicon. The 85°C package temperature is utilized as it induces higher operating temperatures and stress during device operation that allow for a more rigorous examination of each spectral component's response. For the TLM, Raman spectra were obtained at the midpoint of

the device under power dissipations of up to 6 +/- 0.01 W as monitored by a Keithley 2430 SourceMeter®. At each power level, the Stokes peak shift, linewidth, and intensity ratio were used to measure temperature. A similar procedure was used in the analysis of the HEMT to examine temperatures at total dissipated powers levels up to 6.2 +/- 0.01 W (2.8 W/mm). In this case, the Raman response was acquired along the 3rd finger at the midpoint of the channel between gate and drain halfway along the gate width as seen in Figure 11(C).

2.4 Finite Element Modeling of Devices

To verify the temperature measurements acquired during the Raman experiments (as well as the stress measurements acquired as part of Chapter 3), finite element models of both the TLM and HEMT devices were built utilizing the ANSYS software package [116]. In order to simplify the systems under investigation, symmetry allowed for only one quarter of the geometry to be modeled as is shown in Figure 16 for the HEMT device. This geometrical reduction limited the number of elements, thus speeding convergence. To capture the essential non-linear physics of the devices, temperature dependent thermal properties were incorporated into the GaN, SiC, and Cu/W layers as shown in Table 3. For the GaN, thermal conductivity values were acquired as a function of temperature through 3ω testing of MOCVD prepared GaN grown on sapphire, which is of similar quality to that of the epilayer stack [117]. Results from the test compare favorably with other reported values of thermal conductivity for GaN thin films with similar defect densities and doping profiles [118]. Further details on the 3ω technique are outlined in [119].

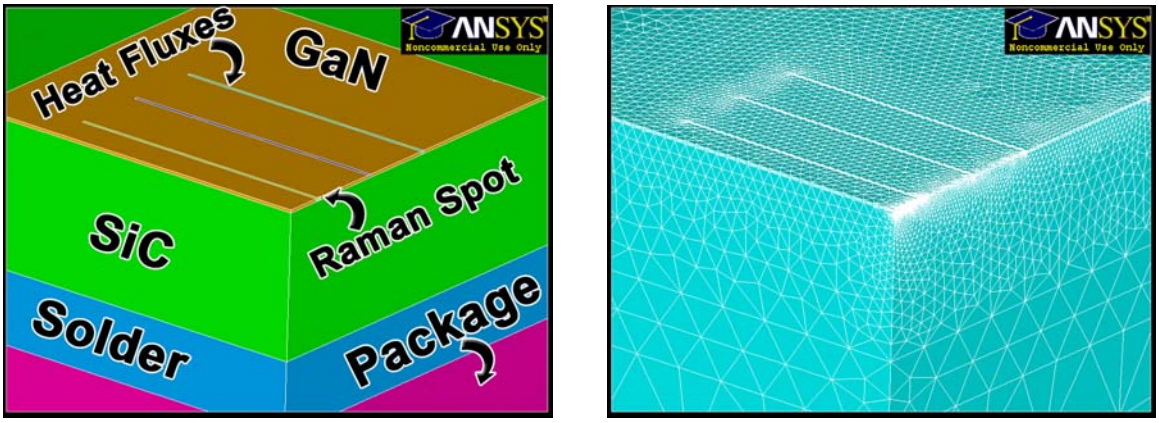

Figure 16. Results from an electro-thermal coupled ANSYS simulation of the TLM and HEMT are compared to the Raman derived measurements of the temperature (Chapter 2) and biaxial thermoelastic stress (Chapter 3). Quarter symmetry of the HEMTs material stack (Note: TLM not shown) (left) is examined with a refined grid (right) allowing for efficient computation of the device's thermal and mechanical response.

Additional layers in the packaged devices included a solder layer between the SiC and Cu/W, as well as a simulated thermal grease layer. While the solder layer was included in the model specifically, the effects of the thermal grease layer were included through stipulation of a contact resistance between the bottom of the Cu/W package and the temperature of the heated stage (85°C). This one dimensional approximation to the

Table 3. Thermal properties incorporated in the 3-D finite element model.

Material	Property	Formula/Value	Reference
GaN	k(T) (W/mK)	$0.0013T^2$-1.3864T+547.41	Measured in this study
SiC	k(T) (W/mK)	61100/(T-115)	[120]
Solder	k (W/mK)	60	Supplied by vendor
Cu/W Package	k(T) (W/mK)	$-0.0004T^2$-0.7492T+18.20	[121]

grease layer is acceptable assuming the spreading resistance is small, which is likely owing to the extreme thinness of the layer.

It is important to note that the thin AlGaN layer used to generate the two-dimensional electron gas (2DEG) at the heterointerface of the bulk GaN layer is not modeled. Typical AlGaN layers are extremely thin, typically two orders of magnitude smaller than the GaN film, thereby contributing little to the thermal signature. The nature of such a thin film also allows for the heat generation to be added into the problem as a surface heat flux boundary condition instead of an embedded volumetric heat generation. This implementation is advantageous as it significantly reduces the number of elements needed to accurately model the temperature response of the entire packaged device. All solutions generated were then checked against multiple meshes to ensure proper convergence (see Figure 16 for final refined mesh). Convergence was defined to be the point when the maximum temperature calculated between meshes deviated by less than 1%.

Solutions generated with the finite element model allow for the temperature field to be known throughout the entirety of the three-dimensional structure. This is not true, however, for measurements made with the micro-Raman technique. Gallium nitride is semi-transparent to the 488 nm laser used in the experiments, and therefore, the Raman system is essentially probing a volume of GaN instead of a distinct focal point. The resulting measurements are then a volume average through the GaN layer rather than a temperature at a distinct location. This averaging will under-predict the maximum device temperature by an amount proportional to the input power. Consequently, in order to compare the simulated results to the Raman data, the calculated temperature field was

averaged through the entirety of the GaN layer using a simulated cylindrical volume 1 μm in diameter analogous to the region that is experimentally probed.

2.5 Effect of Stress on the Raman Spectrum

2.5.1 Effects of Mechanically Induced Stress on the Raman Spectrum

The effect of mechanical stresses on the Raman spectrum in GaN is shown in Figure 17. As expected, the peak position shows a linear shift with stress. This dependency arises due to changes in the interatomic potentials occurring between each of the atoms along the direction of the load. The interatomic potential, in turn, is the greatest determinant of the phonon frequency and hence with its change comes an associated change in the peak position response [80]. As these potential changes cause the peak position to shift to higher wavenumbers with compressive loads while decreasing with higher temperature, measurements derived from this aspect of the signal oftentimes under predict the temperature during analysis of an operational device [78, 106].

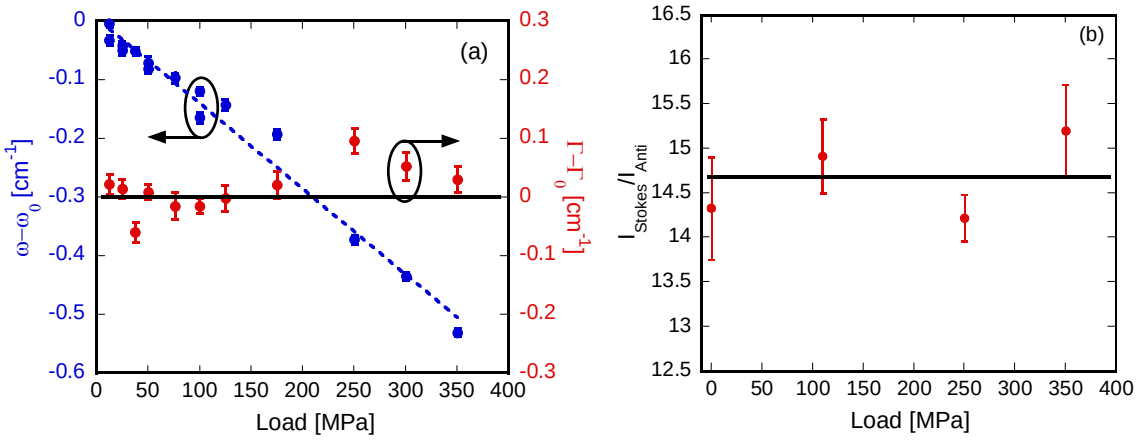

Figure 17. Effect of uniaxial stress on (a) Stokes peak position, Stokes linewidth, and (b) Stokes/anti-Stokes ratio applied upon the epilayer stack. Only the peak position shows a dependence upon this mechanically induced stress along the non-polar planar direction.

The same dependency on mechanical stress is not seen, however, in either the response of the linewidth or the ratio of Stokes to anti-Stokes intensities as is seen in Figure 17. This independence arises due to the very nature of the signals from these components. For example, the Stokes/anti-Stokes intensity ratio is chiefly dependent upon the population of the phonon being examined. Thus, as the number of phonons is determined by the temperature dependent Bose-Einstein distribution, the resultant signal is independent of the applied stress as the phonon's population is independent of the stress' presence as well.

Similarly, the linewidth shows independence to this type of stress as its response is largely population dependent as well. Its signal arises as a consequence of the Heisenberg uncertainty relation, which stipulates that a measured species, in this case the phonon, may only be measured within a certain energy band if its availability to be measured (i.e. lifetime) is finite. This lifetime, in turn, is dependent upon a variety of scattering sources including, most importantly, other phonons. As phonon-phonon scattering most often dominates, it is then both the presence of, and interaction with, other phonons that will determine the linewidth of the Raman signal. The presence of these other phonons is determined by, once again, the temperature dependent Bose-Einstein population distribution while the interaction between phonons is decided by the dispersion of the crystal lattice stemming from the interatomic potential field [96]. While the interatomic potential field certainly changes with stress, the empirical results of the bending test indicate that only a minimal change in the phonon-phonon scattering results when the stress is applied along the non-polar basal plane of the crystal. As a result, both the linewidth and the Stokes/anti-Stokes intensity ratio may then be used to

measure temperature even in the presence of a biaxial stress oriented along this basal plane as often evolves during operation of a device.

2.5.2 Effect of Inverse Piezoelectric Load on the Raman Spectrum

Unlike the one dimensional electric field present during operation of a TLM structure, a two dimensional field forms upon activation of the HEMT device. The 2D field will be oriented in such a way that a planar component will be directed along the vector pointing from the source to the drain while a separate through thickness (vertical) contribution will form along the polar [0001] direction of the GaN crystal due the presence of the gate [102]. These electric fields will subsequently induce strains in the material due to the inverse piezoelectric effect. Since GaN has only three independent non-zero components of the piezoelectric modulus, a shear strain is the sole component present during the operation of the TLM [122, 123]. During operation of a HEMT, this same shear strain is augmented by axial strains along each of the three principal directions resulting from the vertical field component. The final stress state of the device will then result from these induced strains and the subsequent constraint to deformation supplied by the underlying SiC and any gradients that are present in the electric field. Disparate from the 4-point bending test, it is of particular importance that the resulting stress state will have a non-zero component along the polar (parallel to c-axis) [0001] direction.

To examine if the induced stress along the polar direction affects the Raman response, a HEMT device was examined under pinch off conditions allowing for the development of inverse piezoelectric induced stresses apart from Joule heating. Shown in Figure 18 is the effect of this loading on the Raman response for each of the examined aspects of the spectrum. Similar in response to the mechanically induced stress, the peak position displays a linear dependence with increasing source-drain voltage indicating that the final stress is indeed directly proportional to the applied field. The linewidth, meanwhile, is dependent upon the inverse piezoelectric effect as well. This result is contrary to the initial 4 point bending investigation and indicates that the inverse piezoelectric effect distorts the dispersion to an extent that affects scattering and hence the linewidth. Thus when subject to appreciable loads arising from the inverse piezoelectric effect, such as those present during HEMT operation, the linewidth, unless in some way corrected, will

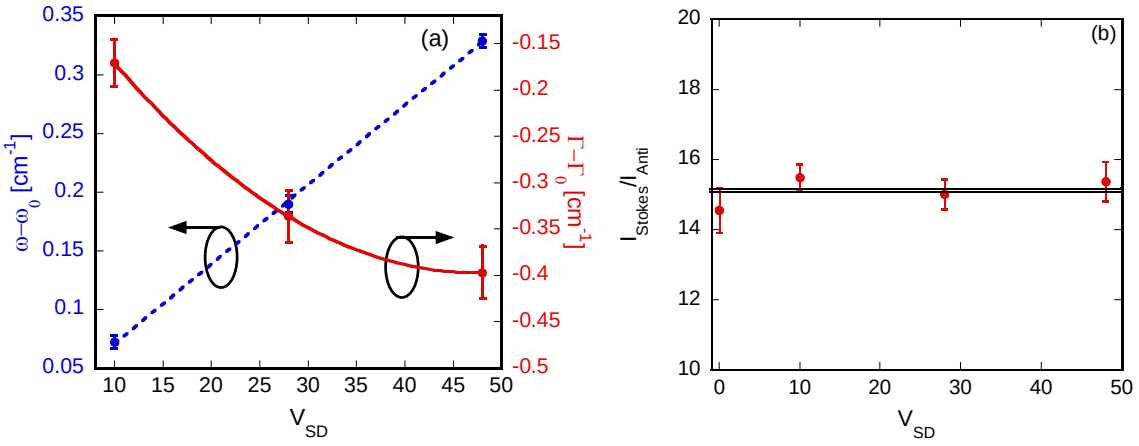

Figure 18. Effect of the inverse piezoelectric effect on (a) the Stokes peak position and linewidth and (b) the Stokes to anti-Stokes intensity ratio applied through biasing of a HEMT under pinch-off conditions. Unlike that seen for 4-Point bending test, the linewidth displays dependence to this type of loading.

induce errors in the measurement of temperature. Without a correction to the linewidth, it is then necessary to utilize the Stokes to anti-Stokes intensity ratio to measure temperature as this metric is insensitive to both types of loading as is shown in Figure 17(b) and Figure 18(b).

2.5.2.1 Origin of the Linewidth Dependence on Stresses Arising from the Inverse Piezoelectric Effect

The linewidth shows independence to stresses arising via a mechanically applied load whereas, as was shown in the previous section, its signal is acutely dependent on a load induced from the application of an electric field. It remains unclear, however, as to whether it is the electric field itself that induces the linewidth's change or instead if it is the direction of the induced stress being parallel to the polar c-axis that causes the dependence. To further investigate this question, an additional 4-point bending test was performed on a non-polar bulk GaN crystal allowing for a load to be mechanically induced along the [0001] direction. Specifically, the crystal was strained to failure both in tension and in compression while the linewidth response of the E_2^{High} mode was again analyzed.

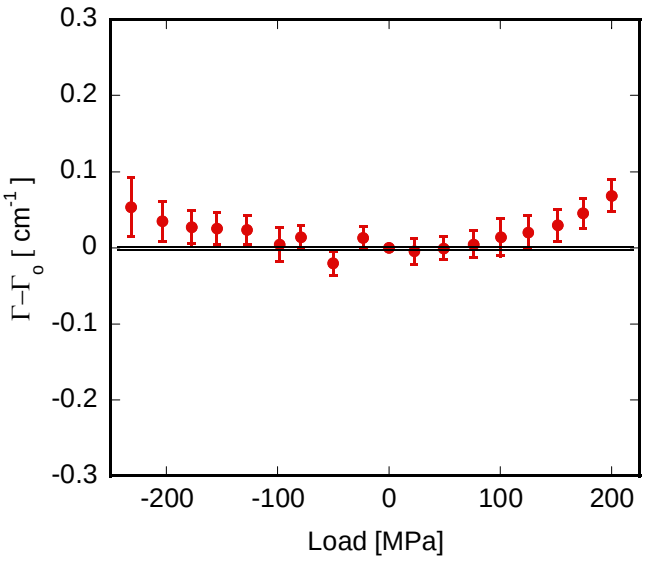

Figure 19. Dependence of the linewidth to a load in the polar [0001] direction. Although there is a degree of dependence, its magnitude is an order of magnitude less than that observed under a piezoelectric induced load. This suggests that the linewidth's sensitivity arises from a cause in addition to just the direction of the strain.

Shown in Figure 19 is the response of the linewidth to both compressive and tensile loading along the polar direction. The linewidth shows a subtle degree of dependence on this type of loading as broadening is observed to occur at heightened stress. However, the response is nearly an order of magnitude weaker when compared to the induced change due to the piezoelectric loading (see Figure 18) although the amount of stress along the c-axis is of similar magnitude in either case (see Section 3.5.3) [102]. Consequently, the direction of the load cannot be the sole causation of the linewidth's dependence on the stress induced from piezoelectric effects. Rather, the underlying cause could stem from the combination of the dominant polar load with the secondary axial and shear components or the presence of the electric field itself. Further investigation is warranted before a definitive answer can be obtained.

2.6 Measurement of Device Temperature

2.6.1 TLM Device

To investigate the capability of Raman thermometry in the presence of an evolving thermoelastic stress, a TLM device was probed at a package temperature of 85°C under dissipative powers of up to 6 W. In order to completely assess the capability of measuring temperature at these large loads, each aspect of the Raman spectrum was utilized. Regardless of the method, temperature was obtained by comparing the difference in the Raman spectra between the unpowered reference ($V_{SD} = 0$) and powered states. The spectral difference was then transformed to a temperature using the appropriate calibrations shown in Figure 14 and subsequently compared with the finite element model in order to assess the suitability of each method. At least 50 separate spectra were acquired at each experimental condition such that the resulting uncertainty in the temperature measurement was +/- 0.4, 2.0, and 4.9°C for the peak position, linewidth, and Stokes/anti-Stokes intensity ratio, respectively. A more thorough explanation of the uncertainty in the measurements will be given in a subsequent section.

The resulting trends of temperature versus power are shown in Figure 20 for each of three aspects of the Raman spectra as well as the model. Values of the measured temperature derived from both the linewidth and Stokes to anti-Stokes ratio correlate well with those of the model indicating the accuracy of each technique. Meanwhile, the evolution of the thermoelastic stress causes the peak position to under predict the temperature by as much as 50°C in manner similar to that which occurs during the operation of silicon devices [78, 106]. These results indicate the efficacy of using either

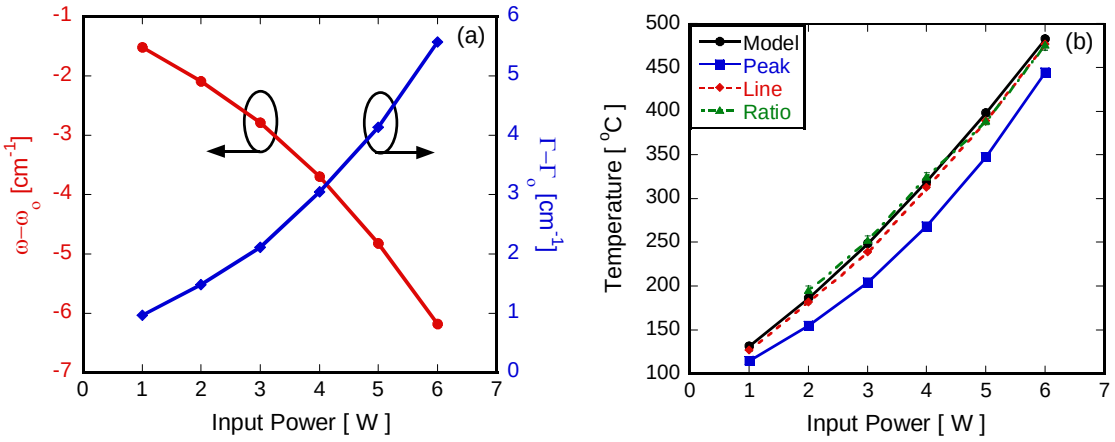

Figure 20. (a) Variation in the spectral response of the peak position and linewidth to increasing power levels in a TLM device (Note: intensity ratio is not shown). (b) Using these spectral changes with an appropriate calibration, operating temperature of the TLM device is estimated. The temperature measured using both the linewidth and Stokes/anti-Stokes ratio correlate well with the prediction of the computational model. The peak position significantly under predicts the temperature as it is affected by the presence of the evolving thermoelastic stress.

the linewidth or intensity ratio even in the presence of thermal stresses without the need for any correction procedures.

Derived from these measurements, a separate conclusion can be made about the sensitivity of the linewidth to stresses arising from the inverse piezoelectric effect. As shown in a previous section, the linewidth is modified with the application of the two dimensional electric field present during operation of a HEMT. In a TLM, this field is one dimensional in nature and acts to produce only a shear stress in the material. As the TLM cannot be operated under "pinch-off" conditions like the HEMT, it is unclear whether this shear stress will affect the linewidth. The subsequent temperature measurements using the linewidth, however, show distinct correlation with estimates of both the Stokes/anti-Stokes ratio as well as the model, thereby indicating that this shear stress induced from the inverse piezoelectric effect must minimally affect the linewidth.

Therefore, it is the vertical field acting along the polar direction of the crystal present only during HEMT operation that is the dominant piezoelectric component and causes the subsequent changes in the linewidth.

2.6.2 HEMT Device

Following a procedure similar to that undertaken in the analysis of the TLM device, the HEMT was investigated at a package temperature of 85°C under increasing levels of power dissipation up to 6.2 W (2.8 W/mm) with a source-drain bias (V_{SD}) of 28 V. Once again, each aspect of the Raman spectrum was used to evaluate temperature whereupon the efficacy of the methods was evaluated through comparison with the finite element model. In this case, at least 70 separate spectra were acquired at each experimental condition such that the resulting uncertainty in the temperature measurement was +/- 0.90, 2.5, and 4.1°C for the peak position, linewidth, and Stokes/anti-Stokes intensity ratio, respectively. Shown in Figure 21 are the derived trends for temperature versus power for each of the different techniques. Due to its sole temperature dependence, measurements derived from the Stokes to anti-Stokes intensity ratio are found to be closely correlated to the estimations of the model. The result indicates the ability of the intensity ratio to measure temperature independent of the stress state in GaN devices. Both the linewidth and the peak position, however, significantly under predict the temperature due to the influence of the complex stress state arising from the dual effects of both the piezoelectric and thermally induced loads. Consequently, in order to obtain a quick and accurate Raman thermometry method, the effects of these complex stresses must in some way be removed.

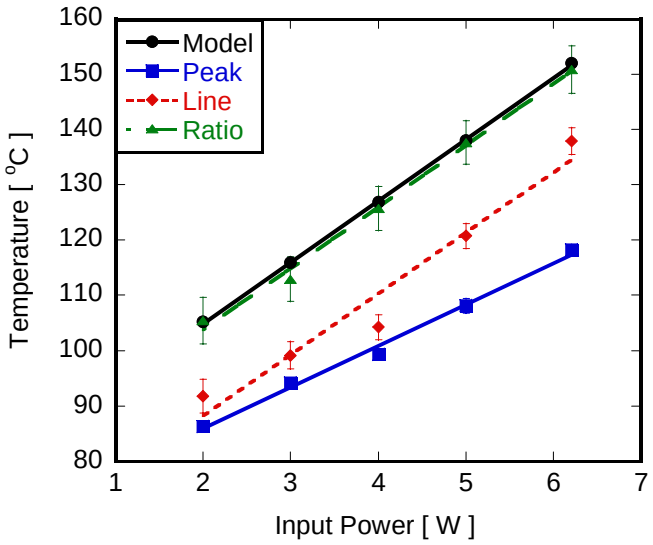

Figure 21. Operating temperature of a HEMT at a package temperature of 85°C acquired from Raman measurements derived using a standard un-powered reference condition. Only the measurements obtained from the Stokes to anti-Stokes intensity ratio correlate with the predicted operating temperatures due to this aspect's independence to both thermally and piezoelectric induced stresses.

Sarua *et al.* [102] assert that the level of piezoelectric induced stress will be similar regardless of whether the gate on the transistor channel is opened or closed. By following these results, errors in the temperature measurement due to the inverse piezoelectric effect may then be removed by simply comparing the difference in the Raman spectra between the powered and pinch-off, rather than unpowered, reference states. Practically this is implemented by acquiring the reference state (ω_o, Γ_o) under the pinch off conditions (V_{SD} = 28 V, V_G = -8 V) rather than the completely unpowered state (V_{SD} = 0 V, V_G = 0 V) and, once again, measuring the operating temperature of the HEMT. As shown in Figure 22, it is clear that indeed the piezoelectric contribution may be removed using the pinch off reference condition as the measurements of temperature derived from the linewidth now show clear correlation to both the estimates from the

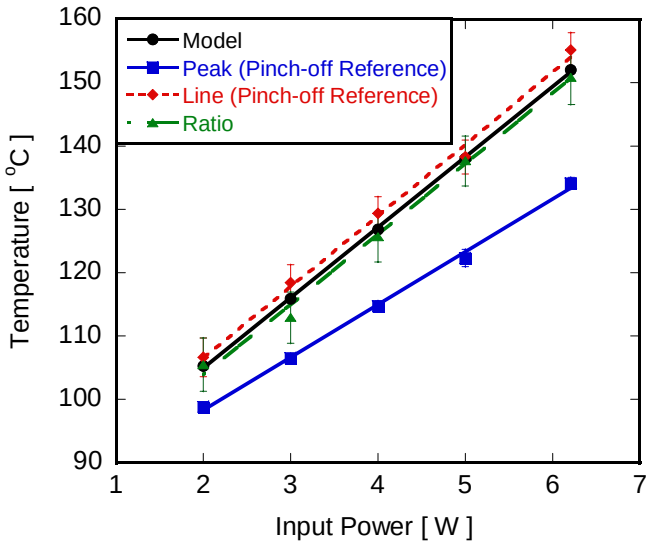

Figure 22. Operating temperature of a HEMT measured using Raman spectroscopy with a reference taken under pinch off conditions. Using this non-standard reference condition allows for piezoelectric induced effects to be removed thus allowing for the accurate measurement of temperature through use of the Stokes linewidth.

intensity ratio as well as the model. However, despite the removal of the piezoelectric contribution, the peak position continues to under predict temperature as thermoelastic stresses remain a significant source of error. Nonetheless, through utilization of the pinch off reference condition, the linewidth allows for a Stokes based Raman temperature measurement independent of the complex stress states that arise during GaN transistor operation.

2.7 Uncertainty in the Measurement of Temperature

Uncertainty in the predicted values of temperature stem from a variety of factors that influence the calculation of the position, intensity, and shape of the Raman peak. These sources of error arise from changes in the actual spectrometer during testing, variation in the sampled volume due to drift in the microscope's stage, spatial non-uniformities in the device response, or differences in the fitted spectra due to the inherent difficulty in fitting

a continuous Voigt function to a discrete "pixelated" data set. To then quantitatively assess the accumulated uncertainty that is present due to each of these factors, the method of Kline and McClintock was utilized to vector sum the individual components present in the experiment [124].

Mathematically, this is accomplished through analysis of the equations predicting the temperature from a change in the analyzed spectral component. With respect to the peak position based measurement, Equation (16) is first solved for temperature,

$$T = \frac{\omega - \omega_o}{A} + T_o . \tag{19}$$

The individual uncertainties may then be linked to the final uncertainty in the measurement of temperature through analysis of Equation (19) as is shown below:

$$\delta T = \left\{ \left(\frac{\partial T}{\partial A} \delta A \right)^2 + \left(\frac{\partial T}{\partial \omega} \delta \omega \right)^2 + \left(\frac{\partial T}{\partial \omega_o} \delta \omega_o \right)^2 \right\}^{1/2} . \tag{20}$$

In Equation (20), δT , δA , $\delta \omega$, and $\delta \omega_o$ are estimates of the 95% confidence intervals for the temperature, calibration constants, and peak position at the tested and reference conditions, respectively. In the above relation, it is assumed that the reference temperature, T_o, remains constant throughout testing. The confidence intervals, themselves, were reduced through the acquisition of multiple spectra during both calibration and testing. As the resulting data sets maintained a Gaussian distribution as verified using Pearson's Chi-Square examination, the confidence intervals, δX , were then calculated from the standard deviations, σ_{st} , of the acquired data set as given in the relation below:

$$\delta X = \frac{1.97 \sigma_{st}}{\sqrt{n}} \tag{21}$$

where n is the number of acquired data points. In all data sets, outliers were defined according to Chauvenet's criterion [125]. Analogous procedures using Equations (17) and (18) for the linewidth and intensity ratio, respectively, were implemented as well allowing for the uncertainties in the totality of the measurements to be obtained.

The resulting uncertainty in the measurement of temperature for both the TLM and HEMT is shown in Figure 23 as a function of the dissipated power. All uncertainty was found to be less than 5% of the resulting magnitude of the temperature measurement. Due to its extensive nature and non-linear response, the intensity ratio exhibits the greatest level of uncertainty as any drift in the optics of the spectrometer or the optical properties of the tested device tend to increase the scatter in the resulting measurements. This problem is circumvented in the peak position and linewidth based methodologies owing to the fact that only a relative change is measured and hence any drift in the system or device can be accounted for through use of periodic reference measurements

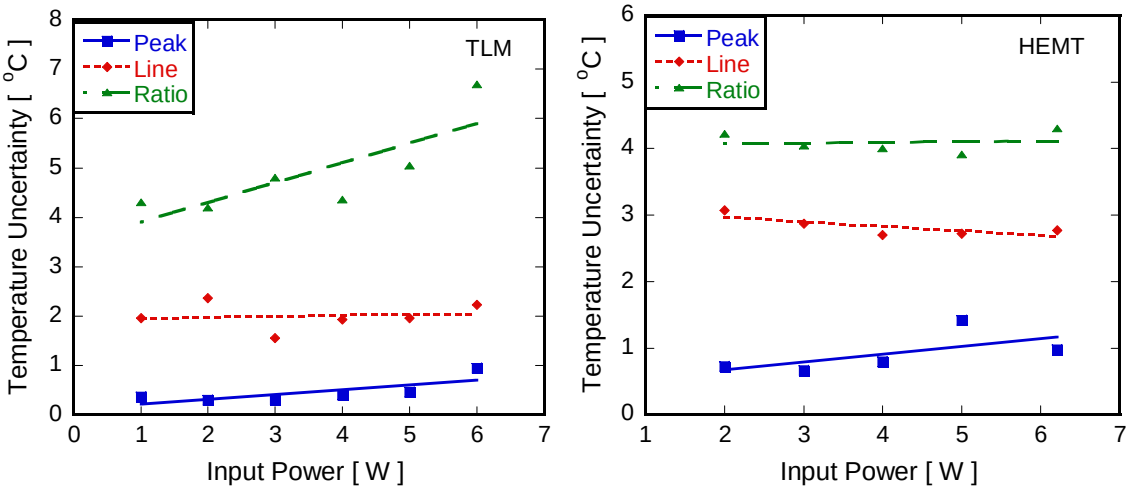

Figure 23. Uncertainty in the measurement of temperature for both the TLM (left) and HEMT (right) devices. All errors are found to be less than 5% of the resulting temperature measurement.

taken throughout the analysis.

Not only is the measurement itself affected by the difficulty of an extensive based measurement, but so too is the calibration. In fact, the total uncertainty in the intensity measurement stems from a comparable degree of scatter between both the measurement and calibration. In contrast, the intensive measurements exhibit uncertainties dominated by the acquisition of the spectral components themselves, rather than their calibration, as the latter source is found to be of second order. The scatter in the acquisition of the spectral components stems from sources including not only those due to drift in the spectrometer but also from uncontrollable changes in the actual volume being interrogated. These changes in volume occur due to the impossibility of perfectly fixturing a device throughout the acquisition of the Raman signal. Due to this non-ideal fixturing, the device's position randomly moves with respect to the focal point during acquisition of the signal (~6 minutes/data set). As this movement occurs in a region of appreciable thermal gradient, the resulting acquisitions of the spectral components will then demonstrate heightened scatter. It is believed that this positional drift is the main source of the uncertainty in the resulting temperature measurements and the reason that the HEMT, which is subject to larger gradients, exhibits greater scatter than the TLM (see Figure 23).

The level of uncertainty is found to remain relatively constant for all measurements regardless of the temperature measured. The constant level of uncertainty, even as the magnitude of temperature increases, is in direct contrast to previous studies that have specified that scatter during Raman thermometry measurements increases with temperature [78, 126]. This study, however, unlike those previous, adjusted acquisition

times such that the signal to noise ratio (SNR) remained constant throughout all measurements and for all temperature levels. This change allows for more constant fitting of the spectrum and hence reduced scatter in the resulting predictions.

2.8 Validity of the Through Thickness Average Assumption

2.8.1 Virtual Raman Investigation

Implicit in the measurement of transparent materials, and GaN in particular, is the probing of the entirety of the material in question. As the vast majority of devices have through thickness temperature variations, it is necessary to investigate the manner in which the Raman signal, and subsequent temperature measurements, is modified by the thermal gradient. Typically, it is assumed that the resulting signal is the average temperature through the thickness [54]. To quantify the validity of this assumption, a "reverse" Raman thermometry investigation is performed in which a known thermal gradient was used to estimate a virtual Raman response. The virtual Raman response is then analyzed to calculate the resulting peak position and linewidth whereupon the "measured" temperature is found and compared to the average value through the layer defined by the specified temperature profile.

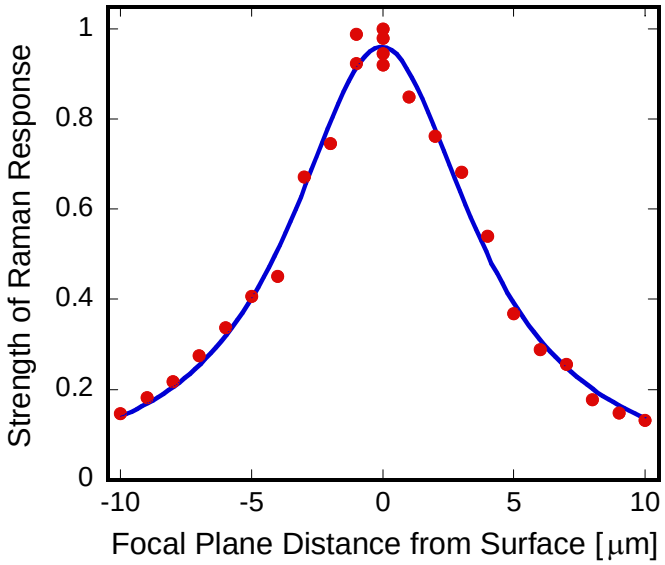

Figure 24. Through thickness response function of the spectrometer to an AlGaN/GaN HEMT. As the FWHM of this curve is 9.16 μm and the thickness of the GaN layer is less than 5 μm, the resulting spectrum will then be affected by the entirety of the GaN

Practically, this assessment occurs by first acquiring the through thickness response function of the spectrometer. This response function describes the sensitivity of the spectrometer to material away from the focal plane and is acquired by successively comparing the intensity of the Raman signal as the focal plane is moved above and below the surface of the material of interest [127]. By analyzing an AlGaN/GaN HEMT in this manner, the response function was obtained and is shown in Figure 24. The acquired response has a FWHM of 9.16 μm meaning that when a GaN device's surface is analyzed, material at a depth of ~5 μm from the surface will influence the resulting curve at a weight of ½ that of the focal plane. As the thickness of the GaN layers is less than this 5 μm, the entirety of the thickness will then affect the resulting Raman signal and, as expected, the subsequent temperature measurement.

To assess whether this interaction may be accurately quantified through the oft employed assumption of a through-thickness average, a linear temperature gradient is assumed to exist in a 2 μm thick portion of GaN. The gradients are varied such that the resulting temperature differences in the layer range from 10-50°C with the associated maximum temperature varied from 85-500°C. The layer itself is separated into 500 separate computational regions and a temperature is assigned to each region according to the assumed gradient and maximum device temperature. Using these temperatures and the calibrations of the linewidth and peak position, an equivalent Raman spectrum is subsequently constructed for each of these computational regions. The composite signal, analogous to that which would be acquired in an actual experiment, is obtained by summing each computational region's response in a manner that is weighted according to the response function shown in Figure 24. This composite signal is fitted using the curve fitting procedures previously described and the resulting "measured" temperature found according to the appropriate calibration. The "measured" temperature is then compared to mathematical mean of the assumed temperature gradient in order to assess the validity of the through thickness assumption.

Shown in Figure 25 is the result of this procedure for both the peak position and linewidth based measurements. It is found that for all gradients and temperature levels considered here, the difference between the peak position's prediction and the through thickness average differs by less than a degree. This difference is comparable to the level of uncertainty in the measurement, and therefore, the assumption of a through thickness average seems to be appropriate when utilizing the peak position. The same conclusions can be reached for the linewidth when the gradient is below 15°C/μm or the maximum

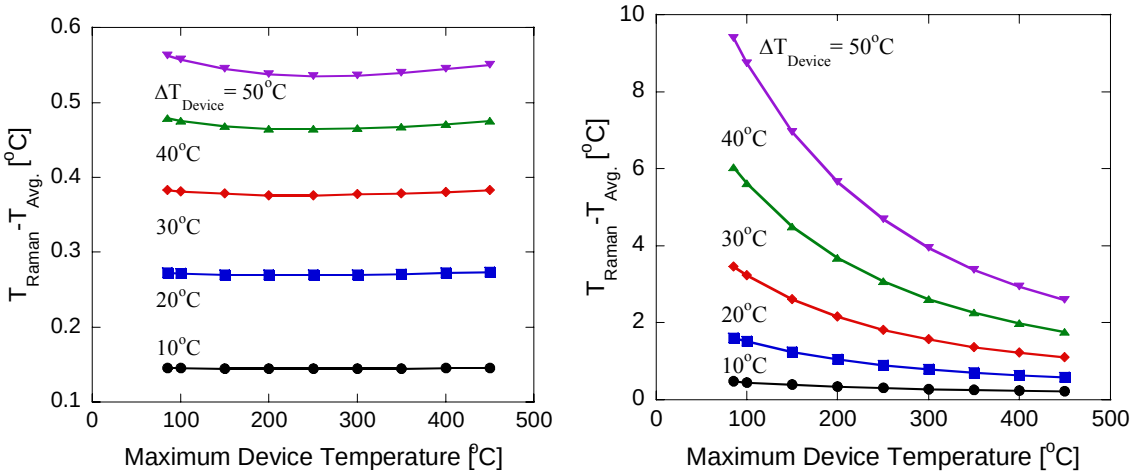

Figure 25. Difference between Raman prediction and average temperature using the peak position (left) and linewidth (right). The assumption of a through thickness average holds in all circumstances when utilizing the peak position, but caution must be taken at lower temperatures when incorporating the linewidth.

temperature remains above 200°C. Under conditions of low operating temperature and high gradient, however, differences between the average temperature and the measurement become far larger than the uncertainty thus giving pause to the use of this assumption.

2.8.2 Experimental Investigation

Adopting the assumption of a through thickness temperature average during Raman thermometry of GaN devices necessitates that the gradients within the material remain reasonable. Near the drain side of the gate, however, substantial thermal gradients arise in conjunction with the formation of the hot spot. Although these vertical gradients dissipate at locations closer to the drain, it remains unclear whether the mitigated field present at the location of the measurements (midway between the gate and drain) limits the applicability of the through-thickness average assumption. To assess the validity of

the utilized assumption, a series of 30 AlGaN/GaN HEMTs grown atop a silicon substrate were analyzed with respect to their operational temperature response. By comparing the evolution of temperature both within the GaN and the underlying silicon through the simultaneous acquisition the Raman signal for each material, the magnitude of the through thickness temperature gradient may be qualitatively examined and the validity of the through thickness average further evaluated.

AlGaN/GaN HEMTs grown on silicon substrates are particularly applicable to this analysis due to material properties of the Si itself. First, the lower thermal conductivity of silicon, as compared to SiC, induces larger temperature increases with power dissipation in the device. These larger temperature increases, and the enhanced thermal resistance of the overall device, will lead to heightened thermal gradients and a more rigorous examination of the assumption. Secondly, the Raman response of silicon is particularly large at a wavenumber of ~520 cm^{-1} while the examined GaN mode is located near 568 cm^{-1}. It is then possible, due to the transparency of the GaN and the spectral similarity in the responses, to measure each material's temperature evolution simultaneously in a single acquisition of the Raman signal. Taking advantage of these facts, each of the 30 transistors were examined at conditions analogous to those described in Sections 2.3.4 and 2.6.2.

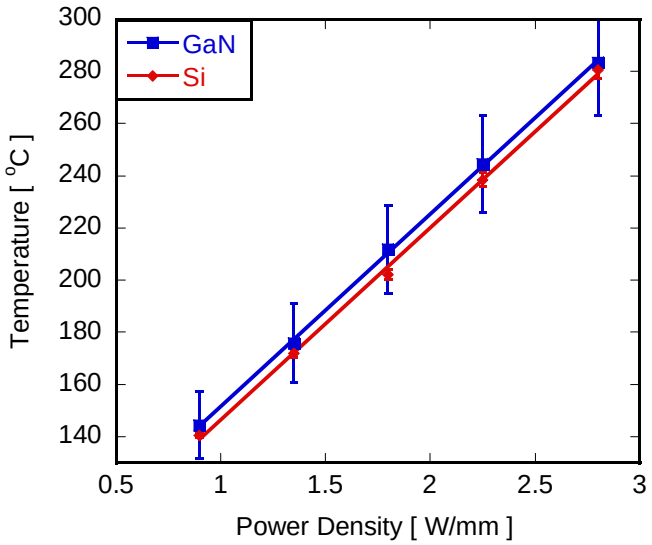

Figure 26. Temperature as a function of power density within both the active GaN layer and underlying Si substrate for an AlGaN/GaN HEMT. The resulting temperatures of each layer are nearly identical indicating that the through thickness temperature gradients in the region of the experiment are small, thus validating use of the through thickness average assumption for the resulting thermal measurements .

Shown in Figure 26 are the resulting temperature measurements at increasing levels of power density for both the GaN and Si layers. For all power inputs, the thermal response is nearly identical for both the active GaN and underlying Si substrate. Notice, however, that while the GaN is transparent and, as such, information is acquired throughout the entirety of this layer, Si is opaque in the visible region of the spectrum. Therefore, the acquired temperatures of the Si correspond to the thermal level within the first 1 μm of the substrate. The near equivalence in the temperatures between the two materials then seems to indicate that the measured values of the GaN are favorably weighted at depths near the interface as has been hypothesized previously [63]. In the previous section, however, it was shown that the spectrometer samples the entire GaN layer with minimal weighting (see Figure 24) rendering this deduction obsolete. Thus,

for the entirety of the GaN layer to demonstrate a temperature nearly equivalent to that of the underlying silicon, it must be reasoned that the through thickness temperature gradient is relatively small at the location of the measurement. In light of this fact, the use of the through thickness assumption for both the peak position and linewidth based Raman thermometry methods remains reasonable for the devices analyzed in this study.

2.9 Summary

Operating temperature is a key determinant in both the reliability and performance of GaN devices, thus making measurement of this parameter central to further development. Raman thermometry is an attractive tool for the acquisition of these temperatures as it is non-invasive and has the potential for spatial and temporal resolution on par with that of the device. Thermal measurements derived from Raman are subject to errors, however, when the oft employed Stokes peak position is utilized owing to this spectral component's dependence to not only temperature, but also thermoelastic and piezoelectric stresses. To assess the magnitude of these errors and circumvent their inclusion, this study has investigated the totality of the Raman response in the presence of these stress effects. Owing to the significant dependence of the peak position to the analyzed loads, temperature measurements derived from this portion of the spectrum were found to significantly under predict in comparison to those acquired utilizing the stress independent Stokes to anti-Stokes intensity ratio, highlighting the need for an alternative Raman thermometry procedure. The linewidth of the same Stokes signal offers this alternative as it is capable of measuring temperature apart from stress effects through adoption of a proper reference condition that removes piezoelectric induced biasing. By implementing the linewidth, temperature measurements may then be

acquired apart from stress induced biasing through sole use of the Stokes signal allowing for a mitigation of both thermal uncertainty and measurement duration.

CHAPTER 3

ASSESSMENT OF RESIDUAL, PIEZOELECTRIC AND THERMOELASTIC STRESS LEVELS IN ALGAN/GAN HEMTS

3.1 Overview and Approach

The tremendous capability of gallium nitride HEMTs exists as a direct result of large carrier concentrations (~10^{13} cm^{-2}) that accumulate along the interface between the AlGaN and GaN layers due to the presence of both spontaneous and piezoelectric polarizations. While the spontaneous contribution is linked to the crystal structure itself, the degree of piezoelectric polarization is proportional to the level of strain, and hence stress, present in the device. As a consequence, the carrier concentration, and in turn the resulting performance of the HEMT, is intrinsically linked to the stress level that evolves during operation [25, 128, 129].

The presence of this operational stress determines not only the level of HEMT performance but so too the long term viability of its operation as reliability is linked not only to operational temperature but the stress level as well [12, 35, 36]. The bond linking reliability and stress stems from defect generation during device operation in response to both thermoelastic and inverse piezoelectric effects. These defects act as traps for the transport of electrons and with their continual accrual comes degradation and eventual device failure [36]. Thus, it is of extreme relevance to measure the source of these defects, namely the stress, in order to further refine both the capability and overall device lifetime of AlGaN/GaN HEMTs.

Full quantification and analysis of the stress necessitates investigation of each of the components that give rise to the total load placed on the device. For AlGaN/GaN HEMTs, three distinct biaxial contributions are at play, namely, the residual, thermoelastic, and inverse piezoelectric stresses. The residual stress evolves as a consequence of the processing schemes employed during fabrication and may be thought of in the context of an "as is" stress that is present at ambient conditions when the device is not in operation. Raman spectroscopy has been frequently employed to measure these residual stresses at ambient temperatures through monitoring of the change in the Stokes peak position from its "true" stress-free value [62, 99, 130-132]. In a similar fashion, Sarua *et al.* [102] propose a complementary methodology by which a change in peak position due to the application of bias on a HEMT is used to quantify the level of piezoelectric induced stress on a device.

However, as described in Chapter 1, the sole use of the peak position in this manner to measure the thermoelastic stress that evolves during device operation is impossible due to the dual dependence of this aspect of the signal on strains arising from both thermal expansion and elastic effects. Due to this difficulty, there has, as yet, been no quantification, Raman or otherwise, to this key portion of the total stress. Furthermore, it has been impossible to assess the magnitude of the total load present in the AlGaN/GaN HEMT or to identify the stress component that is most dominant.

As the peak position displays linear dependence to both temperature and elastic stresses, it is possible to extend the Raman technique to estimate operational stress through use of an additional aspect of the Raman response that is independent to strain. The independent parameter allows for the estimation of temperature that, in turn, allows

for the effects of thermal expansion to be removed from the peak position response. With this effect removed, the peak position is singularly dependent on the stress and can be assessed using only calibrated response of the peak position to elastic deformation. Recently, this approach has been implemented using the linewidth (FWHM) of the same Stokes response to successfully measure evolution of biaxial thermoelastic stresses during operation of silicon based MEMS devices [106]. In GaN devices, an analogous approach should be applicable considering that the effects of both thermal and piezoelectric induced strains may be separated from the linewidth as was reported in Chapter 2 [133]. As such, use of the Stokes peak position and linewidth in tandem may then be employed to measure the operational biaxial thermoelastic stress, thus allowing for a full interrogation of the HEMT's mechanical environment.

To demonstrate the method, the operational stresses in three separate devices were examined experimentally. First, in order to limit the difficulties imposed due to piezoelectric induced stresses, viability of the technique is queried through examination of the thermoelastic stresses that occur during electric heating of a silicon based MEMS device and then compared for accuracy against a finite element model of the system. Subsequently, the same TLM and HEMT structures examined in Chapter 2 were once again investigated to estimate the operational thermoelastic stress in a GaN based system. The efficacy of the method was then judged based on comparison between the measured results and the coupled finite element model of the system [134]. With confidence in the measurement of operational thermoelastic stress, the role of substrate on the mechanical milieu is pursued through analyses of a series of AlGaN/GaN HEMTS built atop either silicon (Si) or silicon carbide (SiC). For each type of device, the residual, piezoelectric,

and thermoelastic stress are compared in order to weigh the relative contribution of each component. In such a way, the dominant stress component is identified in AlGaN/GaN HEMTs experimentally for the first time.

3.2 Measurement of Operational Stress Using Raman Spectroscopy

Stress measurements derived from Raman spectroscopy rely on observations of changes in the location of the Stokes peak position. These changes may be related to the to the stress level via Equation (22) shown below,

$$\omega_s - \omega_o = D\sigma \tag{22}$$

where ω_s is the change in Stokes peak position due to stress relative to its reference position ω_o, σ is the stress, and D is a known calibration constant [106]. Of extreme importance is the fact that this calibration constant does not relate any change in the peak position to a corresponding stress. Rather, it relates a known stress state (e.g., biaxial, hydrostatic, etc.) at a *given temperature* to a frequency change. In the case of thin film devices, the stress evolves in an overwhelmingly biaxial fashion requiring that the resulting calibration of D then be acquired in this stress state. As shown previously, a similar relationship, Equation (16), links a frequency change at a *given magnitude and state of stress* to a corresponding temperature.

As both Equation (16) and (22) are linear, subject to a combined thermomechanical field, the resulting change in peak position is a superposition of each effect,

$$\omega_{Tot} - \omega_o = D\sigma + A'(T - T_o) \tag{23}$$

where ω_{Tot} is the total change in peak position due to both temperature and stress while A' is a calibration constant relating the response of the peak position to temperature under

stress free conditions. Due to this superposition, investigations of devices while in operation result in 2 unknowns (temperature - T and stress - σ) accompanied by a singular measurement (ω_{Tot}), making estimation of either parameter most difficult.

Measurement of the operational stress through use of the peak position thus necessitates an independent measurement of temperature. Practically, this may be accomplished in a singular acquisition of the Stokes response through utilization of the linewidth to acquire a stress independent measurement of temperature using the methods delineated in Chapter 2. Thus, through rearrangement of Equation (23) and the stress independent measurement of temperature acquired through the linewidth, the operational stress of a device at elevated temperature is described as demonstrated below:

$$\sigma = \frac{(\omega_{Tot} - \omega_o) - A'(T - T_o)}{D}. \tag{24}$$

Although at first glance it may appear that Equation (24) allows for the measurement of any themoelastic stress, its use is limited to systems having an analogous stress state to that which was calibrated. As most of the thin films comprising an electronic device evolve a biaxial thermoelastic stress during operation, analysis must then take place with a calibration constant, D, acquired under these conditions.

3.3 Measurement of Operational Stress in Silicon MEMS Devices

3.3.1 Sample Preparation

To investigate the thermal stress evolution in a MEMS structure during operation and simultaneously demonstrate the technique apart from complications arising from piezoelectric sources, polysilicon microheaters were analyzed using a micro-Raman mapping procedure. The device consisted of a phosphorous doped polysilicon beam

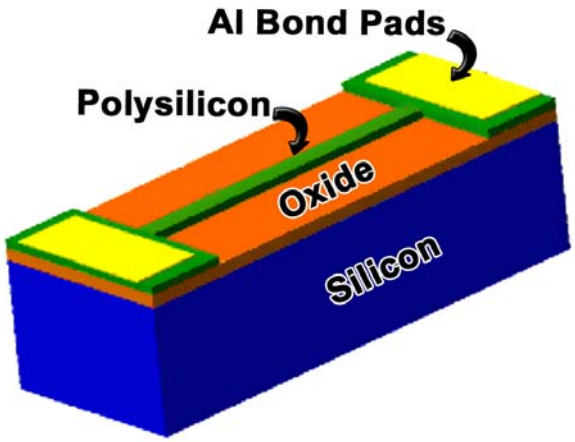

Figure 27. Schematic of polysilicon doped microheater measuring 300 μm long by 10μm wide.

deposited on a 3.9 μm thick layer of thermal oxide, which rested on a 500 μm thick layer of silicon. The microheater was 10 μm wide by 300 μm long and had a thickness of 2.2 μm. The final doping of the microheater was 10^{20} atoms/cm^3 and was achieved using an ion implantation procedure. Details of the fabrication scheme can be found elsewhere [135]. A schematic of the structure is shown in Figure 27. The devices were used without releasing them from the underlying oxide layer in order to constrain the deformation of the beam creating appreciable levels of thermal stress during operation.

3.3.2 Calibration of the Silicon Response to Temperature and Stress

The temperature response of the Stokes peak and linewidth were measured for a monolithic single-crystal silicon sample, which was mounted in an unconstrained manner as part of a temperature controlled stage (Linkham TS-1200). Raman spectra were acquired in 100°C increments from ambient to 500°C as described elsewhere [136, 137]. Twenty five spectra were taken at each temperature with acquisition times adjusted to

obtain a Stokes peak with at least 6000 CCD counts. The values of the Stokes peak position and linewidth at each temperature, determined from Voigt curve fitting of the spectra, were used to calibrate the Raman response versus temperature. The peak position and linewidth show a linear and parabolic fit similar to that seen in Figure 14 for GaN with calibration constants that compared well with those reported in the literature [126, 131]. A second calibration curve for the linewidth was then found using the four phonon process model first proposed by Balkansi *et al.* [73, 138]. The resulting fit agreed to within 1% of the empirically derived parabolic curve. Using this model, the Raman linewidth at 0K was found to be within 5% of the value obtained by Hart *et al.* [74] indicating the pertinence of the calibration methods employed.

It should be noted that the calibration of linewidth as a function of temperature depends on the microstructure of the material; a smaller linewidth is observed with improved crystalline quality and larger crystal size that results from longer phonon lifetimes as per Equation (8) [139]. However, the relative change in linewidth ($\Gamma - \Gamma_o$) is much less dependent on microstructural effects. The change in linewidth with temperature arises due to phonon-phonon scattering mechanisms whose rate is primarily determined by the temperature dependent population of the phonons available for scattering. While defects in the microstructure can increase phonon-impurity scattering and broaden the Raman linewidth, the defect's contribution to temperature dependent changes is small as compared to phonon-phonon scattering. This is true as long as the microstructure remains stable with increasing temperature. This effect is seen in Figure 28 where the relative change in Raman linewidth ($\Gamma - \Gamma_o$) is plotted for several polysilicon and single-crystal silicon samples. When the offset, Γ_o, is subtracted, all of the data

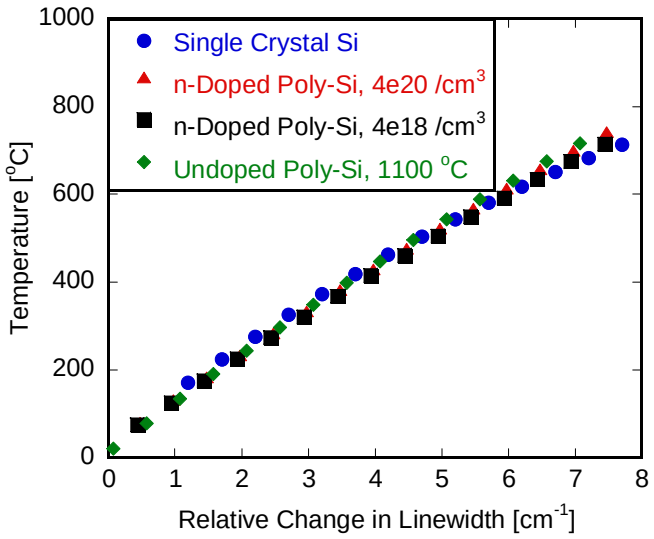

Figure 28. Relationship between temperature and relative linewidth for single crystalline and several polycrystalline silicon samples. Data show that the temperature versus relative linewidth change is very similar regardless of the microstructural aspects of the silicon sample.

collapse to a single curve which suggests that the calibration of single-crystal Si can be applied to the samples in our study. By using single crystalline Si, it is ensured that the calibration of temperature dependent Raman characteristics comes from a stress-free sample for our analysis.

A calibration was also performed to determine the Raman response of the (001) plane under an applied stress along the [100] direction of single crystalline Si. Using a four point bending stage, the response of silicon to various levels of stress was analyzed both in compression and tension as described elsewhere [136, 137]. The Stokes peak position was found to vary linearly with stress (D = -3.6 cm^{-1}/GPa, Equation (24)) at a rate within 10% of the predicted biaxial constant given by De Wolf [131]. Although the four point bending procedure strains the material in a uniaxial fashion, this calibration is

equally valid for biaxial stress within the same crystal plane [140]. Consequently, its use is warranted for the current analysis. The linewidth, however, showed no detectable dependence on the state of stress.

With knowledge of the thermal and mechanical response of silicon, full temperature and stress fields were obtained on the polysilicon microheater through incorporation of a mapping procedure. The mapping procedure was carried out using an automated x-y stage with 0.5 micron resolution. Raman spectra were sampled at 2 μm intervals across the beam width and 6 μm periods along the length. Acquisition times were once again varied to obtain Stokes peaks with intensities of at least 6000 CCD counts on the microheater for each level of power dissipation.

Thermal stress evolution was probed by first taking a map of the beam at room temperature to account for residual stress in the beam. The values for peak position and linewidth obtained during this initial ambient scan were then incorporated as ω_o and Γ_o at each measurement point during subsequent powered scans for use in Equations (16) and (17). In this manner, the biaxial thermal stress evolution was analyzed at powers of 240 and 480 mW. Total stress (i.e., both residual and thermal) can be found if reliable values for the peak position and linewidth are known for a particular material and microstructure at ambient stress free conditions. In this study, only thermal stress evolution was examined as this allowed for a more direct comparison to a finite element model.

3.3.3 Temperature Mapping of Si Microheaters

Figure 29 displays the 2D temperature maps of the microheater as a function of heater input power. The temperatures were observed to be nearly uniform throughout the microheater at each power level. Only near the ends of the microheater, where the

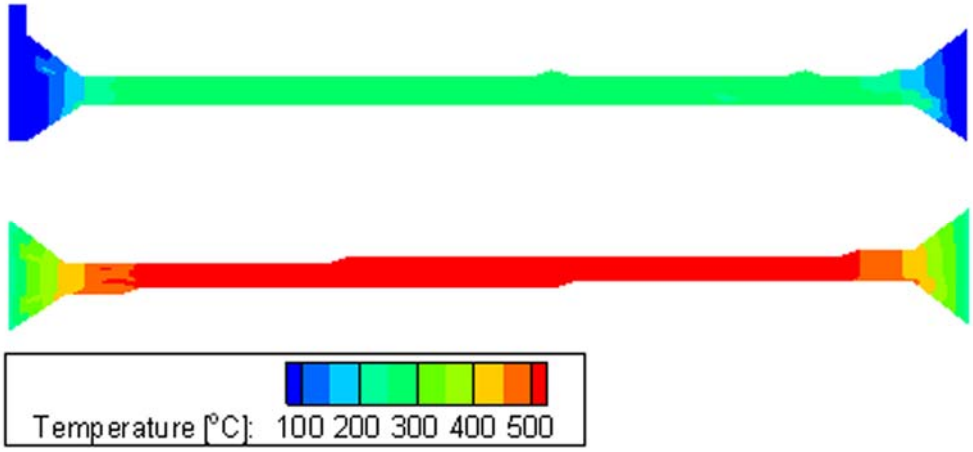

Figure 29. Temperature (°C) maps of the beam at 240 mW (top) and 480 mW (bottom).

interconnect pads serve as a thermal sink, is there an appreciable temperature gradient. Since the stress distribution should follow the temperature distribution, this mapping procedure indicates that the stress should be relatively constant in the middle of the heater as well. Such simple physical profiles provide a known response against which the measured values of stress and temperature can be compared, and from which the precision in the measurements can be estimated from the scatter in experimental data.

A comparison between the Stokes peak shift (Equation (16)) and linewidth (Equation (17)) based temperature profiles of the powered microheater are shown in Figure 30. The results show a significant difference between the two measurements, being on the order of 30°C at 240 mW and 60°C at 480 mW of dissipated power. Considering the fact that the uncertainty in ambient stress measurements using Raman is normally reported to be approximately ±25 MPa for silicon [141], this would correspond to a temperature difference between the two methods of ±4.1°C. As shown in Figure 30, the discrepancy between temperature measurements is much greater than this threshold, indicating that significant stress is present in the device, as expected. Furthermore, since the predicted

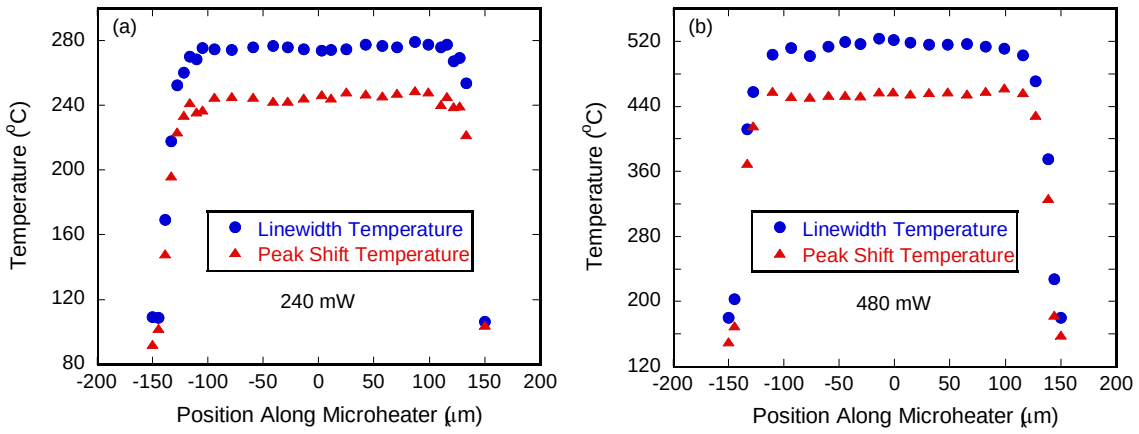

Figure 30. Temperature distribution across the length of the microheater when dissipating 240 mW (top) and 480 mW of power (bottom). The peak based method significantly under predicts the temperature indicating, as expected, that the beam is under a compressive stress.

peak position based temperature is less than the linewidth-based value, a compressive stress is anticipated. The next sections will enumerate how to quantify this stress in a manner that minimizes uncertainty.

3.3.4 Uncertainty in the Calculation of Stress

The uncertainty in the stress measurement is predominately controlled by the deviation in the measurement of the Stokes linewidth. The effect of this deviation on the estimation of stress can be examined analytically using Equation (24) and vector summing the component uncertainties:

$$\left(\delta_\sigma\right)^2 = \left(\frac{\partial\sigma}{\partial\Delta\omega}\delta_{\Delta\omega}\right)^2 + \left(\frac{\partial\sigma}{\partial T}\delta_T\right)^2 \tag{25}$$

where $\Delta\omega = \omega_{Tot} - \omega_o$ and T corresponds to the measured temperature. Equation (25) ignores the contribution to uncertainty arising from the calibration of the Si response to

stress as it was found to be of second order, thus allowing for the relation to be rewritten as:

$$\left(\delta_\sigma\right)^2 = \left(\frac{1}{D}\delta_{\Delta\omega}\right)^2 + \left(\frac{A'}{D}\delta_{T_\Gamma}\right)^2 \quad . \tag{26}$$

The ratio of *A'/D* is 6.1 MPa/°C for silicon, which results in a significant amount of stress uncertainty for only a small deviation in the measurement of temperature regardless of preciseness in measurement of the peak position. As a consequence, it is imperative to reduce the variation in the measurement of temperature either through the use of superior experimental hardware or the employment of multiple measurement realizations. In a mapping procedure like the one employed here, however, multiple acquisitions are untenable and hence reductions in uncertainty must be attained via an alternative route.

To estimate the inherent uncertainty in the method, stress free single-crystal Si was inserted into a Linkham environmental test stage and heated to temperatures between 100 and 500°C. A total of 25 Raman spectra were taken at each temperature in order to obtain a suitable distribution of the peak position and linewidth. By measuring the change in peak position and calculating the temperature from the change in linewidth using Equation (17), a 95% confidence interval was calculated to obtain $\delta_{\Delta\omega}$ and δ_T, respectively. Using Equation (26), the variation in stress was found to be on the order of +/- 40 MPa for a set of 25 acquisitions as is typically utilized in a standard measurement. Additional acquisitions were not seen to significantly change the distributions and hence this magnitude will be used as the intrinsic scatter in the silicon measurements for the rest of this study.

3.3.5 Determination of Stress in Si Microheaters from Mapping Procedure

Moderate levels of noise in the measurement of the linewidth-based temperature can introduce significant scatter in the measured stress profiles. This fact is exacerbated when only a singular acquisition is acquired as is the case in a mapping operation. To mitigate this effect towards a level on par with that of a standard measurement in which at least 25 acquisitions are utilized, the measured thermal values were fit to an expected functional form of the temperature profile. The unreleased beam structure was modeled by considering an energy balance between 1D axial conduction, uniform Joule heating, and lateral heat losses that were proportional to the surface area and local temperature. With constant thermal conductivity and electrical resistivity, the governing differential equation for this steady state heat transfer problem is given by:

$$\frac{d^2\theta}{dx^2} - M\theta + Q = 0 \tag{27}$$

where x is the axial position along the heater, and $\theta = T(x) - T_{ref}$ is the difference between the local heater temperature and an appropriate reference temperature, M is a parameter describing the relative importance of lateral heat losses to axial conduction, and Q represents the relative importance of Joule heating to axial conduction. The solution to Equation (27) is given by

$$\theta(x) = \frac{Q}{M^2} + K_1 \sinh(Mx) + K_2 \cosh(Mx) \tag{28}$$

where K_1 and K_2 are constants.

By using Equation (28) to fit the temperature found using the linewidth, the uncertainty in the measurement of stress may be reduced to the intrinsic value (i.e., +/- 40 MPa) of a normal measurement apart from the mapping operation thereby allowing a

suitable stress map to be obtained with only one acquisition. While the specific functional form shown in Equation (28) works well for MEMS with 1D conduction, it may also be possible to use other generalized functions such as polynomials, Fourier series, etc., to fit data sets for arbitrary geometries. The use of generalized functions, however, requires additional assessment to determine the appropriate order of the function to be used in order to ensure there is no reproduction of high frequency scatter in the data. The need for this type of filtering function can be removed with a reduction of the uncertainty in the measurement of temperature.

3.3.6 Comparison of Mapping Results to Finite Element Models

To verify the calculation of stress obtained from the Raman mapping procedure, a separate finite-element model was developed using ANSYS 9.0 with multi-physics elements for the Si microheater. Temperature dependent values for the thermal conductivity and thermal expansion coefficient were employed, while other material properties were assumed constant for each of the three materials: polysilicon, silicon dioxide, and silicon [142].

The model itself incorporated a fine mesh in the polysilicon beam and silicon dioxide layers to accurately resolve the temperature and stress distribution. The temperature measurements, smoothed using Equation (28), were used as the surface boundary condition of the beam in the thermal analysis [135]. An additional boundary condition was obtained by placing a thermocouple on the backside of the silicon substrate during operation of the microheater. Mechanical boundary conditions were incorporated that negated vertical displacement on the bottom of the substrate while fixing the two orthogonal edges leaving the opposite faces free to expand within the plane.

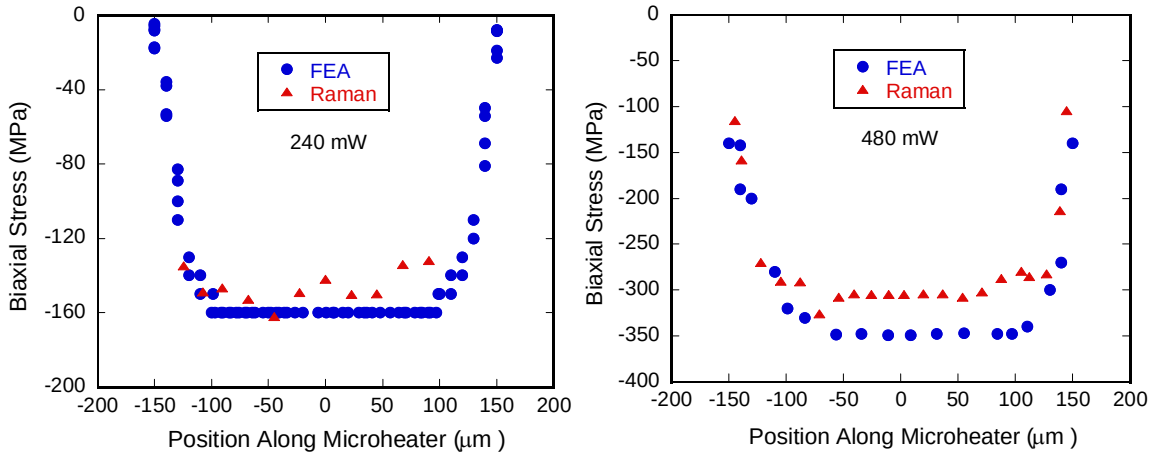

Figure 31. Data comparison of biaxial stress calculated using finite-element analysis (FEA) and Raman spectroscopy for power dissipation levels of 240 mW (left) and 480 mW (right). At the higher power level, the Raman data shows a lower stress level than that calculated by FEA at a level close to the inherent uncertainty (±40 MPa). This may be due to the use of a temperature independent modulus in the analysis.

Figure 31 shows a comparison of the biaxial stresses calculated from both the Raman measurement and the finite-element analysis for a microheater power of 240 mW and 480 mW. The data show fairly good agreement at a power of 240 mW with the stress averaged over the heater of $\sigma_{FEA} = -160$ MPa and $\sigma_{Raman} = -153$ MPa. A similar trend was also seen at a power dissipation level of 480 mW with maximum stress levels of $\sigma_{FEA} = -348$ MPa and $\sigma_{Raman} = -304$ MPa. As seen in the figure, a degree of scatter is apparent in the Raman based stress measurements. Although this scatter could be attributed to variations across the actual device, it is more likely that the variation arises from the inherent uncertainty in the system.

The discrepancy between the Raman measurement and FEA analysis grows to 44 MPa at the higher power dissipation level. It is believed that this is due to the use of a temperature *independent* Young's modulus in the finite element calculation. With a microheater temperature of 520°C, a reduction in the modulus of the polysilicon is

expected resulting in a reduction of stress in the device, a fact not captured by the model. In spite of this finding, both data sets show encouraging results suggesting that it is possible to perform a stress analysis on devices under thermal loading using Raman spectroscopy.

3.4 Measurement of Operational Thermoelastic Stresses in GaN Devices

3.4.1 Experimental Methodology

Using the techniques described in the previous sections, the operational thermoelastic stresses in the AlGaN/GaN HEMT and TLM structures investigated in Chapter 2 are measured and compared against a finite element model of the system in order to judge the efficacy of the proposed methodology. The necessary calibrations were obtained by first examining the E_2^{High} mode of monolithic GaN in the temperature range of 23°C to 550°C in order to specify the stress free constant *A'*. The stress response of this same mode was then analyzed and the magnitude of the biaxial calibration constant *D* found to be -2.91 cm^{-1}/GPa through loading of an epilayer stack in tension from 0-350 MPa (see Figure 17(a)). This measured value of *D* compares well with other reports in the literature thus lending confidence to its use in the subsequent investigation [59, 115]. Furthermore, as the response of the analyzed E_2^{High} phonon mode retains the same linear response irrespective of the nature of the strain, *D* remains valid even in the measurement of compressive stresses despite the tensile nature of the calibration [56, 115]. Its use is also applicable in the measurement of biaxial stresses despite the uniaxial conditions under which the constant is acquired. This finding results from the equivalent phonon response to strains in either crystal direction within the basal plane thereby providing a path between uniaxial calibration and biaxial measurement [115].

The operational stress measurements of the TLM and HEMT were then obtained directly from the Raman acquisitions used to measure temperature in Chapter 2. Pinch-off reference conditions (V_{SD} = 28 V, V_G = -8 V) were utilized in the measurement of the HEMT such that the biaxial thermoelastic stresses could be quantified in a manner that minimized piezoelectric contributions. Using Equation (24), the cumulative averages of the change in peak position and the measured temperature of the more than 75 Raman acquisitions acquired at each data point were then employed to calculate the magnitude of the operational thermoelastic stress in each of the devices.

3.4.2 Finite Element Modeling of Operational Thermoelastic Stress

In order to verify the measurements acquired from Raman spectroscopy, the ANSYS model utilized in Chapter 2 was extended to analyze thermoelastic stress through a one way coupling of the energy and mechanical equations (see Figure 16 for model schematic) [143]. The applied boundary conditions used for the quarter symmetry of the simulation are shown in Figure 32. These conditions, used in conjunction with the solution of the energy equation, allow for the estimation of the thermoelastic stress that forms during operation of both the TLM and HEMT. To facilitate this estimation, interfaces are assumed to be in perfect contact between material layers with any softening being of negligible magnitude. Like in the thermal simulation, the AlGaN layer is not modeled as it contributes little to the mechanical response due to its extreme thinness. Once again, solutions were checked against multiple meshes in order to ensure proper convergence. Convergence was defined to occur when the maximum stress in the device deviated by less than 1% between meshes (see Figure 16 for refined mesh).

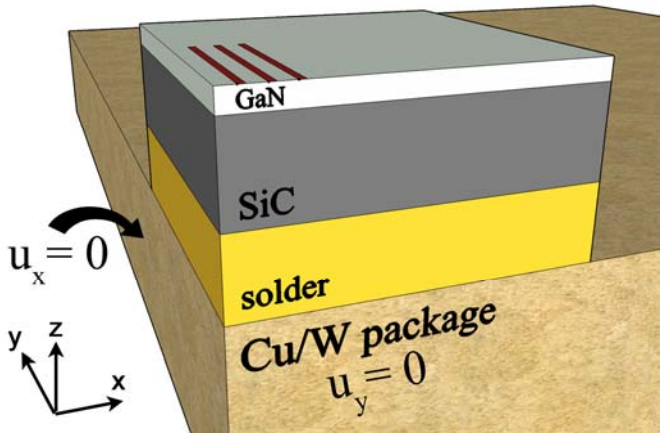

Figure 32. Geometry and mechanical boundary conditions utilized in the finite element model of the AlGaN/GaN HEMT. These same conditions also exist on the corresponding opposite faces of the device such that the model accurately represents the complete fixturing of the device applied during testing. Analogous conditions are applied on the TLM as well**.**

In order to model a complex system such as the HEMT or TLM studied here, accurate material properties must be determined. There exists a large body of work dedicated to determining material properties used in the construction of electronic devices. Consequently, the mechanical properties of the macroscopic material layers of the devices (i.e. substrate, package materials, and solder layer) can be determined with relative confidence due to the wide range of experimental procedures available and their uniform crystalline quality. Thin films, specifically the GaN layer, are much more difficult to test, however, due to their small dimensions and the variability intrinsic in their processing. These difficulties result in a wide range of values for the elastic modulus, thermal expansion coefficient, and Poisson ratio [144]. Care must be taken to incorporate material properties from the literature that are representative of the actual device since direct acquisition of these material properties from the studied devices is beyond the scope of this inquiry.

In light of these concerns, material properties were chosen from the literature in a manner that maximized similarities between the processing, geometry, and film quality of the tested films and those used to construct the TLM and HEMTs considered here. These properties are summarized in Table 4. As seen from the table, an isotropic linear elastic assumption was used for all materials. While anisotropic stiffness matrix elements are available in the literature, large discrepancies continue to exist between the reported individual matrix elements [144]. On the other hand, the effective isotropic modulus calculated using these elements and the Poisson ratio shows much less variation between the published values. Hence, while not ideal, the assumption of an isotropic effective modulus is incorporated as it allows for an overall reduction in the number of unknowns present in the simulation.

Table 4. Mechanical properties incorporated in the 3-D finite element model.

Material	Property	Value	Reference
GaN	α_c (1/K)	3.17e-6	[145]
	α_a (1/K)	5.59e-6	[145]
	ν	0.183	[146]
	E (GPa)	388	[147]
SiC	α_c (1/K)	4.7x10-6	[148]
	α_a (1/K)	4.30×10^{-6}	[148]
	ν	0.175	[149]
	E (GPa)	480	[149]
Solder	α (1/K)	2.0x10-5	[149]
	ν	0.4	[149]
	E (GPa)	56	[149]
Cu/W Package	α (1/K)	6.14×10^{-6}	
	ν	0.289	
	E (GPa)	357	

In order to compare the predicted values of stress from the model with those obtained from the Raman experiment, an averaging technique like that employed in the thermal simulation was utilized. Since GaN is semi-transparent to the 488 nm light used in the experiments, information is obtained throughout the entire material volume and as such an average of the stress through the layer is measured. To compensate for this fact, the model was averaged through the GaN thickness in order to facilitate comparison between computation and experimentation. Although this step was carried out to provide a "one to one" comparison of experiment and simulation, it is of note that throughout the GaN layer the simulated stress was found to remain nearly constant.

Additionally, the simulated stress was found to be overwhelmingly biaxial in nature. This is particularly salient as the calibration constant, *D,* utilized in Equation (24) is derived from the biaxial response of a crystal. As such, its use is only warranted in this particular loading condition. Consequently, the verification of biaxial stress from the simulated results validates the use of this calibration constant in the measurements.

3.4.3 Comparison of Raman and Finite Element Derived Thermoelastic Stress

Thermoelastic stress measurements of the GaN TLM and HEMT structures are complicated over silicon based devices due to several factors. First, GaN is a piezoelectric active material and, hence with the application of an electric field, the material will strain due to this effect as well as those of the thermoelastic variety. While piezoelectric response has been shown to be removable within the uncertainty of the thermal measurements, it is unclear to what extent the remnant that likely remains affects the subsequent stress measurement. This fact is central to the capability of the technique as small errors in the measurement of temperature induce sizable errors in the

quantification of stress. Secondly, unlike silicon, the properties of gallium nitride, both with respect to their Raman response and basic mechanical properties, continue to have wide scatter in the literature, thus inducing difficulties in the precise comparison of the experimental and computational results [56, 144, 150].

With these complications in mind, the resultant measurements of the biaxial thermoelastic stress are shown in Figure 33 for both the TLM and HEMT devices. The experimental values correlate reasonably well with the predictions of the model when the host of uncertainties surrounding the measurement is considered. The quantitative values of the uncertainty in the experiment were calculated using Equation (26) with the scatter in the measured peak position and temperature obtained from the 95% confidence intervals of the more than 70 Raman acquisitions taken at every point. Additionally, uncertainty in the acquired stress values was further reduced through utilization of operational temperatures acquired from the lines of best fit to the measured values (i.e., the lines of Figure 20 and Figure 22) using an analogous procedure to that described in

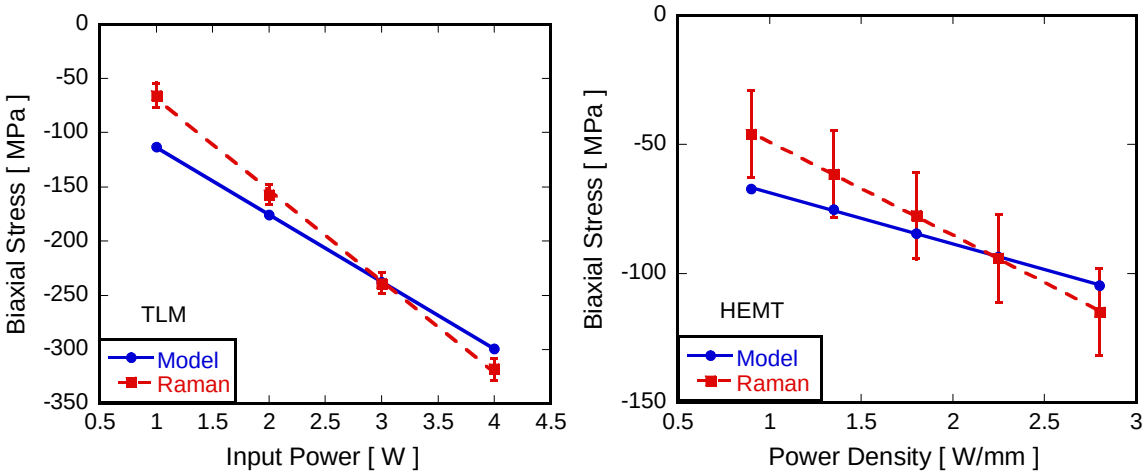

Figure 33. Comparison of thermoelastic biaxial stress obtained through Raman spectroscopy and finite element analysis for a GaN based TLM (left) and HEMT (right).

Section 3.3.5.

Particularly interesting is the magnitude of the evolving thermoelastic stress in the transistor device, which reaches only ~1% of the yield strength of GaN even at high power [151]. Due to this relatively small magnitude, questions subsequently arise as to whether it is this thermoelastic stress component or rather the piezoelectric and residual contributions that are the dominant components of the total load driving the relaxation induced degradation [12, 36, 152]. As this technique shows promise in the determination of operational stress, this question can be approached through quantification and comparison of each stress component and the resultant stress state that evolves during device operation.

3.5 Determination of Dominant Stress Components in AlGaN/GaN Based HEMTS

3.5.1 Experimental Methodology

In order to assess the dominant component of the load present in an AlGaN/GaN HEMT, residual, thermoelastic, and inverse piezoelectric stresses are quantified for a series of devices grown atop both silicon (Si) and silicon carbide (SiC) substrates. Each of these substrates has been suggested for widespread implementation into GaN based devices and while their merits have been investigated from a thermal perspective, comparison of their mechanical capabilities is still lacking [79]. To provide this comparison, 16 separate GaN on SiC AlGaN/GaN devices similar to that analyzed in the previous section, and described in Section 2.2, were measured to obtain the values of residual, thermoelastic, and inverse piezoelectric stresses. Subsequently, a set of 30 GaN on Si AlGaN/GaN HEMTs were investigated in a synonymous procedure. Measurements of the residual and inverse piezoelectric stress were obtained at ambient conditions while

thermoelastic stresses were obtained during operation at a package temperature of 85°C in an identical fashion to the previously described measurements. In addition, although the device architectures between the two sets are not congruent, care was taken to ensure that inputs (i.e., power, bias) were equal such that comparisons between the series remained pertinent. Finally, the great number of devices that were analyzed, 46 in total, allows for confidence that the comparisons between the data sets are significant and not the result of a peculiarity in an individual device. In this manner, it is possible to determine with certainty the dominant loading contribution in the device.

3.5.2 Determination of Residual Stress

Residual stress is measured by comparing the Raman signal of the specimen of interest as compared to a stress free sample of the same material. The difference in the peak positions between these two measurements may then be utilized to calculate stress from Equation (22). Use of Equation (22) with the obtained constant *D*, infers that the residual stress is biaxial in nature. This is likely owing to the thin film architecture of the transistor, and as such its use is warranted here. To then calculate the magnitude of this load, the stress free peak position of GaN was first found from a free standing bulk sample and calculated to 567.198 +/- 0.004 cm^{-1} for the utilized E_2^{High} mode. This value is within the range of values reported in the literature and allows for the determination of the residual stress to take place apart from spectrometer specific biasing [150, 153]. To obtain these stresses, each of the analyzed devices was measured at ambient conditions under no bias both before and after operational testing with no significant changes taking place for either material system.

With respect to the devices built atop a SiC substrate, the resulting ambient peak position was found to be 566.96 +/-.05 cm^{-1}. This value, when used in conjunction with the position of the stress free sample and Equation (22), corresponds to a biaxial residual tensile stress in the sample of 87 +/- 16 MPa. In a similar fashion, the residual peak position of the silicon substrate series was found to be located 565.74 +/- .05 cm^{-1} leading to a much larger biaxial residual stress in these devices of 499 +/- 16 MPa. This larger magnitude arises from the great difference in the coefficients of thermal expansion that exist between the silicon and GaN (2.8-4.6 ppm/K difference). In comparison, the stress is greatly reduced in the devices having a SiC substrate as the discrepancy between the materials' coefficients of thermal expansion are much smaller (0.28-2.08 ppm/K difference) [154]. Regardless, each system is initially in a state of residual tension, which will act to increase the initial carrier concentration of the 2DEG (see Figure 3).

3.5.3 Determination of Piezoelectric Induced Stresses

Sarua *et al.* [102] assert that the level of stress induced from the piezoelectric stress remains the same regardless of the bias on the gate, and hence, irrespective of whether current is flowing through the transistor. Therefore, the stress arising from this effect can be obtained by comparing the peak position of the device under both ambient and pinched off conditions whereupon Equation (22) can be utilized once again as the stress may be shown to be biaxial in nature. Practically, this took place by analyzing each series of devices both before and after powered operation. At each time, the devices were interrogated at ambient conditions under zero bias (V_{SD} = 0 V, V_G = 0 V) and at pinch-off conditions (V_{SD} = 28 V, V_G = -8 V) with the peak positions compared and subsequently

transformed to stress. For the devices having a SiC substrate, the piezoelectric induced biaxial compressive stress was found to be -50 +/- 1 MPa.

Unlike what was seen in the devices with a SiC substrate, the transistors having a silicon substrate exhibited highly variable behavior before and after powered operation. Initially, there was very little change in the Raman signal with bias indicating that the evolution of stress from the inverse piezoelectric effect was minimal. Contrarily, after testing, changes in the signal were observed that corresponded to an induced biaxial compressive stress of -75 +/- 5 MPa. The cause for the dynamic nature of this stress evolution is unclear but does indicate the possibility of relaxation somewhere in the device architecture. Notice, however, that unlike the residual stress, the values of the piezoelectric induced stresses between the Si and SiC samples are comparable.

To verify that the stresses estimated using this method are plausible, Sarua *et al* [102]. develop an uncoupled electromechanical analytical model of the system that links the strain, and in conjunction the change in peak position, to the electrical field. Generally, this model derives from the thermodynamic relation linking the strain and the electric field at constant temperature via:

$$\varepsilon_{ij} = S_{ijkl}\sigma_{kl} + d_{kij}E_k \tag{29}$$

where ε_{ij} is the strain, E_k the electric field, σ_{kl} the stress, and d_{kij} along with S_{ijkl} are elements of the piezoelectric modulus and elastic compliance tensor, respectively [123]. For the specific case of a AlGaN/GaN HEMT, this general relation may be simplified by assuming a free surface and rigid coupling of the GaN to the underlying substrate allowing for a prediction of the peak position change to a given electric field :

$$\varepsilon_{33} = \frac{\Delta\omega}{\beta} = \left(d_{33} - \frac{2S_{13}}{S_{11} + S_{12}} d_{31} \right) E_{33} \tag{30}$$

where ε_{33} and E_{33} are the strain and the electric field in the through thickness (z) direction, β is the phonon deformation potential linking a change in the peak position to strain, while the numbered subscripts correspond to matrix notation of a tensor [123]. Utilizing this relation with a modeled electric field, comparisons can be made between the measured and predicted strain values. Incorporating this procedure, which implicitly assumes a constant stress and electric field through the thickness of the transparent GaN layer, Sarua *et al.* [102] report similarities in the qualitative trends of the measured and modeled responses. However, despite this qualitative agreement, the magnitude of the experimentally obtained stress is reported to be ten times greater than that of the computation.

Using this same methodology on the devices of this study, a similar drastic over prediction was found when comparing the strains in the SiC series with a model of the electromagnetic response developed using Sentaurus by Dr. Eric Heller of the Air Force Research Laboratory. Comparable values to within 24% between experiment and computation were found for the strain, however, if the maximum, rather than average, electric field was utilized in Equation (30). This close correlation, especially if the great uncertainty in reported piezoelectric modulus of GaN is considered, indicates that although the total volume of the material is indeed probed by the Raman response, the material itself strains, like many thin films, according to the most intense load and hence the magnitude of the greatest electric field. Furthermore, the correlation also lends confidence that our estimation of the piezoelectric induced stress is at least correct to

within an order of magnitude. Consequently, this measured response allows for the load to be compared with the other calculated components of the stress.

3.5.3.1 Confocal Investigation of Through Thickness Piezoelectric Stress Variations

To judge the suitability of assuming a uniform stress profile within the GaN layer according to the maximum electric field, a confocal examination of the piezoelectric induced stress evolution in a HEMT having a SiC substrate was performed. In a confocal arrangement, the depth of field is substantially limited allowing for variations to be observed through the thickness of the GaN layer in spite of its transparency. Quantitatively, the employed confocal arrangement reduced the depth of field to ~ 1.6 μm, which permits for comparison of the piezoelectric stress at discrete depths within the active layer [50]. Specifically, the experiment was implemented through acquisition of the Raman signal at 0.5 μm increments from the surface of the transistor until a depth of 3.5 μm at both ambient and pinch-off (V_{DS}= 28 V, V_G= -8 V) conditions. The differences in the peak positions at each depth level are then compared to judge if the piezoelectric induced stress varies within the film. Notice that as the thickness of the GaN layer is ~2 μm, Raman acquisitions are acquired while the focal plane is actually within the underlying SiC substrate. This occurs as the depth of field extends for ~ 1.6 μm above and below the focal plane and as such relevant information is available for depths of up to the examined 3.5 μm (i.e., 1.6 μm into the SiC).

Simulated electric field profiles of AlGaN/GaN HEMTs predict a profile that exponentially decreases with distance away from the surface of the GaN layer [102]. It is expected that the induced piezoelectric stress should then follow a similar exponential decrease. The magnitude of this elastic gradient is quite substantial inducing a predicted

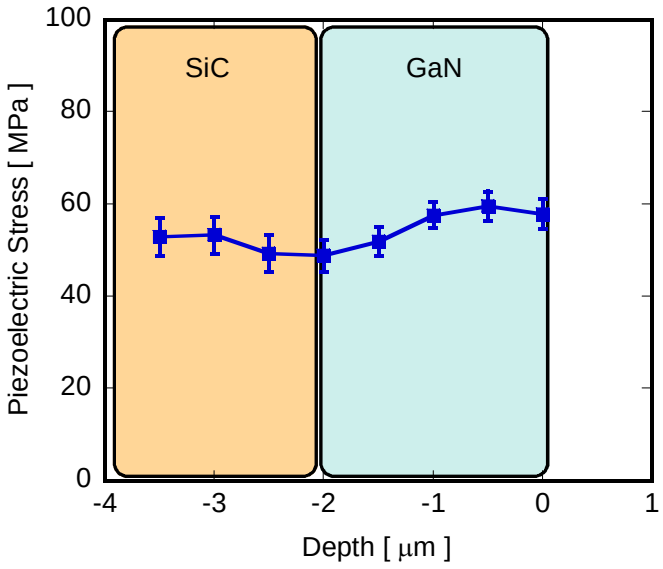

Figure 34. Variation of biaxial compressive stress due to the inverse piezoelectric effect through the thickness of the GaN layer. The induced stress remains similar through the entirety of the layer indicating that the response remains nearly constant despite the change in electric field.

change in the stress of nearly an order of magnitude inside the GaN. Consequently, even if the acquired Raman signal is unable to resolve the finer aspects of this gradient owing to the depth of field being only marginally smaller than the layer itself, the large magnitude of the variation may be detected if, in fact, it is present. However, examination of Figure 34 indicates that the piezoelectric induced stress remains nearly constant throughout the entire thickness. Furthermore, the magnitude of this response, similar to that reported in the previous section, indicates that the stress seems to correspond to the maximum electric field rather than the average. These results then provide experimental evidence that the piezoelectric stress profile in the GaN layer indeed remains fairly uniform.

3.5.4 Determination of Operational Thermoelastic Stress

Each of the 46 examined AlGaN/GaN HEMTs was tested at a backside package temperature of 85°C with a drain-source bias set to 28V. Operational stresses were examined through appropriate adjustment of the gate such that five different power densities were examined between 0.9 and 2.8 W/mm. The cumulative values and distributions of the temperature and peak position from all devices were then used in concert with Equations (24) and (26) to estimate the operational biaxial thermoelastic stress and uncertainty, respectively.

Shown in Figure 35 are the resultant measurements of the biaxial stress in each of the two types of devices. Once again, the load in the silicon series of devices is much greater than that of the devices grown on SiC. This result stems, like that seen with respect to the residual load, from the much greater coefficient of thermal expansion mismatch between

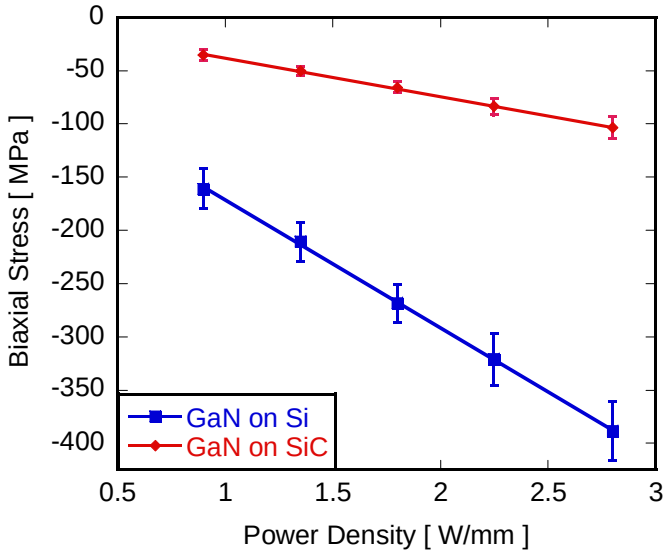

Figure 35. Biaxial thermoelastic stress calculated during operation of an AlGaN/GaN HEMT grown atop a silicon and SiC substrate.

GaN and Si than that of a GaN/SiC system. In addition, as the thermal conductivity of SiC is much greater than that of Si, the effect of this mismatch becomes exacerbated as the temperature in the silicon devices reaches in excess of twice that of the SiC series. As a consequence of these factors, the resultant biaxial thermoelastic stress is nearly four times greater in the silicon devices for the same power load.

3.5.5 Comparison of Different Stress Loads in AlGaN/GaN HEMTS

The different types of loading are directly compared in Figure 36 for both the SiC and Si series of devices. In each case, the biaxial stress induced from the inverse piezoelectric effect is relatively small in comparison to the maximum thermoelastic stress that evolves during operation and those residual loads already present from the fabrication of the device itself. Furthermore, assuming the material is linear elastic for the conditions studied here, an assumption which is likely valid for the GaN but not the

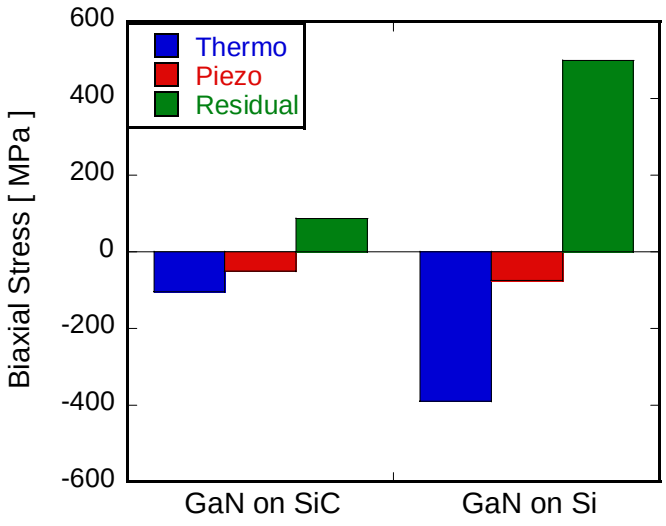

Figure 36. Comparison of the residual, inverse piezoelectric and thermoelastic loading (at 2.8 W/mm and a package temperature of 85°C) for AlGaN/GaN HEMTs grown on SiC and Si. Note that as each individual component induces a biaxial stress, the resultant load will be biaxial as well.

AlGaN layer, the resultant stress state of the device during operation may be obtained through superposition of the individual biaxial stress components at each power level. Surprisingly, although large levels of compressive stress develop during operation of the Si devices, the resultant biaxial stress state is actually tensile and achieves a magnitude on par with that of the SiC devices at the highest levels of input power (see Figure 37). Likewise, the residual stress acts to mitigate the evolving compressive thermoelastic stress in the SiC devices. In contrast to the Si series, however, the resultant state in the SiC/GaN system remains compressive throughout the entire range of powers investigated. It is of note that these conclusions are dependent upon the backside package temperature (i.e., 85°C) as the absolute magnitude of the thermoelastic, and as such the resultant load, is dependent upon this value. Consequently, at higher package temperatures when the thermoelastic stress contribution will be larger, the silicon devices should be expected to operate in a compressive regime at lower power densities.

The nature of the resultant stress is of great consequence as the concentration of carriers in the 2DEG increases while in tension but decreases under a compressive load (see Figure 3). Consequently, the resultant load actually serves to increase the number of carriers and increase, assuming no relaxation in the AlGaN layer, the capability of the device built on silicon. Contrarily, the nature of the load in the SiC series serves to decrease the capability of the device. As the sign of this resultant load is determined primarily by the residual stress, future studies may investigate the manner to increase this tensile value without relaxation occurring in the AlGaN layer, thereby increasing the number of carriers with the concomitant increase in device performance.

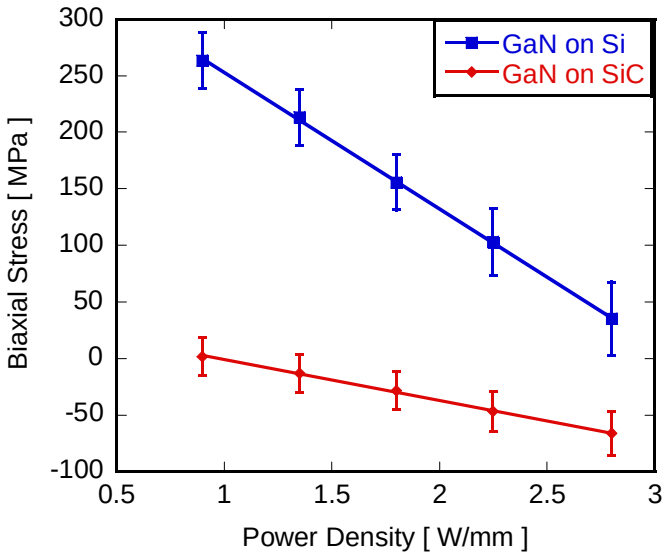

Figure 37. Resultant biaxial stress during operation at a package temperature of 85°C of an AlGaN/GaN HEMT grown on top of Si and SiC. Although compressive stresses increase for each device with input power, the large residual stress of the Si series determines that these devices operate in tension.

3.6 Summary

The magnitude of the stress in an AlGaN/GaN HEMT is a primary determinant of the concentration of carriers and the overall performance of the device. As a consequence, measurement of this parameter is central to the further refinement and improvement of this device class. In response, this study has developed a method to measure the biaxial operational thermoelastic stresses that form during operation of MEMS and microelectronic devices through use of Raman spectroscopy. Through utilization of the Stokes linewidth to measure temperature, the peak position was demonstrated to be capable of accurately measuring the evolving thermoelastic stress in a silicon based MEMS structure and two differing GaN architectures. With the technique verified, GaN HEMTs grown on Si and SiC were examined to investigate the roles of the thermoelastic, inverse piezoelectric, and residual stresses on the overall device load. Through this

investigation, the residual stresses were found to severely mitigate the evolving compressive thermoelastic stress to such an extent that the transistors grown on silicon operated in tension at even high thermal loads. The dominant role of these residual stresses, illuminated through technique developed here, may be leveraged in future design to produce an AlGaN/GaN HEMT of greater performance and reliability.

CHAPTER 4

TEMPERATURE AND DOPING DEPENDENCE OF PHONON LIFETIMES AND DECAY PATHWAYS IN GAN

4.1 Overview and Approach

Conceptual understanding of the temperatures quantitatively estimated in the previous chapters requires understanding of the dominant energy transfer mechanisms at play. In particular, it is necessary to understand the manner in which energy cascades from an accelerated electron into the lattice and away from the active region of the device. In GaN, electrons emit and interact with polar optical phonons as they are accelerated across the transistor channel. From a thermal perspective, this route is problematic as these emitted optical phonon modes have low group velocities causing them to act as a capacitive energy reservoir for the energy emitted by electrons. To dissipate the transferred energy effectively, these optical phonon modes must then decay into acoustic phonon modes that move with higher velocities. At issue is the fact that the time scale for optical phonon emission by electrons is much smaller than the time scale for phonon decay. This leads to a phenomenon known as the hot phonon bottleneck, which induces intense heating in the device channel with an associated reduction in both performance and reliability [155, 156]. While the hot phonon bottleneck is an area of much research, relatively little is known about the actual phonon transformations that give rise to the effect.

The lifetimes, and derivatively the transformations, of zone center (Γ-Point, see Figure 41) optical phonons can be determined experimentally through a number of techniques including steady state and time resolved Raman spectroscopy, as well as

microwave noise measurements [93, 157, 158]. In using steady state Raman spectroscopy, the linewidth, Γ (FWHM), of the Stokes peak can be directly correlated to the lifetime of the measured phonon through the energy-time uncertainty relation (see Equation (8)) [93, 159]. Time resolved Raman spectroscopy, on the other hand, does not rely on this relation but instead deduces the lifetime through examination of the decay in the temporal response of the anti-Stokes Raman signal [160]. In contrast to these optical techniques, the microwave noise procedure relies upon an interaction between the phonon and the free carriers thus limiting its application to only particular modes. This interaction allows for the creation of a simple energy balance, which when used in concert with measurements of the rate at which electrons gain and lose energy, allows for estimation of the phonon lifetime [157, 161].

Regardless of technique employed, measuring the lifetimes of a particular mode at several temperatures allows for prediction of the phonon decay path through use of perturbation theory. Knowledge of the decay pathway, in turn, gives insight into the entire lattice energy cascade and visualization of the energy "flow". Through careful examination of this flow, energy bottlenecks may be identified and future avenues for device improvement through phonon engineering are illuminated. Using standard Raman spectroscopy, previous studies have identified these pathways for 5 different phonon modes in standard bulk samples of GaN having relatively low free carrier concentrations ($n<10^{17}$ cm^{-3}) [96, 162].

In the presence of a high free carrier concentration ($n > 5x10^{17}$ cm^{-3}), however, the LO phonons become strongly coupled with the presence of plasmons forming what is commonly referred to as a longitudinal optical phonon-plasmon (LPP) coupled mode [66,

163]. Tsen *et al.* [158] have used this coupled mode, in turn, to deduce the lifetime of the A_1(LO) phonon showing an inverse relationship between the rate of decay and the free carrier concentration. Due to this dependency, questions arise as to the extent of free carrier interaction throughout the entirety of the energy cascade. In response, this study analyzes decay of 4 phonon modes in a series of GaN samples having carrier concentrations ranging from $3x10^{17}$ to $1.24x10^{18}$ cm^{-3} at temperatures varied from 23-300 °C. By incorporation of this method, the lifetime, decay pathways, and carrier dependencies will be enumerated for each of the modes thus offering insight into relevant the energy transfer mechanisms in GaN based devices.

4.2 Experimental Methodology

A series of gallium nitride wafers were produced through use of a metal organic chemical vapor deposition (MOCVD). Three different wurtzite GaN samples were examined in this study, namely: n-type (nGaN) acquired through Si infiltration, p-type (pGaN) attained utilizing an Mg implantation procedure, and bulk GaN (GaN). Through room temperature analysis of the spectral profiles of the LPP modes, it was found that the free carrier concentration for the n-type, p-type, and bulk GaN samples were: $1.24x10^{18}$, $6.4x10^{17}$, and $3x10^{17}$ cm^{-3}, respectively [150]. Due to the nature of the doping procedures, it must be emphasized that these values correspond to only the free carrier concentration and not necessarily the actual level of doping (e.g., the amount of implanted Mg). In addition, it is of note that the doped regions described thus far rest directly on top of an undoped GaN buffer layer in order to assure the highest quality lattice structures. Further details regarding both the growth and initial characterization of the GaN samples studied here can be found in references [164-166].

Phonon lifetime measurements were carried out using a Renishaw InVia Raman system. The system utilized a 488 nm Ar^+ laser in the 180° backscattering mode through a 50X objective. In this region of the spectrum, GaN is transparent, and as such, the probing radiation interacts with both the doped as well as the undoped GaN buffer layer. The acquired signals will thus have contributions stemming from each region. However, as this buffer layer is consistent between each of the differently doped samples, qualitative comparisons between the specimens remain valid. With this understanding, samples were measured at typical device operating temperatures ranging from 23-300 °C using a Linkam TS-1200 heated stage along both the *c* and *a* axis (see Appendix for necessity of measuring along both axes) in order to capture 4 of the Raman active modes (A_1(LO), A_1(TO), E_1(LO), and E_2^{High}). In the backscattering arrangement, the E_1(LO) mode is forbidden and as such the actual measured values are that of quasi-LO or Q(LO) mode. This Q(LO) mode, however, has been used to directly estimate the lifetime of the E_1(LO) mode in the work of Song *et al.* [96] and will likewise be used here.

Of the 4 modes investigated, the E_2^{High} mode is the only non-polar phonon mode and will be used as a comparison to the behavior of the other polar optical phonon modes. This same mode is also used as a built in temperature sensor to verify sample temperature during the experiments through basic Raman thermometry techniques [103]. For each temperature and phonon mode, at least 20 acquisitions of the Raman signal were acquired resulting in uncertainties that were no more than +/- 3.7 % and most often less than +/- 1% of the measured lifetime value.

4.3 Results

4.3.1 Temperature Dependence of the Phonon Lifetimes

The measured Raman linewidths are a convolution of effects stemming both from the spectrometer-induced broadening and the actual Lorentzian vibrational distribution of the phonons in the crystal lattice. It is typically assumed that the spectrometer imposes a Gaussian response on the signal from the crystal lattice, which is itself Lorentzian in character. Thus, the Raman spectrum is fitted using the mathematical convolution of these functions known as the Voigt profile [167]. Consequently, the "as acquired" measured linewidth cannot be used to obtain the phonon lifetime directly as it has effects evolving from both the crystal and the response function of the spectrometer.

To obtain the actual crystal lattice linewidth, the Voigt profile is deconvoluted using Posener's Tables with knowledge of the Gaussian response function of the spectrometer [138, 168] . The Gaussian response function can be determined through calibration with plasma lines of an extended neon source at varying slit widths. The lifetime is subsequently calculated using the energy-time uncertainty relation with the true linewidth described here again for clarity in a restatement of Equation (8) as [169]:

$$\tau = \frac{\hbar}{\Gamma} \tag{31}$$

where τ is the lifetime in ps, $\hbar$ is the modified Planck constant (5.3 cm^{-1} ps), and Γ is the crystal linewidth.

Using this deconvolution procedure, phonon lifetimes were examined for the 4 phonon modes in each of the 3 samples investigated. Quantitatively, it was found that the room temperature lifetimes of the E_2^{High}, $A_1(LO)$, $A_1(TO)$, and $E_1(LO)$ modes were 2.56,

0.86, 0.63, and 0.66 ps, respectively for the bulk GaN sample. These lifetimes correlate well with the recent work of Song *et al.* [96] who report similar values of 2.5, 0.75, 0.5, and 0.58 ps for these same respective modes for bulk GaN at room temperature.

Figure 38 shows the temperature dependence of the lifetimes for each of the five phonon modes for the bulk, p-doped, and n-doped GaN samples. From the figure, it is seen that for all samples an increase in temperature is accompanied by an associated decrease in phonon lifetime. This decrease occurs as the rate of phonon-phonon scattering increases with temperature due to the associated increase in the phonon thermal occupancy and hence their interaction. Yet despite this qualitative uniformity, there are significant quantitative differences in lifetime values for many of the modes. This is exemplified for the A_1(LO) mode where at room temperature the lifetime is seen to decrease from 0.86 ps with a carrier concentration of $3.1x10^{17}\,cm^{-3}$ to 0.68 ps at a concentration of $1.24x10^{18}\,cm^{-3}$. The underlying cause for this discrepancy, whether it be changes in the lattice due to the doping procedure or actual phonon-carrier interaction, cannot be enumerated based solely upon the differences in these lifetime values. Rather, it is necessary to compare the decay processes for each of the different samples in order

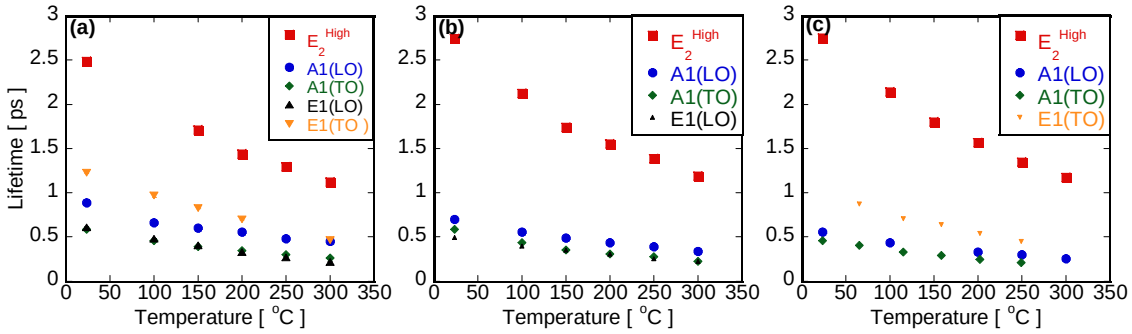

Figure 38. Phonon lifetime vs. temperature for each mode examined in (a) bulk GaN (b) p-type GaN (c) n-type GaN. Analysis of the temperature dependence of these lifetimes can be used to identify the decay pathways of the phonon modes.

to identify the underlying causes for the variation in the lifetimes. Consequently, the subsequent sections will examine the decay pathways for each mode in order to determine the lifetime's dependency on free carrier concentration.

4.3.2 E_2^{High} Phonon Decay Channels and Carrier Dependency

Using the temperature dependent phonon lifetimes seen in Figure 38, it is possible to determine the phonon decay pathways in the Brillouin zone. Assuming that each optical phonon dissipates into two phonons in a so called 3 phonon process, Klemens obtained the following relation for the linewidth of a crystal based upon perturbation theory:

$$\Gamma_3(\mathrm{T}) = \Gamma_D + \Gamma_o\left(1 + \sum_{i=1}^{2} \frac{1}{\mathrm{e}^{(x_i)} - 1}\right) \tag{32}$$

where Γ_o and Γ_D are fitting parameters that represent the linewidth at 0K, $x_i = \frac{\hbar\omega_t}{k_B T}$ where k_B is the Boltzmann's constant, T is the temperature in Kelvin, $\hbar$ is, again, modified Planck's constant only this time in standard units of Joule-seconds, and ω_i is the frequency of the resulting phonon after the scattering process [170]. Due to conservation of energy, the following relation must be satisfied: $\omega_0 = \omega_1 + \omega_2$. Using Equation (32), the temperature dependent linewidths were fitted for the E_2^{High} mode assuming a symmetric decay process ($\omega_o/2 = \omega_1 = \omega_2 = 284$ cm^{-1}) and then transformed to a lifetime value per Equation (31). As seen in Figure 39 for the bulk GaN sample, it was found that the resulting curve did not correlate well with the measured lifetime values. Consequently, it is necessary to account for more complex and possibly asymmetric decay mechanisms.

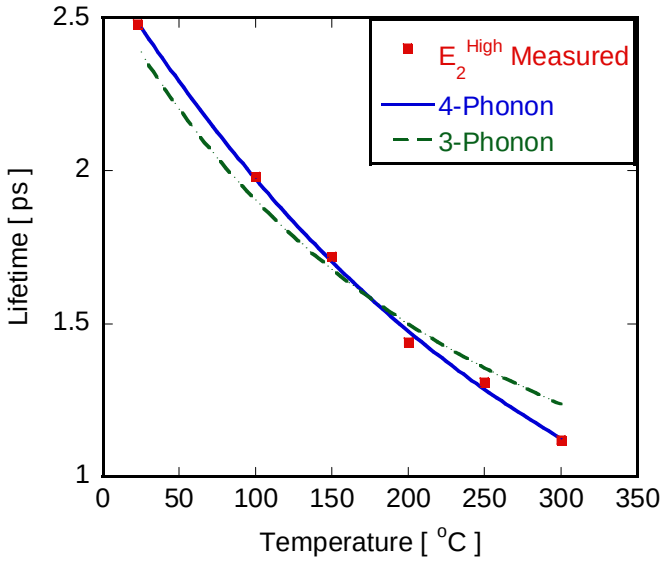

Figure 39. Measured E_2^{High} mode for bulk GaN fitted accounting for only 3-phonon processes (dashed line) and using both 3 and 4-phonon processes (solid line). It can be seen that 4-phonon processes are quite relevant at the temperatures examined here.

Balkanski *et al.* [73] account for these complex decay mechanisms through modification of Klemens' original model considering both 3 and 4 phonon processes. In a 4 phonon process, decay of the phonon is assumed to occur into 3 separate phonons and revises Equation (32) into the form shown below:

$$\Gamma_4(\mathrm{T}) = \Gamma_3(T) + \Gamma_1\left(1 + \sum_{i=3}^{5}\frac{1}{\mathrm{e}^{(x_i)}-1} + \sum_{i=3}^{5}\frac{1}{\left(\mathrm{e}^{(x_i)}-1\right)^2}\right) \tag{33}$$

where Γ_1 is an additional fitting parameter representing a portion of the linewidth at 0K. Incorporating this fitting procedure and assuming equivalent decay for the 4-phonon process ($\omega_3 = \omega_4 = \omega_5 = \omega_0/3$). Equation (33) was found to have excellent correlation with the data for the E_2^{High} mode as seen in Figure 39. As this same fitting model was also capable of predicting each of the differently doped samples' responses (see Figure 40), it

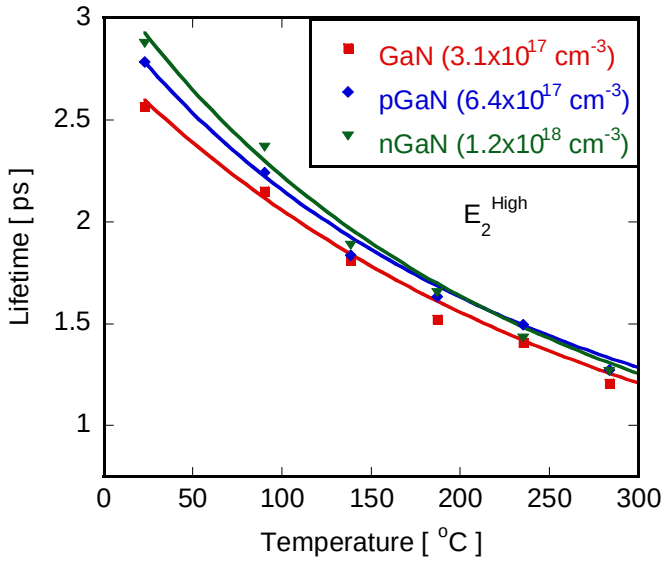

Figure 40. Phonon lifetime versus temperature for the E_2^{High} mode of bulk, p-type, and n-type GaN where the symbols are the measured values while the lines represent the fitting obtained using Equation (33). Notice that at higher temperatures the lifetimes converge indicating the dominance of phonon-phonon scattering and a lack of phonon-carrier interaction.

can be reasoned that the phonon decomposition mechanisms are identical despite the changes in free carrier concentration.

The actual path of decomposition may be identified through examination of the Brillouin zone of GaN as in any scattering event energy must be conserved while phonon momentum must similarly be preserved within a reciprocal lattice vector. To examine the phonon momentum (energy was conserved as part of the fitting procedure), it must be noted that due to the wavevector of the incident light, it is only those phonons near the Gamma point that are measured during the acquisition of a 1st order Raman spectrum [150]. Consequently, in the assumption of a symmetric 3-Phonon decay process, conservation of the phonon momentum stipulates that the resulting phonons must have wavevectors opposite to one another with respect to the Gamma point of the Brillouin

zone. This fact remains valid even after an Umklapp process, as with the addition or subtraction of a reciprocal lattice vector, the resulting phonon has an identical wavevector albeit in an adjacent zone.

In a similar manner, momentum conservation of the phonons necessitates that in a 4-phonon process, the sum of the 3 resulting phonon wavevectors must equal zero. As there is a relation between energy (frequency) and phonon momentum (wavevector) via the lattice dispersion curve, only certain transformations will be allowed. Thus by examining the scattering processes with respect to the dispersion curve, one can easily ensure the viability of a scattering mechanism while simultaneously tracing the decay pathway of the phonon.

Previously, it was shown that suitable fitting of the experimental lifetime data for the E_2^{High} mode was obtained by assuming a symmetric decay process where the phonon

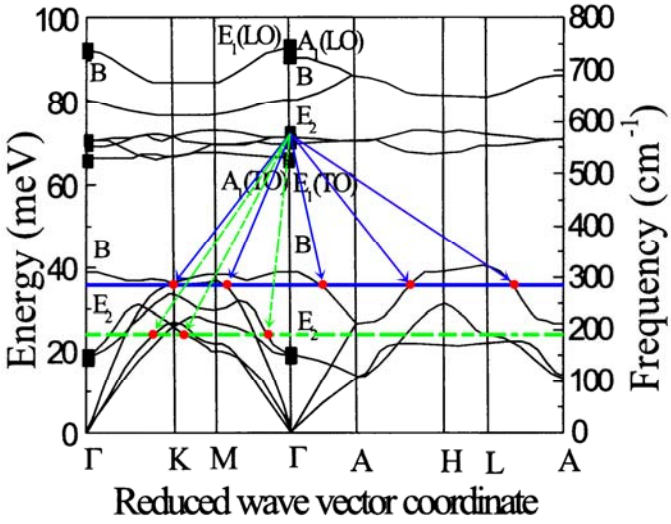

Figure 41. Dispersion curve of wurtzite GaN as reported by Siegle *et al.* [149]. The decay of the E_2^{High} phonon is shown to occur via a combination of symmetric 3 phonon and 4-phonon decay. Notice the points (dots) on the curve satisfy the momentum criterion indicating an allowed scattering event.

decays into 2 phonons of energy $\omega_o/2$ and a 4 phonon process by which 3 phonons of energy $\omega_o/3$ result. If the dispersion curve, as seen in Figure 41, is then examined at these resulting energies (the solid 284 cm^{-1} and dashed 189 cm^{-1} lines), decay can take place only if points on the dispersion curve are present that also satisfy the momentum criterion. For example, the momentum criterion is satisfied for symmetric decay at points on the dispersion that intersect the constant $\omega_o/2$ energy line as 2 resulting phonons of opposite wavevector at this intersection will result. Similarly, viability of the 4 phonon process can be ensured if intersection between the $\omega_o/3$ energy line and the dispersion curve occurs at a set of 3 locations such that the resulting wavevectors sum to 0. In Figure 41, the solid and dashed arrows identify such locations along the constant $\omega_o/2$ and $\omega_o/3$ energy lines, which satisfy these conditions for both the 3 and 4-phonon processes respectively. As a consequence, the hypothesized decay model is then validated while simultaneously illustrating possible avenues for the decomposition of the of the E_2^{High} mode. Note that as the dispersion only gives information with respect to the directions of high symmetry and not the entire Brillouin zone, additional scattering pathways will no doubt be available. Thus, Figure 41 gives possible, rather than definitive, pathways. Yet even with knowledge of these possible decay routes, a preliminary picture of the energy cascade in GaN begins to form and the dominant cause of scattering can be identified through comparison of the lifetimes between differently doped samples.

The lifetime of a phonon is limited by interactions with boundaries, defects, free carriers, and other phonons. If these interactions take place independent of one another, an assumption that may not remain strictly valid at high free carrier concentrations but is

often employed to analyze GaN carrier transport nonetheless, Matthiessen's rule allows for the scattering as a whole to be examined through analysis of the individual scattering sources themselves [171-173]. During the Raman measurement, a large set of individual scattering events is probed and the resulting lifetime is an average composed of contributions from each of these scattering sources. This average is weighted toward those events occurring most often and, hence, the scattering source with the greatest strength. In general, the combined strength of a scattering source is population dependent, depending on defect density, phonon population, carrier population, etc. Differences in the measured lifetimes then arise due to disparities in the populations of the scattering sources themselves. Thus, by understanding the temperature dependent populations of the scattering sources, it becomes possible to identify the dominant scattering mechanism in each of the differently doped samples.

As GaN has a stable crystal arrangement, the microstructure may be assumed to remain static during the measurements and hence so too the number of defects. Thus, with an increase in temperature, the number of scattering events arising from the presence of defects will remain largely constant. In contrast, the number of both phonon-phonon and phonon-carrier scattering events will change with temperature as the number of these species available for interaction varies due to their temperature dependent Bose-Einstein and Fermi-Dirac distributions, respectively. Therefore with an increase in temperature, and a concomitant increase in the number of phonons and free carriers, the measured lifetime will become ever more weighted to the effects of these species rather than those of the microstructure. Consequently, comparison of the phonon lifetimes at higher

temperatures between each of the doped samples allows for the effects of phonon and carrier scattering to be isolated from those stemming from the microstructure.

Separation of the carrier and phonon effects may then occur by recognizing that each of the differently doped samples remains in a GaN wurtzite crystal arrangement and as such displays a similar dispersion. While the dispersion may be slightly modified by the dopants alteration of the crystal stiffness, this effect is expected to be comparatively small, and as such the level of phonon-phonon scattering will be practically equivalent between the specimens. In contrast, the number of carriers, and hence the level of carrier scattering, will be different between samples owing to the variance in doping concentration. As the value of the lifetime is intrinsically tied to the population of the scatterers, similarities in the measured lifetimes may evolve only through a dominant source common to all samples. Only phonon-phonon scattering is similar in each of the specimens, and thus a convergence in the value of the lifetimes indicates a dominance in this form of scattering and an associated independence to carrier scattering. Using this deductive procedure, similarities in the lattice scattering are seen in Figure 40 where the lifetimes of the E_2^{High} mode converge to a common value of ~1.25 ps near 300°C indicating a prevalence of phonon-phonon scattering and, as expected, an independence to carrier interaction. At lower temperatures, meanwhile, the lifetime varies widely between samples as microstructural differences arising from the doping procedure become an ever more dominant scattering source.

The independence of this mode to carrier interaction is particularly relevant with respect to the measurements of temperature and stress described in the previous chapters. It is imperative, in order for these measurements to be accurate, that the utilized Raman

mode be independent to any factor outside that parameter being assessed. Consequently, the independence of the E_2^{High} mode to carrier interactions further validates the methodology incorporated in the measurement of temperature and stress as its signal remains unaltered from the carriers that drive the operation of the device.

4.3.3 A_1(LO) and E_1(LO) Phonon Decay Channels and Carrier Dependency

At high free carrier concentration, coupling occurs between the LO modes and plasmons creating a longitudinal optical phonon-plasmon coupled mode (LPP). This LPP mode has a spectral shape dependent upon the frequency of the free carriers and has been used as a complement to Hall measurements in the determination of free carrier concentration [163, 174]. Recently Tsen *et al.* [158] used this LPP mode to measure the lifetime of the A_1(LO) phonon assuming equivalent durations for both the coupled and vibrational modes. Using this same assumption, it is possible to examine the decomposition processes of the A_1(LO) and E_1(LO) phonons. In order to determine these processes, the modified Klemens decay model using the Ridley decomposition channel, presented in Equation (33), was utilized to simulate the temperature dependent lifetime response for both the A_1(LO) and E_1(LO) modes.

Unlike the E_2^{High} mode, high energy A_1(LO) and E_1(LO) lifetimes can not be modeled using a symmetric phonon decay process since $\omega_o/2$ occurs in a large phonon bandgap of the dispersion curve. For the A_1(LO) mode, it has been both postulated theoretically by Ridley [175] and verified experimentally by Tsen *et al.* [176], that an asymmetric 3-phonon process is the dominant decay pathway whereby the LO phonon decomposes into a TO and longitudinal acoustic (LA) mode. Assuming this asymmetric decomposition for the 3-phonon process in Equation (33), while making no other assumptions for the 4-

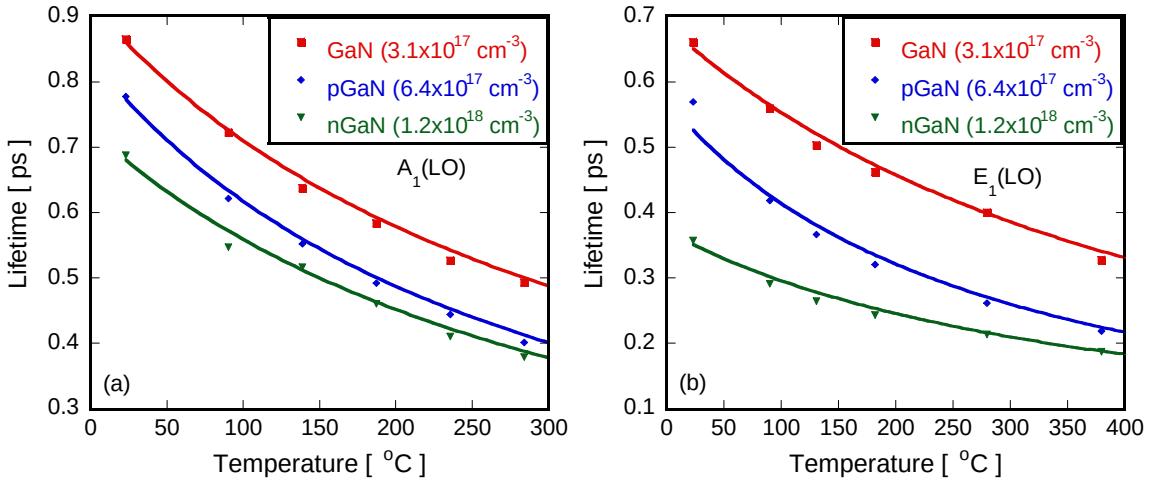

Figure 42. Lifetime of the (a) A_1(LO) and (b) E_1(LO) mode as a function of temperature. Unlike the E_2^{High} mode, the lifetimes of the LO modes remain distinct across the entirety of the examined temperature range indicating interaction with the free carriers. As expected, the lifetimes decrease with an increase in free carrier concentration.

phonon process, the temperature dependence of the A_1(LO) and E_1(LO) modes was modeled for each of the different samples with excellent correlation as seen in Figure 42. From these fitted models, the ratio of Γ_0/Γ_1 was found to be >50 for each case illustrating the clear dominance of the 3-phonon decay process. The pathway for these transformations are shown in Figure 43 where it is evident that decay into the TO mode at a wavenumber of ~530 cm^{-1} indeed occurs. In light of these results, it becomes apparent that the avenue for decay of the phonons themselves is independent of carrier concentration.

Due to intense Fröhlich interaction, the higher energy optical modes heavily interact with free carriers [153, 174]. Recently, this has been shown experimentally as under non-equilibrium fields the phonon lifetime of the A_1(LO) mode is observed to vary inversely with the free carrier concentration [157, 158]. In this study, however, the incident laser light is below the bandgap of the GaN and the equilibrium response of the

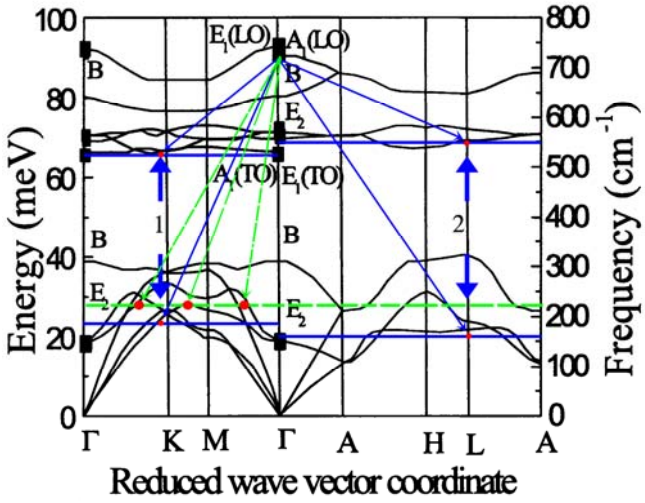

Figure 43. Dispersion curve of wurtzite GaN as reported by Siegle *et al.*[177]. The asymmetric decay of the LO phonons occurs via decomposition into a TO mode. Notice that although the 4-phonon process may occur via the dashed line, 3-phonon processes dominate in the determination of the lifetime for these modes. Note that although only the A_1(LO) pathways are shown, pathways for the E_1(LO) mode are extremely similar.

crystal is probed instead. Yet despite this significant difference between the conditions in this study and those previous, a similar trend for the A_1(LO), as well as the E_1(LO) mode, is found as lifetime is seen to decrease across all temperatures with an increase in free carrier concentration (see Figure 42). Quantitatively, this trend is exhibited at room temperature where lifetimes of the A_1(LO) mode were found to vary between 0.86 and 0.69 ps across a carrier concentration range of $3.1x10^{17}$ to $1.2x10^{18}$ cm^{-3}. These values are within the lifetime range of 2 to 0.51 ps recently reported by Tsen *et al.* [158] for GaN in a similar concentration regime.

The dependency of the lifetime to doping concentration occurs due to direct interaction of the phonons with the carriers rather than differences in the microstructure arising from to the doping procedures themselves. While the doping process does induce distortion of the lattice, and hence strain fields that affect phonon scattering, these

microstructural effects are not the dominant scattering source. Rather, it is the carriers themselves that weigh most heavily on the scattering of the LO modes. This is first indicated upon investigation of Figure 42 where the lifetimes do not converge at higher temperatures. The lack of convergence indicates that phonon-phonon scattering is not the dominant mechanism as was the case for the non-polar E_2^{High} mode. Hence, an additional source of scattering either in the form of microstructural differences or direct carrier/phonon interaction must be present even at these higher temperatures.

To ascertain the nature of this additional scattering source, it is useful to examine the rate of change of the lifetime with respect to temperature ($\partial\tau/\partial T$). Utilizing the derivative is pertinent, allowing for the removal of microstructural effects as, again, this scattering source remains largely constant with temperature. Consequently, through examination of the derivative only the effects of phonon-phonon and phonon-carrier scattering are investigated. Hence, due to the sample's common dispersion, a

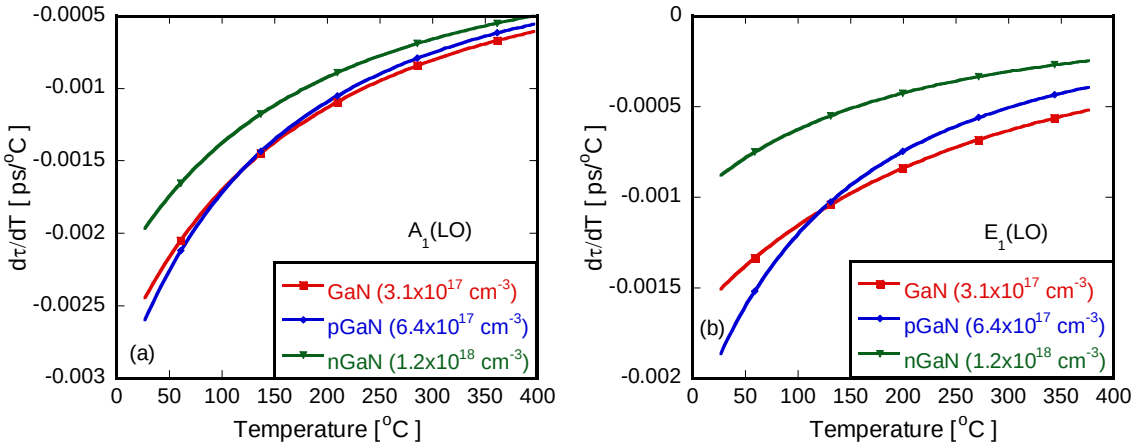

Figure 44. Rate of change in the lifetime of the (a) A_1(LO) and (b) E_1(LO) mode with respect to temperature. Utilizing the rate of change isolates the source of scattering to only other phonons and free carriers. As the phonon-phonon scattering is equivalent between each of the samples, the discrepancy in the rate of change indicates that differences in the lifetime values may be attributed to direct phonon-carrier interaction.

convergence of the lifetime's derivative with respect to temperature indicates that phonon-phonon scattering is dominant and thus differences in the actual lifetime evolve from microstructural differences. Upon investigation of Figure 44, however, it is seen that for each LO mode the rate of change of the lifetime remains distinct at all temperatures. This result indicates that the dominant source of scattering varies in its temperature dependent population between each of the specimens examined. It may then be deduced that it is the carriers themselves that directly interact with the LO modes.

4.3.4 A_1(TO) Phonon Decay Channels and Carrier Dependency

Charge carriers in GaN strongly interact with the LO optical modes and thus several researchers have concentrated on the lifetimes of these polar optical phonons. However, as shown in the previous section, the LO modes undergo asymmetric decay into

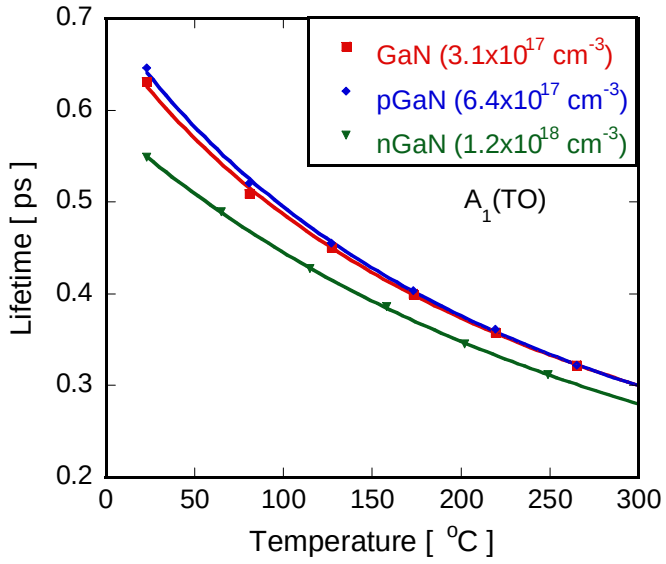

Figure 45. Lifetime versus temperature for the A_1(TO) mode. Although convergence is seen at higher temperature for the lower doped samples (GaN & pGaN), the higher doped nGaN specimen has a lifetime clearly distinct from these other two specimens raising suspicions that carriers may interact with this mode.

transverse optical (TO) modes. Thus, understanding the lifetimes and decay mechanisms of these transverse optical modes is also necessary to elucidate the entirety of the phonon energy cascade into acoustic modes. To this end, the temperature dependence of the A_1(TO) mode was fit using Equation (33) as shown in Figure 45. For each sample, excellent correlation between the model and data is achieved assuming symmetric decay for the 3-phonon process ($\omega_o/2 \sim 266$ cm^{-1}) along with an associated value of $\omega_o/3$ utilized for the 4-phonon process. This decay pathway is viable as indicated in Figure 46 by the points of intersection annotated along the constant energy lines of 266 cm^{-1} and 177 cm^{-1} corresponding to the 3 and 4 phonon processes, respectively.

Further examination of Figure 45 displays convergence of the lifetime at higher temperatures for the lower doped samples (GaN & pGaN) while the lifetime of nGaN specimen is continually lower. This difference with doping does not arise due to direct interaction of the phonon with the carrier, however, but rather as a consequence of

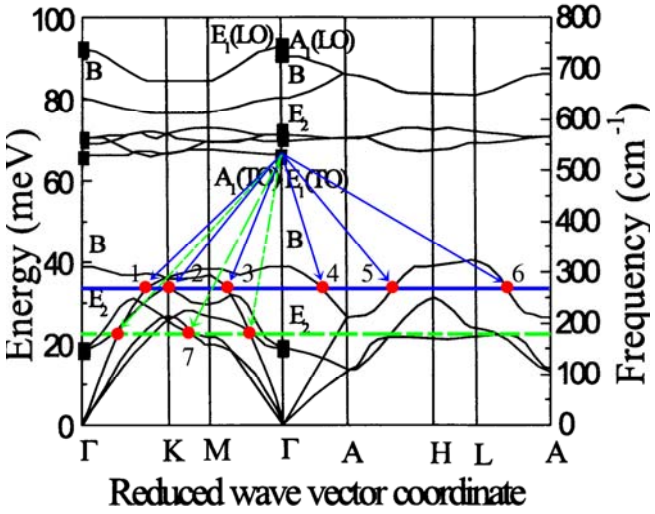

Figure 46. Dispersion curve of wurtzite GaN as reported by Siegle *et al.* [177]. Decay for the A_1(TO) occurs via both 3-phonon processes (solid line) and 4-phonon processes (dashed line).

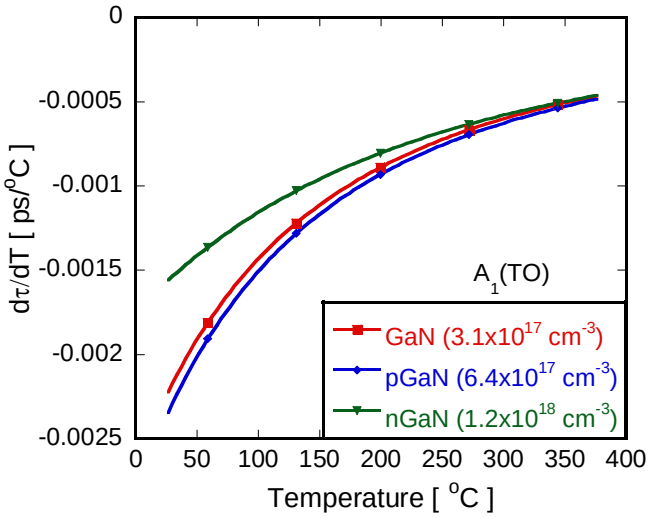

Figure 47. Rate of change in the lifetime of the A_1(TO) and with respect to temperature. Convergence in this rate of change is seen for each of the differently doped samples indicating the absence of any phonon-carrier interaction. Consequently, differences in the lifetimes arise due to interaction with the microstructure.

heavier scattering with the microstructure in the nGaN sample. Figure 47 verifies this assertion as the rate of change of the lifetime with temperature converges for each of the samples. This indicates that the temperature dependent scattering sources are similar in each of the samples and thus carrier interaction does not occur. Thus, carrier interaction does not permeate through the entirety of the energy cascade. Instead, energy flows regardless of carrier concentration once decay from the higher energy LO modes is accomplished.

4.4 Summary

Using the energy-time uncertainty relation, phonon lifetimes were measured for four different optical modes in a series of gallium nitride samples each having a different free carrier concentration. By measuring the lifetimes across the typical operating temperature spectrum for GaN devices, decay mechanisms and pathways for each of the

different modes were deduced. Lower energy modes were found to decay via a combination of symmetric 3-phonon and 4 phonon processes. In contrast, the higher energy LO modes decomposed primarily via asymmetric 3-phonon Ridley decay. Through use of previously determined dispersion relations, a graphical technique accounting for both the conservation of energy and phonon momentum allows for visualization of the entire energy cascade. The effect of free carrier concentration on phonon decay was then examined for each of the four modes through analysis of both the lifetime and the rate of change of lifetime with respect to temperature. Through this analysis, it was found that only the high energy LO modes directly interact with the free carriers while the modes into which the LO modes decay are independent to their presence. Consequently, upon decomposition of an LO mode, energy propagates independent to the presence of carriers. Therefore, the most significant bottleneck to energy dissipation in GaN devices occurs as a result of the inefficient decay of the LO modes into lower energy lattice vibrations. Future studies should then focus on limiting the ability of free carriers to reabsorb these polar modes in order to maximize energy transfer thereby limiting the likelihood of hot spot formation.

CHAPTER 5

ESTIMATING THE EFFECTS OF DISORDER ON THERMAL BOUNDARY CONDUCTANCE OF GAN/SUBSTRATE INTERFACES

5.1 Overview and Approach

The transport of thermal energy across material interfaces is playing an ever increasing role in the response of thin-film and nanostructured devices. Thermal boundary conductance (TBC), which describes the efficiency of heat flow at material interfaces, is a concept that must be understood in order to control the thermal response of material systems such as superlattices, thermoelectrics, nanocomposites, and even high power electronics. While much effort is underway to predict and understand TBC from atomistic calculations, a need remains for more simple analytical calculations capable of capturing the salient transport mechanisms apart from intense computational rigor. This is especially true when considering the impact of interfacial disorder on the thermal boundary conductance.

For AlGaN/GaN devices, the process of heat dissipation is complicated by the numerous interfaces that exist between the active device layer and the supporting substrate. The large number of interfaces occurs as a result of the heteroepitaxial growth process, which requires either lattice matching of the active layer to the substrate or the growth of intermediate buffer layers to accommodate the lattice mismatch between the two materials. Since it is difficult to find perfectly lattice matched substrates to nitride semiconductors, buffer layers or specific ternary alloys must be used near the substrate to allow for the construction of high quality devices. These extra layers, and the associated

increase in the number of interfaces, undoubtedly affect the transmission of thermal energy from the device as a whole. However, little work has been done to elucidate the nature of this interfacial resistance even though its magnitude has been shown to influence the temperature of GaN based HEMTs by as much as 60% [178] .

Obtaining estimates on thermal boundary conductance in thin-film semiconductor devices is often very challenging. Experimental methods involving 3-ω and transient thermoreflectance have been performed on multiple layers of heterogeneous materials from which the boundary resistance is calculated assuming known properties of the adjoining materials [179-182]. While these techniques have worked well, it is impractical to experimentally measure all permutations of material and interface structure. Thus the development of predictive methods for such parametric studies is of primary importance.

Significant attention has been paid to molecular dynamics and atomistic models where the interfaces can be explicitly prescribed. Not surprisingly, significant work has been devoted to silicon systems and in particular Si/Si grain boundaries. Specifically, the analysis of well-defined phonon wave packets and their transmission at interfaces has been performed using atomic level simulations to determine thermal boundary conductance [183]. This wave packet approach has been utilized as well, in conjunction with more traditional molecular dynamics, to analyze the TBC of imperfect hetero-interfaces with emphasis being placed on inelastic scattering [184]. Importantly, these studies have showed that the degree of disorder at the interface is a major determinant of the effective conductivity of an entire device [185].

The role of disorder is particularly important in GaN devices as most interfaces between thin films contain at least some degree of intermixing dependent upon the processing methods employed. While atomistic modeling may capture details of the thermal energy transport across such disordered interfaces, it remains a daunting task to model all permutations of structural disorder that can be encountered in a real system. Thus, higher length scale analytical models, which contain some statistically averaged quantities from the microstructure, may provide a more tractable solution to such a problem.

The use of analytical models to estimate thermal boundary conductance between materials has frequently relied on the diffuse mismatch model (DMM) [179]. This method assumes that when a phonon interacts with an interface, it is diffusively scattered and hence transmission is dependent upon the ratio of the densities of states between the two materials. Using this ratio, a transmission coefficient is calculated and the thermal boundary conductance is found by integrating over all phonon frequencies taking part in the thermal transport. Inherent in the diffuse scattering assumption is that some degree of roughness or disorder is present at the interface. However, the nature of this roughness cannot be accounted for in any explicit or implicit manner using the DMM.

Approaching the Debye temperature, smaller phonon wavelengths are excited in the material increasing the likelihood of multiple scattering events at a rough interface resulting in an overall decrease of the TBC. As the DMM predicts only a singular diffusive scattering event, it is not surprising the model overestimates TBC in acoustically similar materials with disordered interfaces such as is the case in GaN devices [179, 186, 187]. To improve upon the DMM, previous studies have largely

focused on either using a more realistic density of states or investigating the extent to which phonons are indeed diffusively scattered [187, 188]. While enhancements to the analytical approach of calculating TBC have been made through these efforts, there still exists a need to account for the degree of interfacial disorder in the estimation. This work seeks to account for this irregularity of an interface in order to produce a method that quickly estimates the thermal boundary conductance while lending insight into the sensitivity of material systems to interfacial quality.

To account for the interfacial disorder, a virtual crystal (VC) approximation within interface will be made. In the virtual crystal approximation, the disordered region is replaced by a homogenized virtual crystal having effective properties based on the disordered medium [189]. Using this approach, transmission coefficients can be calculated on both sides of the homogenized crystal. Dependence of the thermal boundary conductance on the degree of disorder can then be examined by altering the composition of the virtual crystal. Thickness of the disordered interface is addressed through scaling of the conductance with respect to both the phonon mean free path in the virtual crystal and the thickness of the disordered region. Through these extensions, a model is available that can approximate the effects of interface structure on thermal boundary conductance.

The virtual crystal diffuse mismatch model (VCDMM) is initially demonstrated through analysis of a chromium (Cr) and silicon interface that has been experimentally probed such that comparisons between the predicted and measured values of the thermal boundary conductance are possible. With the model verified, the sensitivity of the thermal boundary conductance to interfacial disorder is analyzed for GaN systems. In

this manner, substrates frequently employed in GaN devices, specifically Si, SiC, and sapphire, are compared as to their capability and robustness to transmit heat across the interface and away from the active region of the device.

5.2 Theory and Derivation of Virtual Crystal Diffuse Mismatch Model (VCDMM)

The diffuse mismatch model calculates the thermal boundary conductance according to the following relation:

$$h_{INT} = \sum_j h_{1-2,j} = \sum_j \frac{1}{4} \int_0^{\omega_{\max}} \left(\frac{dN_{1,j}}{dT} \right) \hbar \omega \alpha_{1-2} c_{1,j} d\omega \tag{34}$$

where $h_{1\text{-}2,j}$ is the TBC for a particular mode j, ω_{max} is the Debye cutoff frequency, $\hbar$ is the modified Planck constant, $c_{1,j}$ is a given mode velocity, and N_j is the phonon population for the temperature and mode of interest based on Debye theory. Of special note is the transmission coefficient, α_{1-2}, which quantifies the percentage of phonons able to forward scatter from side 1 to 2 and hence transmit thermal energy. The transmission coefficient is found to be a ratio of the phonon propagation speeds in each material:

$$\alpha_{1-2} = \frac{\sum_j c_{2,j}^{-2}}{\sum_j \left(c_{1,j}^{-2} + c_{2,j}^{-2} \right)}. \tag{35}$$

In the diffuse mismatch model, it is assumed that the interface can cause only a single diffuse scattering event, neglecting any possibility that a phonon may be scattered multiple times. However, if there is a finite thickness of disorder at the interface, the assumption of a single scattering event may not be satisfied. In considering the interface between two materials, an interphase region of appreciable thickness with properties much different than those of the materials on either side may exist. Since the diffuse

mismatch model cannot address this situation, it may be limited to applications of a perfect interface or where the interphase region is very small compared to the wavelength of the dominant heat carriers.

Modeling the interphase region is extremely complex as details of its structure and composition are not fully known. On the other hand, effective material properties that homogenize the interphase can yield some insight into the region's impact on TBC. Using such a method to estimate properties was first proposed by Abeles while investigating the thermal conductivity of mixed crystal alloys [189]. In this manner, prediction of the thermal conductivity in alloys such as SiGe was made possible over a wide range of compositions.

Through utilization of the virtual crystal approach, the interphase region is replaced by a virtual crystal, creating an interface with materials 1 and 2 as shown in Figure 48. The total thermal boundary conductance is then found by finding the equivalent conductance of the two interface system,

$$h_{INT} = \left[\left\{ \sum_j h_{1-vc,j} \right\}^{-1} + \left\{ \sum_j h_{2-vc,j} \right\}^{-1} \right]^{-1}. \tag{36}$$

To calculate the conductance between a material and the virtual crystal, Equation (34) is used with modifications to account for the effects of the virtual crystal. The only term that must be changed in this expression is the transmission ratio, which will be modified by the presence of the virtual crystal. Equation (35) is now applied between material 1 and the virtual crystal as well as material 2 and the virtual crystal in order to calculate the TBC in Equation (36).

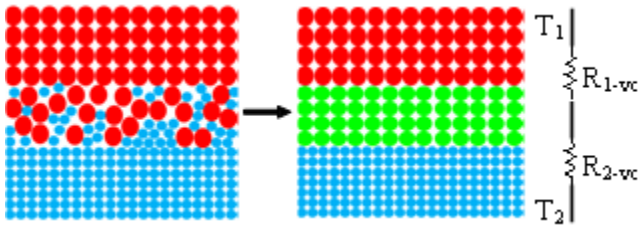

Figure 48. Schematic representation of the virtual crystal interface accompanied with associated heat resistance circuit. The interface region is replaced with a homogenized virtual crystal across which the phonon transmission coefficients are calculated leading to TBC predictions.

To calculate the unknown phonon propagation speeds in the virtual crystal required in Equation (35), Debye theory may be used as proposed by Abeles [189]. However, this methodology requires knowledge of the elastic constants of the virtual crystal. Near the interface, however, estimation of these constants is quite difficult due to the inherent randomness of the interface. As a consequence, it is assumed in this approach that the propagation can be modeled simply as a composite of the speeds of the host materials as shown below, where b_1 is the percentage by mass of material 1 in the VC,

$$c_{VC,j} = b_1 \cdot c_{1,j} + (1 - b_1) c_{2,j} . \tag{37}$$

In considering the disorder analysis above, the depth of disorder has not been considered. To incorporate the effect of this interface thickness a dimensionless parameter, the depth factor δ, is introduced,

$$\delta_j = D' / \Lambda_{VC,j} . \tag{38}$$

In Equation (38), D' is the actual depth or thickness of the interface while $\Lambda_{VC,j}$ is the mean free path of the virtual crystal for a particular mode. This mean free path is calculated from kinetic theory using the relation between thermal conductivity, average phonon speed, and specific heat in the bulk,

$$\Lambda_{VC,j} = \frac{3K_{VC}}{C_{vc}c_{j,VC}}. \tag{39}$$

Calculation of the thermal conductivity in the virtual crystal is accomplished using the original approximation method by Abeles [189] while all other parameters are estimated using the rule of mixtures as in Equation (37). The depth factor relates the relative region of disorder to the dominant mean free path of the heat carriers. In this case, if $\delta > 1$, it is possible that the phonons can scatter multiple times in the interphase region. Thus, the boundary conductance should scale with this factor. As such, the depth factor is used to modify Equation (36) into the final form for evaluation of the thermal boundary conductance using the virtual crystal diffuse mismatch model (VCDMM),

$$h_{INT} = \left[\left\{ \sum_j \frac{h_{1-vc,j}}{\delta_j} \right\}^{-1} + \left\{ \sum_j \frac{h_{2-vc,j}}{\delta_j} \right\}^{-1} \right]^{-1}. \tag{40}$$

In the case of metal-dielectric interfaces, the effect of electron-phonon coupling resistance should be accounted for by including the method of Majumdar and Reddy [190].

5.3 Validation of VCDMM via Analysis of a Cr/Si Interface

To compare the current model to experimental data, the interfacial thickness, *D'*, as well as the composition, *b*, of a disordered region must be known. Hopkins *et al.* [191, 192] examined the effect of these parameters on TBC using both Auger spectroscopy and a transient thermoreflectance technique for a series of chromium/silicon interfaces. Using the reported interfacial thicknesses and deriving the virtual crystal composition from the given elemental concentration profiles, it is possible to compare the measured values of TBC to those predicted from the virtual crystal approach. These comparisons were

Table 5. Comparison of thermal boundary conductance (TBC) calculated from the virtual crystal diffuse mismatch model (VCDMM) to measured values for several Cr/Si interfaces [191, 192]. For each interface examined, the prediction is within 18% of measured value.

Interface Thickness [nm]	Virtual Crystal Comp. (% Si)	Measured TBC [GW/m^{2}K]	VCDMM [GW/m^{2}K]	DMM [GW/m^{2}K]
9.5	0.54	0.178	0.147	0.855
14.8	0.67	0.113	0.118	0.855
11.5	0.66	0.139	0.146	0.855
10.1	0.48	0.150	0.131	0.855

carried out including electron-phonon coupling resistance using the value for chromium reported by Hostetler *et al.* [193] and material properties obtained from Swartz and Pohl [179]. Shown in Table 5 is a comparison of the virtual crystal model to the experimental data where in each case the VCDMM is within 18% of the measured values. From the table, it can be seen that increased interfacial thickness results in a reduction in TBC as the number of scattering events increases. These additional scattering mechanisms reduce the rate at which energy can be transported across the interface causing a decrease in the TBC.

While the thickness of the interface region plays a strong role in the TBC, the disorder within that phase also limits thermal transport due to the increase in scattering sites inherent with a loss of regular periodicity. This effect is seen in Figure 49 for an interface between Cr and Si of thickness 9.5 nm for which the composition of the VC is allowed to vary from 10 – 90% Si. When the concentration is near one-half, and disorder is maximized, TBC is minimized following the same qualitative trend of the effective thermal conductivity as predicted by the Abeles mixed crystal thermal conductivity model.

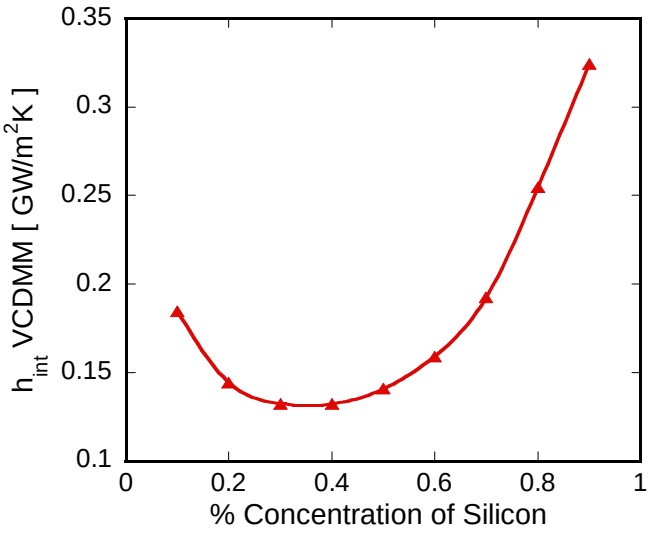

Figure 49. Thermal boundary conductance of a 9.5 nm Cr/Si interface as a function of Si content. The model shows a minimum thermal conductance occurring near 40% fraction of Si due to a peak in phonon scattering and an associated minimization of thermal conductivity.

5.4 Analysis of TBC in GAN/Substrate Systems using the VCDMM

A recent study by Fillipov *et al.* [178] has demonstrated that the maximum device temperature in a GaN based HEMT may depend on the thermal boundary conductance by as much as 60%. Due to this significant dependence, it is relevant to evaluate the different interfaces commonly present in GaN devices through use of the virtual crystal diffuse mismatch model. Specifically, the relative effects of interface quality (i.e., interface disorder and thickness) are investigated for substrate materials frequently used with GaN, namely sapphire, SiC, and silicon. This is accomplished by examining each material interface across a range of thicknesses ranging from 0-200 nm for each different combination of concentration from 0.1 to 0.9. The material properties utilized in each calculation are given in Table 6 where all simulations were assumed to take place at 300K.

Table 6. Material parameters utilized in simulation. (Values courtesy of [179, 194, 195])

Material	Density [g/cm^3]	Longitudinal Phonon Velocity [m/s]	Transverse Phonon Velocity [m/s]	Transverse Phonon Velocity [m/s]
GaN	6.15	7960	4130	6310
SiC	3.21	9500	4100	4100
Sapphire	3.97	10890	6450	6450
Silicon	2.33	8970	5332	5332

Using these simulation parameters, the TBC of the differing systems at a practically perfect interface (D'=0 nm, b=0.9 GaN) ranged in values from 0.203 GW/m^{2}K for silicon to 0.095 GW/m^{2}K for SiC. These values over predict the values of analogous systems measured by Sarua *et al.* [79] by as much ~50%. However, if the interface is assumed to extend for 30 nm in conjunction with the reported thicknesses of the nucleation layer used in this reference [79], correlation is found between the range of values reported experimentally and those predicted from the VCDMM. This fact provides confidence in the implementation of the model with respect to GaN systems and allows for further investigation into this type of interface.

The quality of any interface is a function of the disorder of that interface and the thickness to which this disorder persists. Using the virtual crystal method, the thickness is modeled using the depth factor of Equation (40). Shown in Figure 50 is the effect of the interfacial region on the thermal boundary conductance assuming that the GaN composes 30% by mass of the virtual crystal. As the extent of disorder at this interface persists, the TBC of the system falls as the likelihood of multiple scattering events increases. This fact is particularly evident as each of the materials displays a more than 50% reduction in interfacial conductance once the disorder extends to only 20 nm.

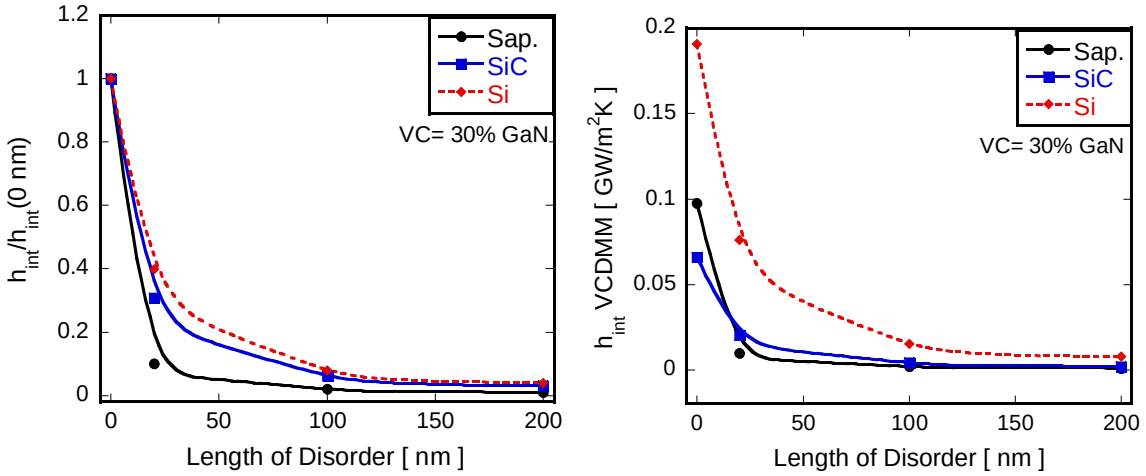

Figure 50. Prediction of TBC (left) using the VCDMM for a GaN on sapphire, SiC, or Si system as a function of the length of interfacial disorder. The sapphire system, although having a higher predicted TBC for a perfect interface, shows a higher sensitivity as displayed from the normalized values (right) to the persistence of disorder than do the other materials.

Particularly vulnerable to this disorder is the sapphire system, which suffers from a reduction in the TBC of 90% with the introduction of thickness effects. As a consequence, the sapphire boundary demonstrates a TBC lower than that of the SiC system despite its initially higher value in the limit of a perfect interface. Consequently, when introducing a GaN/sapphire system, the quality of the interface is of significant importance in the optimization of the TBC and hence the overall thermal capability of the device.

In addition to thickness, the actual degree of disorder in the interfacial region also plays a role, albeit a lesser one, in the determination of the thermal boundary conductance. Figure 51 shows the decrease in TBC that occurs for each type of material system as the disorder is increased. Notice that the minimum TBC occurs when the disorder is maximized, i.e., virtual crystal concentrations between 0.4 and 0.6, resulting in small decreases in the TBC. This decrease is due to the reduction in phonon

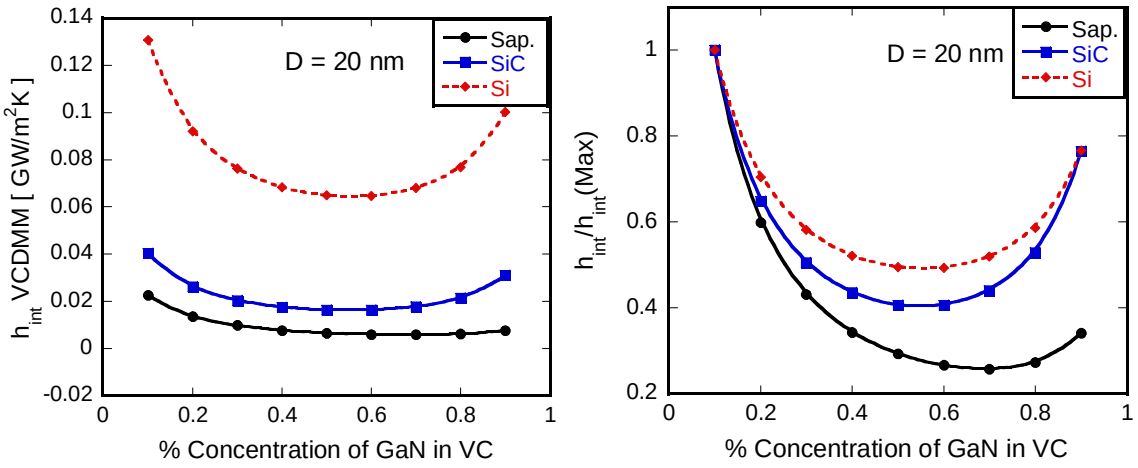

Figure 51. Dependence of TBC on degree of disorder for a GaN on sapphire, SiC, or Si system. Both the magnitude (left) and normalized values (right) show, once again, that sapphire is acutely sensitive to an increase of disorder.

transmission that arises with the increasing number of scattering sites that inherently scale with the degree of disorder. The magnitude of this reduction relative to the depth factor is smaller, however, indicating that phonons are more sensitive to the extent rather than the degree of disorder.

The material systems scale in their sensitivity (i.e., % reduction in TBC) to the degree of disorder at a rate that is inversely related to the magnitude of their "ideal" TBC. More simply, the material systems that have higher TBC seem to be more robust in the face of reduced interfacial quality than do those with lower interfacial heat transfer capabilities. Therefore, as this result is common to the extent of disorder as well, it is indispensable when a lower performing system is utilized that fabrication methods be employed that maximize interfacial quality due to these systems greater sensitivity to a non-ideal boundary.

5.5 Summary

An extension of the diffuse mismatch model is presented for disordered interfaces. Utilizing a virtual crystal approximation for the interface, it is possible to estimate the thermal boundary conductance for interfaces with finite thickness and disorder. While the model qualitatively follows the trends of limited experimental data on this topic, additional effects must still be added to this approach to capture the temperature dependence of both the phonon mean free path and TBC. However, the current approach shows a simplistic method that captures physically motivated phenomena offering improvements over the diffuse mismatch model thus allowing for investigation into the sensitivity to disorder for a series of GaN/substrate systems. Through this study, the extent of disorder was found to have a greater effect on the thermal boundary conductance than did the degree of intermixing while also demonstrating that those substrates having lower interfacial transport capabilities were more acutely sensitive to the presence of these disorder effects.

CHAPTER 6

SUMMARY, OPPORTUNITIES, AND CONCLUSIONS

6.1 Summary

The evolution of temperature and stress in AlGaN/GaN HEMTs directly impacts both the performance and reliability of this promising device class. It is necessary that characterization methods be utilized that are capable of measuring each one of these parameters simultaneously present during operation. Due to its non-invasive nature and favorable spatial resolution (~1 μm), Raman spectroscopy is often employed to investigate both the thermal and mechanical environments of GaN materials. Difficulties arise, however, as the most common implementation of the technique monitors changes in the Stokes peak position that are sensitive to strains arising from both thermal and elastic sources. This dual sensitivity, in turn, significantly limits the measurement of either temperature or stress in their concurrent presence as the signal becomes convoluted due to each contribution. In response, this study has re-examined the use of Raman spectroscopy in the characterization of GaN systems. Specifically, an original implementation has been described that allows for the simultaneous investigation of the thermal and mechanical response of GaN microelectronics. The following serves as a summary of this technique, highlighting the major findings found through its development and initial application.

6.1.1 Micro-Raman Thermometry in the Presence of Complex Stresses in GaN Devices

The measurement of temperature is particularly salient in the analysis of AlGaN/GaN HEMTs as both the performance and reliability of the device scale inversely proportional to the magnitude of the thermal load. Raman thermometry has proven particularly useful in this analysis as its spatial resolution and non-invasive probing make it alluring in the acquisition of quick and accurate measurements. Most frequently, these measurements take place through the analysis of the Raman signal's peak position to deduce temperature. While this aspect of the signal is easy to work with and acquire, it is dualistically sensitive to strains arising from both thermal expansion and elastic (stress) effects. As a consequence, when a material is simultaneously subject to thermomechanical loading, such as that present during AlGaN/GaN HEMT operation, the measurement of temperature using the peak position becomes biased.

To compensate and quantify this effect, this study examined the full response of the Raman signal, including the linewidth (FWHM) and Stokes to anti-Stokes ratio as well as the peak position, to strains arising from thermal, elastic, and inverse piezoelectric effects. The peak position, as expected, was found to be distinctly dependent on each type of strain. This dependence, in turn, caused large under predictions in the subsequent temperature measurements of both a TLM and HEMT device subject to comparatively large thermoelastic and inverse piezoelectric stresses, respectively. These errors, however, were found to be avoidable through the utilization of an alternative aspect of the signal dependent only to thermal effects. This fact was demonstrated through incorporation of the ratio of Stokes to anti-Stokes intensity, which is only dependent on

temperature irrespective of strain. Consequently, utilizing this method, temperatures were measured in both devices at levels nearly identical to that predicted through finite element simulation.

While indisputably capable of measuring the temperature, the ratio of the Stokes to anti-Stokes signals is quite difficult to implement in practice and, at a minimum, requires twice as much experimental time as both portions of the Raman signal must now be acquired. Due to these difficulties, it is desirable that a third aspect of the spectral signal be resolved to measure the temperature. This study has focused on the implementation of the linewidth (FWHM) of the Stokes response due to this spectral artifact's dependence on the lifetime and, as a derivative the population, of the phonon mode. As a consequence, it was found that the linewidth was capable of measuring temperatures in the presence of thermoelastic stresses in GaN devices without any need for correction. However, the linewidth was found sensitive to the presence of the piezoelectric loads present during operation of AlGaN/GaN HEMTs. While this sensitivity may be removed through proper choice of a biased reference condition, its physical causation remains unclear. Regardless, the linewidth allows for the measurement of temperature in GaN devices apart from the effects of strain without the need for the acquisition of the anti-Stokes signal.

TAKEAWAY:

A key tool in the analysis of AlGaN/GaN HEMTs, Raman thermometry most often utilizes the peak position to acquire temperature despite significant errors that arise due to the sensitivity of this spectral component to elastic as well as thermal effects. To remove these errors, this work has demonstrated linewidth based Raman thermometry allowing

for unbiased temperature measurements in operating microelectronics acquired from sole use of the Stokes signal.

6.1.2 Assessment of Residual, Piezoelectric, and Thermoelastic Stress Levels in AlGaN/GaN HEMTs

AlGaN/GaN HEMTs achieve their great capability as a direct result of the intense aggregation of carriers that occur at the interfaces between the constituent GaN layer and its alloyed counterpart. This carrier accumulation transpires in response to the polarizing fields present in the materials stemming from not only spontaneous sources but so too those of the piezoelectric variety. These piezoelectric polarizations, in turn, evolve as a direct consequence of the strain and, hence, stress present in the system. As such, these stresses are a major determinant in the resulting performance and reliability of the devices. It is, therefore, pertinent that these stress levels are accurately characterized.

While Raman spectroscopy has been utilized in the estimation of residual and piezoelectric stress levels, operational thermoelastic stresses have been impossible to obtain owing to the simultaneous presence of strains arising from both thermal expansion and elastic responses. Estimation of these thermoelastic stresses is possible, however, if the thermal and elastic strains may be deconvoluted from one another. With respect to the Raman signal, the peak position displays a linear dependence on each type of strain causing the total response to be a superposition of each effect in their dual presence. In order to deconvolute the peak position signal, and thus pave the way for the measurement of the thermoelastic stress, all that is needed is a stress independent measurement of the temperature. Once again, the linewidth of the same Stokes signal is capable of providing

this stress independent measurement, which allows for the peak position to be utilized in the interrogation of the operational thermoelastic stress.

The developed approach is first demonstrated on a silicon based MEMS device where the estimated levels of thermoelastic stress were found to closely correlate with those obtained from a finite element simulation of the system. Subsequently, similar correlation between experiment and simulation was found in the analysis of GaN based TLM and HEMT devices. Despite the agreement, as the technique uses two independent measurements in tandem (peak position and linewidth), uncertainty levels in the resulting measurements may be quite high. It was found that these levels may be mitigated, however, through fitting of the raw experimental temperature (linewidth) data to an expected profile. With this correction, the scatter is reduced substantially and allows for the estimation of operational thermoelastic stress with micron resolution.

With this new capability, it is possible to compare the relative magnitude of each stress component - residual, piezoelectric, and the now observable thermoelastic - present during the operation of an AlGaN/GaN HEMT. This assessment was acquired through analysis of two series of devices grown atop either a silicon or silicon carbide substrate. Due to the vastly different coefficients of thermal expansion between the materials, the devices grown on a silicon substrate were found to have much larger residual tensile stresses than those grown on the more forgiving SiC. Similarly, as power dissipation increases in the device, compressive stress levels in the Si series of devices dwarf their SiC counterpart while, in contrast, the piezoelectric induced stresses are comparable between each type of transistor. Despite the differences in the magnitudes of each component stress, the resultant load in the devices is comparable at higher levels of input

power as the dominating residual stress is counteracted in almost equal measure by the evolving thermoelastic load. Surprisingly, due to the dominance of the residual stress, the silicon series of devices persistently operate in a resultant state of tension while those grown on SiC perform in compression. This fact may have distinct ramifications as the number of carriers in the channel, and hence the capability of the device, is dependent upon the nature of the stress.

TAKEAWAY:

The measurement of operational stress in GaN devices has not been reported due to the difficulty in deducing loads when strains arise simultaneously from thermal, piezoelectric, and elastic sources. As the stress state is central to the performance and reliability of these microelectronics, this study has developed a methodology capable of quantifying the operational thermoelastic stress, and in turn the total elastic load, through tandem use of the Raman signal's peak position and linewidth.

6.1.3 Temperature and Doping Dependence of Phonon Lifetimes and Decay Pathways in GaN

Beyond making quantitative observations of the thermal environment, Raman spectroscopy is also capable of providing conceptual insight into the mechanisms leading to the measured magnitudes. Once more, this capability arises as a direct consequence of the linewidth of the Stokes signal. This spectral feature is determined by the lifetime of the analyzed phonon and, as such, is directly related to the scattering and lattice transport mechanisms at play in the material. These lattice transport mechanisms, in turn, are a major determinant in the transport of thermal energy in the GaN material system,

and thus their investigation provides a method in which the energy "flow" through the material may be observed.

In a GaN device, the flow of energy begins with the application of an electric bias, or potential, which serves to accelerate electrons through the material. Due to the polar (ionic) nature of the GaN, these electrons then dissipate their energy through intense emission of the Raman "visible" high energy longitudinal optical (LO) phonons. These high energy optical phonons, however, act as thermal reservoirs due to their low group velocity and must decompose into lower energy faster moving acoustic phonons in order to dissipate this excess "heat." The decomposition mechanisms of the high energy-slow moving optical phonons and the parameters affecting this decomposition are then critical to the total thermal management of GaN devices. In response, this study has examined these decomposition mechanisms and their dependence upon the number of carriers in order to identify the chief bottlenecks in the transport of thermal energy.

Through measurement of the lifetime of several phonon modes at a series of temperatures via the linewidth, the pathways of decomposition were identified through the development of a graphical technique used in conjunction with the GaN dispersion curve and theoretical prediction centered on the energetic character of the decomposition. It was found that these pathways were invariant for all concentrations of carriers indicating that the lattice/lattice scattering takes place independent of the electronic milieu. In contrast, the rate of decomposition was found to be dependent upon the number of carriers for those modes that are emitted by the electrons. Taken together, these findings indicate that the "flow path" of thermal energy through the lattice takes place independent of the carriers. However, it remains unclear whether the number of

carriers limits the decomposition of the high energy emitted LO modes through reabsorption or if, rather, a new energy dissipating "plasma" channel is created as the number of carriers passes some unknown threshold [158]. Regardless, it is only these emitted LO modes that are significantly affected by the electronic environment as all other modes display independence from this alternate physical environment.

TAKEAWAY:

The rate and manner in which optical phonons decompose plays a central role in the thermal dissipation of energy in GaN devices. Through measurement of the lifetimes of these modes at a series of temperatures, this study has identified the decomposition pathways of several phonon modes and the dependence of their decay rate on the presence of electrical carriers. While the pathways are invariant for all modes irrespective of the carrier concentration, those modes emitted by the carriers decay at a rate dependent upon this concentration highlighting the distinct role that the electronic environment plays on thermal transport.

6.1.4 Estimating the Effects of Disorder on Thermal Boundary Conductance of GaN/Substrate Interfaces

The manufacture of the GaN films comprising the active region of the devices analyzed in this study takes place via an epitaxial growth process atop a substrate. The quality, or ideality, of the interfaces between the GaN and substrate will vary in response to both the processing conditions employed as well as the physical nature of materials themselves. These interfaces, meanwhile, have a distinct effect on the overall thermal transport of the device and may influence the final operating temperature by as much as 60% [178]. Due to this large influence, it is necessary that the nature of this interfacial

thermal transport be understood such that its effect may be minimized. However, as all interfaces are not "created equal," it is equally important that this analysis in some way accounts for the variance in interfacial quality, which is undoubtedly present.

Measurement of interfacial thermal transport, or equally the thermal boundary conductance (TBC), is quite difficult and, as a consequence, most effort centers on simulations of the phenomenon. While the frequently employed atomistic models allow for detailed analysis of the system, computational expense makes their use prohibitive in the analysis of the infinite arrangements of intermixing and disorder that occur with a change in the quality of the interface. In response, this study has developed an extension of a frequently employed analytical prediction to account for the effect of interfacial quality on thermal transport. By incorporating a virtual crystal to represent the finite interfacial region, or interphase, the diffuse mismatch model is scaled to account for the multiple scattering events that take place at a non-ideal interface thus allowing for the prediction to, in some way, account for the effect of interfacial quality. After proving the validity of the approach through correlation with experimentally measured values of a Cr/Si interface, it was found that the length at which disorder persists affects the thermal transport of a GaN/substrate system more than the degree of intermixing that occurs in that interfacial region. Additionally, systems having lower ideal thermal boundary conductance were found to be particularly sensitive to reductions in the interfacial quality. Therefore, to properly account for the thermal boundary conductance during device design, decisions must be weighed not only with respect to material selection but also to a processing recipe maximizing interfacial quality as well.

TAKEAWAY:

Due to the many layered architectures utilized in the design of GaN electronics and micro/nano devices in general, interfacial transport is playing an increasingly important role in the overall thermal response. While analytical models have proven useful in the prediction of this transport, their implementation has been limited to ideal interfaces. This study has demonstrated an analytical model capable of approximating transport through non-ideal interfaces in the prediction of TBC via the development of the Virtual Crystal Diffuse Mismatch Model.

6.2 Opportunities

The present investigation is focused on the development and deployment of new semiconductor characterization methods while concurrently utilizing those techniques in the analysis of GaN devices. As a consequence, future analysis stemming from this work will likely be divided between studies seeking extended optical characterization capabilities for electronic devices, in general, and those focused on the observation and improvement of the AlGaN/GaN HEMT, in particular. In response, the proceeding subsections seek to highlight some of the more promising opportunities for each type of investigation.

6.2.1 Opportunities in the General Characterization of Devices

6.2.1.1 Size Constraints

Electronic devices are continually stretched to produce greater capability in ever smaller footprints. This trend toward smaller and more capable devices has not only lead to greater complications in the prediction and analysis of the response but so too its very

measurement. Oft incorporated optical techniques inherently rest on the supposition that the spatial resolution of the probing radiation provides a spatial resolution sufficient to analyze the device. For radiation in the far field, the implication is that there are no salient features less than the diffraction limit. In the case of visible light, this requires that the device have a "constant" response at length scales less than $\lambda/2 \sim 0.5$ μm. As devices are now commercially available that are designed at length scales over an order of magnitude less than this 0.5 μm figure, characterization techniques capitalizing upon the advantages inherent in non-contact measurements must be developed for these length scales [196].

The most obvious solution towards this objective relies on the development of techniques utilizing incident radiation having wavelengths much smaller than that of visible light. Unfortunately, concomitant with the implementation of these small wavelengths (e.g., X-Ray) comes an associated increase in the amount of energy incident upon the device and thus the likelihood of damage to the sample. In addition, practical utilization of these smaller, higher energy, wavelengths is extremely difficult due to the specialized optics necessary for their use. Therefore, alternative approaches will likely center less on the wavelength of the radiation and more on the methodology by which it is focused. Through the use of either sub-diffraction "superlenses" or near field radiation, spatial radiation less than the diffraction limit may be acquired thereby allowing for the characterization of devices at more pertinent length scales without the complication of utilizing small wavelength probing radiation [197].

6.2.1.2 Two-Dimensional Mapping

Infrared thermography is one of the most popular techniques to investigate the temperature of electronic devices despite the fact that its spatial resolution of ~5 μm would be considered obsolete for most other methodologies. The continued relevance of the technique stems from its capability to quickly and easily acquire a 2-dimensional temperature distribution with a minimal amount of effort. A method that could achieve this capability on a length scale more on par with today's devices would be extremely useful.

In most Raman experiments, the vast majority of the CCD quantifying the amount of light across the spectrum is under-utilized as the peak signal is only present across a very small portion of the detector. If this portion may be quantified, then the surplus of the CCD pixels may then, through appropriate modification of the optics, be utilized to measure this same region of the spectrum at different X-Y locations simultaneously. While this would not allow for the entirety of the device to be mapped in "one shot" as occurs in IR measurements, it would allow for a 2D map with small spatial resolution to be acquired in a much smaller amount of time thereby combining the advantages of IR and micro-Raman thermometry.

6.2.1.3 Simultaneous Electronic-Lattice Characterization

Semiconductor devices have electronic and lattice environments that are inextricably linked. Energy is deposited, via a bias, into the electronic system and subsequently transferred to the lattice where the excess heat must be dissipated. Measurement of the devices, however, typically occurs with respect to only one of these environments even though, in a light scattering event, energy transfer may occur with either the electronic or

lattice environment. Therefore, it should be possible to implement techniques that optically analyze each of these environments simultaneously through proper filtering of the spectral and temporal signals. For example, techniques such as photoluminescence, thermoreflectance and Raman spectrometry may be combined in order to probe the evolution of, among other factors, the electron phonon interaction central to the dissipation of thermal energy in GaN devices [198]. Regardless of the particular implementation, as incident light interacts with both the electronic and lattice environments simultaneously, techniques should be developed that more easily capitalize on the entirety of the signal as both portions of the response could be of value.

6.2.2 Opportunities in the Analysis of AlGaN/GaN HEMTs

6.2.2.1 AlGaN's Role on the Behavior of AlGaN/GaN HEMTs

The operation of AlGaN/GaN HEMTs relies upon a large aggregation of carriers forming along the interface between the alloyed and unalloyed layers. Throughout this study, our analysis has focused exclusively upon the GaN portion of this system with total disregard to the nature of the response in the alloyed layer despite its centrality to the operation of the transistor. This deficiency stems from the fact that the AlGaN layer is quite difficult to investigate in practice, owing to the layer's extreme thinness and similarity in Raman response to the undoped GaN. Future studies should seek to fill this inadequacy.

To compensate for the small signal originating within the AlGaN layer, previous studies have capitalized on near-resonant Raman conditions through use of incident radiation above the band gap of the material in the form of UV radiation [87]. Furthermore, as GaN and its alloys are opaque in this region, the UV light will only

sample from the "top" of the device allowing for the sole interrogation of the AlGaN apart from its unalloyed counterpart. In using an above bandgap source, however, temperature measurements are complicated by the creation of electron-hole pairs that will modify the observed device's operation. Yet since the AlGaN layer has an extremely small thermal signature, its analysis with respect to temperature is not central and thus need not be sought. Rather it is the stressing, and more importantly, the relaxing of this layer that is central to the performance of the device. Therefore, use of UV-Raman should focus on specifying at which conditions, both in operation and processing, relaxation occurs in this alloyed layer.

6.2.2.2 Hot Spot Quantification in AlGaN/GaN HEMTs

In a HEMT device, the electric field achieves its acme and "spikes" just beneath the gate on the side nearest to the drain (see Figure 1). At this location, the potential energy embedded in the bias quickly manifests itself into a severe degree of kinetic energy within the electronic system. All this kinetic energy must in some way be dissipated and, in response, the lattice is heated in a manner that "spikes" with the electric field at this same location. The intense localized heating is termed the "hot spot" and corresponds to the location of maximum load within the device. Due to the high level of load, it is within the hot spot that most failure is believed to originate and thus its investigation and quantification is of prime interest.

Optical access to this region is quite difficult in today's devices, however, due to the employment of T-shaped gates and field plates that act to "hide" the hot spot from standard top-view backscattering methodologies. This problem has been circumvented utilizing Raman spectroscopy imaged through the substrate in conjunction with confocal

microscopy techniques [50]. Even utilizing the confocal capabilities of the spectrometer, however, results in a temperature measurement averaged through a thickness of at least 3 μm due to the dispersing effects of the substrate. Unfortunately, the hot spot is unlikely to extend to such a depth and, as a consequence, the measurements will underestimate the true maximum due to averaging with the adjacent cooler region.

Therefore, an approach employing a through thickness depth of field on par with the hot spot must be implemented in order to quantify the true maximum temperature in the device. As UV light is above the band gap of gallium nitride, it may be employed to achieve this depth of field. For the same reason, however, utilizing this wavelength of incident radiation through the substrate (i.e., from the bottom) would not result in any information being obtained from the AlGaN/GaN layers due to the effects of absorption. It is then necessary that optical access to the hot spot be, in some way, obtained in a standard top view backscattering arrangement. This access is, again, inhibited by the Ti/Al metallic layers of the gate and field plate and thus their effects must be removed. Thus, devices which utilize transparent conductive oxides may provide a logical path forward in investigating these features.

6.2.2.3 Reliability of AlGaN/GaN HEMTs

With continued utilization, GaN based HEMTs suffer from degradation in their operational capabilities. Subject to either RF or DC stress, drain current, output power, and gain each reduce with time causing significant reductions in the overall lifetime and viability of the device. While the observation of this degradation has been reported [2, 9, 13, 14, 16, 18, 20, 22, 34, 35, 42, 199-213], there has been a relatively limited amount of study focused on the mechanisms by which this degradation actually occurs.

At its core, the capability of an electronic device is limited only by the number of available charge carriers and the ability for these carriers to move. Study of degradation is then an examination into the changes in both electronic concentration and mobility with time. In AlGaN/GaN systems, the concentration of electrons occurs as a direct result of large polarizations that arise due to both spontaneous and piezoelectric effects. Any change affecting this polarization will modify the active region of the device and cause a subsequent dispersion in performance. For this reason, it is imperative that each of the mechanisms responsible for changes in the polarization be identified in order to limit HEMT degradation.

In order to maintain charge neutrality upon being polarized, pairs of positively charged holes and negatively charged electrons must be matched on opposing surfaces of the AlGaN layer [214]. If either a hole or electron gains sufficient energy to move away from its respective surfaces, the associated polarization will reduce causing a decline in available electrons and hence limited overall device performance. The deleterious movement of these charged particles, in turn, arises as a direct consequence of the formation of traps that form at nearly every location between the gate and drain including the surface, bulk, and even adjacent to the gate itself [215]. While improved surface passivation and gate design have largely mitigated the formation of surface and gate traps, recent studies have deduced that defects formed in the bulk AlGaN layer are now a dominant cause of reduced performance [36, 152]. These bulk traps form not as a result of damage from "hot electrons" but rather as an outcome of stress relaxation in general, and specifically, cracking underneath the gate within the AlGaN/GaN layers [216]. Thus, it is the evolution and relaxation of stress in response to the large mechanical loads

induced due to residual, inverse piezoelectric, and thermoelastic effects that govern the rate of device degradation [17].

While previous studies have deduced this cascade of events, the exact conditions inducing relaxation have not been verified. In response, future study may track the evolution of stress in all its components throughout both the GaN and AlGaN layers with continued device operation. Additionally, the level of crystallinity in each layer may be monitored as well in order to observe the formation of defects. By correlating these changes in stress and crystallinity to changes in the electronic performance, the multi-physical nature of the degradation process may be probed directly and future avenues for device improvement illuminated.

6.3 Conclusions

In physical structures, an interconnectedness evolves between the different environments (e.g., thermal, electrical, etc.) as the length and times scales over which devices operate decreases. At this level, energy loses its distinction with respect to its thermal, mechanical, electrical, or chemical origin and instead is transformed into a "total potential" defining the wavefunction of the system as a whole. Analysis particular to, for example, the electrical or thermal response becomes less and less relevant as the problem ceases to be defined by any one of these categories but instead by the *electro-thermal* interaction. In GaN systems for example, these types of interactions are especially pertinent at even continuum length scales due to the strong piezoelectric response of the material in which each of the regimes - thermal, mechanical, and electrical - becomes powerfully coupled in a multi-physical feedback loop. This loop, in large part, determines the capability of the device and, as such, requires that the coupled nature be thoroughly

observed, characterized, and eventually, understood. This study, through movement away from the singular "silos" of analysis towards a more "interconnected" approach (see Figure 52), has attempted to achieve just this.

The very nature of a semiconductor material lends itself to an interconnected approach due to the solid state characteristics of the lattice from which the material is ordered. In these types of materials, the lattice may be thought of as a series of "balls and springs" interweaved within a three dimensional network. At any finite energy, these balls (atoms) vibrate with respect to one another at a frequency governed by the behavior of the springs between them. The springs (interatomic potential), in turn, are modified with any change in their displacement and thus any variation of the atom's position relative to another. As a consequence, with an alteration in the atomic position comes an associated dispersion in the frequency of the vibration (phonon). Analyzing these vibrations then provides insight into those causes affecting the displacement of the atoms.

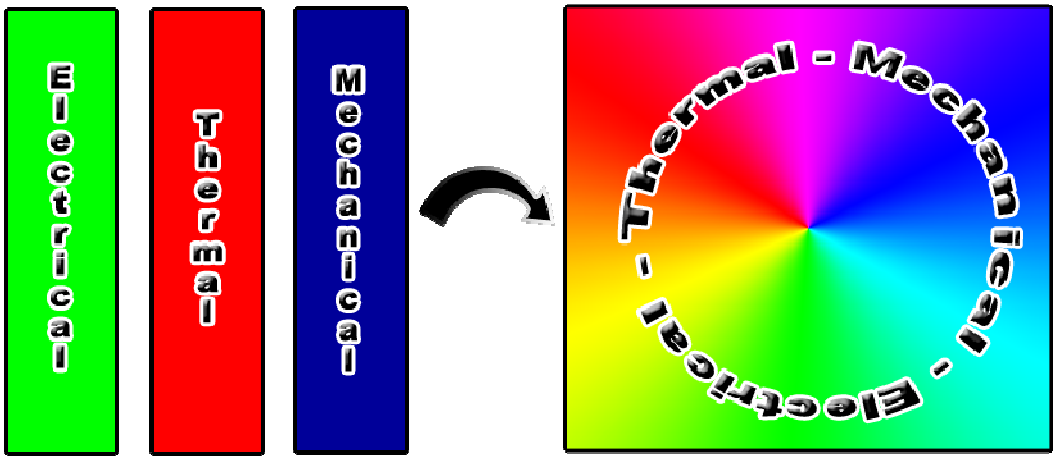

Figure 52. As devices become more coupled in their response, characterization must move from individual "silo" investigations of the environments in isolation (left) towards a more integrated examination of the device in its totality (right).

Likewise, the scattering of light off of this lattice is dependent upon the atomic arrangement, and hence vibration as well [58]. Therefore, analysis of light scattering, as occurs during Raman spectroscopy, allows for the atomic displacement, and in turn its physical causation, to be "seen" and subsequently quantified.

Specifically, these atomic displacements arise due to any strain that occurs in the material. In a GaN device, strain arises from sources spanning the range of the physical spectrum - thermal, electrical, and mechanical – through thermal expansion, piezoelectric, and elastic effects, respectively. Thus each of these physical environments, so coupled in a GaN device, are probed through the scattering of light in a Raman investigation. This fact is both a complication and an opportunity.

Previous Raman investigations of GaN systems have largely ignored this physical coupling by focusing on a lone parameter. Stress measurements were performed apart from both thermal and electrical effects. Similarly, temperature measurements most often were acquired using only the peak position without regard to the coupled nature of this spectral artifact. As a consequence, characterization has continually occurred in exclusive silos rather than from a coupled isometric perspective.

This study moves the characterization of a coupled system from a singular viewpoint to one that capitalizes, rather than being crippled, on the distinctly "flat" response. By tracing each component of the Raman spectrum back to its physical origin, the entirety of the intermixed signal may be deconvoluted and utilized. In such a manner, much of the multi-physical loop determining the capability of the GaN device is then illuminated. Temperature may be measured in the presence of stress. Stress may be investigated in the presence of elevated temperatures as well as electrical effects. Even the role of

electrical carriers on the transport of heat may now be seen, completing, however primitively, an experimentally derived glimpse of the 3-D thermo-electro-mechanical coupled loop at play in GaN materials. Additionally, it is hoped that this analysis, in approach as much as method, has provided a glimpse at the further "flattening" of characterization, and subsequently design, necessary as technology runs headlong towards the room, no doubt, still aplenty at the bottom [217].

APPENDIX

RAMAN SELECTION RULES FOR HEXAGONAL GAN

In Chapter 4, measurement of the E_1(LO) and A_1(TO) phonon lifetimes required the Raman analysis to take place in such a manner that the incident light was parallel to the non-polar *a* axis. The previous measurements of Chapter 2 and 3, however, employed a more common backscattering arrangement in which the probing radiation remained parallel to the polar *c* axis in order to monitor the E_2^{High} phonon mode. The necessity of turning the crystal "on edge" in order to observe certain modes arises as a consequence of the selection rules governing the Raman process. A short discussion of these rules in GaN materials is then pertinent.

The selection rules governing the Raman signal are determined by the vibratory aspects of the material being analyzed. In the hexagonal GaN examined in this study, group theory predicts 6 Raman active optical modes: A_1(LO), A_1(TO), E_1(LO), E_1(TO), E_2^{High}, and E_2^{Low} [150]. Of these modes, those delineated with the letter A, or "axial," have atomic displacements parallel to the c-axis while, in contrast, all of the other modes have atomic movements within the basal plane. The nature of this displacement is critical as momentum must be conserved in all light scattering processes. Consequently, only phonons propagating in the same plane as the exciting and measured radiation will then be observable. In a typical backscattering measurement where the incident light is parallel to the c-axis, this implies that every mode will be observable except the A_1(TO) and E_1(LO).

Table 7. Raman tensors for hexagonal GaN [218]. Letters within the parentheses correspond to the polarization of the given phonon mode while ⊗ indicates a non-zero element within the tensor.

$A_1(z)$	$E_1(x)$	$E_1(y)$	E_2
$\begin{bmatrix} \otimes & 0 & 0 \\ 0 & \otimes & 0 \\ 0 & 0 & \otimes \end{bmatrix}$	$\begin{bmatrix} 0 & 0 & \otimes \\ 0 & 0 & 0 \\ \otimes & 0 & 0 \end{bmatrix}$	$\begin{bmatrix} 0 & 0 & 0 \\ 0 & 0 & \otimes \\ 0 & \otimes & 0 \end{bmatrix}$	$\begin{bmatrix} \otimes & \otimes & 0 \\ \otimes & \otimes & 0 \\ 0 & 0 & 0 \end{bmatrix}$

Momentum conservation, however, is not the only condition determining the visibility of a particular Raman mode. It is also necessary that the polarizability of a mode be capable of changing as a consequence of the incident electromagnetic field (see Equation (3) and (5)). This criterion is analytically described through the relation linking the scattering efficiency, *S*, to the experimental arrangement:

$$S \propto \left| e_L \cdot R \cdot e_S \right| \qquad (.41)$$

where *R* is the mode specific Raman tensor describing the ability of the polarizability to change, and e_L and e_S are the polarizability vectors of the incident and scattered radiation, respectively [219]. Using this proportionality and the Raman tensors described in Table 7, the selection rules are defined in Table 8 for GaN. As the z direction is defined to be oriented parallel to the c-axis, notice that only the A_1(LO) and E_2 modes are visible in a normal backscattering arrangement. It is then necessary to turn the crystal on edge to observe the additional Raman active phonon modes.

Table 8. Raman selection rules for hexagonal GaN using Porto notation to describe the propagating direction and polarization of the incident and scattered radiation.

$z(x,x)\bar{z}$	$z(x,y)\bar{z}$	$x(z,z)\bar{x}$	$x(y,y)\bar{x}$	$x(z,y)\bar{x}$	$x(y,z)\bar{y}$
A_1(LO), E_2	E_2	A_1(TO)	A_1(TO), E_2	E_1(TO)	E_1(LO), E_1(TO)

REFRERENCES

[1] T. Friedman, *The World is Flat: A Brief History of the Twenty-First Century*, 3.0 ed., New York, NY: Picador, 2007.

[2] S. Elhamri, A. Saxler, W. C. Mitchel *et al.*, "Study of deleterious aging effects in GaN/AlGaN heterostructures," *Journal of Applied Physics,* vol. 93, no. 2, pp. 1079, 2003.

[3] K. Gurnett, and T. Adams, "Considerations for GaN-powered base stations," *III-Vs Review* vol. 19, no. 7, pp. 20-22, 2006.

[4] Widgap, *D4 Roadmap for wide bandgap semiconductors*, vol. 3, 2007.

[5] J. Moon, J. Kim, I. Kim *et al.*, "GaN HEMT based Doherty amplifier for 3.5-GHz WiMAX Applications," in Microwave Integrated Circuit Conference, 20007. EuMIC 2007. European, 2007, pp. 395-398.

[6] L. Kim, G. W. Lee, W. J. Hwang *et al.*, "Thermal analysis and design of GaN-based LEDs for high power applications," *physica status solidi(c),* vol. 0, no. 7, pp. 2261-2264, 2003.

[7] J. Shealy, J. Smart, M. Poulton *et al.*, "Gallium nitride (GaN) HEMT's: progress and potential for commercial applications." p. 243.

[8] M. Higashiwaki, T. Matsui, and T. Mimura, "AlGaN/GaN MIS-HFETs with f/sub T/ of 163 GHz using cat-CVD SiN gate-insulating and passivation Layers," *Electron Device Letters, IEEE,* vol. 27, no. 1, pp. 16-18, 2006.

[9] S. Saygi, H. Fatima, X. He *et al.*, "Performance stability of high-power III-nitride metal-oxide semiconductor-heterostructure field-effect transistors," *physica status solidi (c),* vol. 2, no. 7, pp. 2651-2654, 2005.

[10] M. Kuball, M. J. Uren, and T. Martin, " Reliability optimization for wide bandgap devices: Recent developments in high-spatial resolution thermal imaging of GaN devices." pp. 246 - 247

[11] Y. C. Chou, D. Leung, I. Smorchkova *et al.*, "Degradation of AlGaN/GaN HEMTs under elevated temperature lifetesting," *Microelectronics and Reliability,* vol. 44, no. 7, pp. 1033-1038, 2004.

[12] C. Lee, L. Witkowski, H. Q. Tserng *et al.*, "Effects of AlGaN/GaN HEMT structure on RF reliability," *Electronics Letters,* vol. 41, no. 3, pp. 155-157, 2005.

[13] S. S. H. Hsu, P. Valizadeh, D. Pavlidis *et al.*, "Impact of RF stress on dispersion and power characteristics of AlGaN/GaN HEMTs." pp. 85-88.

[14] C. Lee, L. Witkowski, M. Muir *et al.*, "Reliability evaluation of AlGaN/GaN HEMTs grown on SiC substrate." pp. 436-442.

[15] W. Liu, M. F. Li, Z. C. Feng *et al.*, "Material properties of GaN grown by MOCVD," *Surface and Interface Analysis,* vol. 28, no. 1, pp. 150-154, 1999.

[16] I. Daumiller, C. Kirchner, M. Kamp *et al.*, "Evaluation of the temperature stability of AlGaN/GaN heterostructure FETs," *Electron Device Letters, IEEE,* vol. 20, no. 9, pp. 448, 1999.

[17] J. Joh, and J. d. Alamo, "Effects of Temperature on electrical degradation of GaN high electron mobility transistors," in 7th International Conference on Nitride Semiconductors, Las Vegas, NV, 2007.

[18] H. Kim, V. Tilak, B. M. Green *et al.*, "Reliability Evaluation of High Power AlGaN/GaN HEMTs on SiC Substrate," *physica status solidi(a),* vol. 188, no. 1, pp. 203-206, 2001.

[19] S. Singhal, T. Li, A. Chaudhari *et al.*, "Reliability of large periphery GaN-on-Si HFETs," *Microelectronics Reliability,* vol. 46, pp. 1247–1253, 2006.

[20] R. Vetury, J. B. Shealy, D. S. Green *et al.*, "Performance and RF Reliability of GaN-on-SiC HEMT's using Dual-Gate Architectures." p. 714.

[21] Y. Zhu, and H. D. Espinosa, "Reliability of capacitive RF MEMS switches at high and low temperatures," *International Journal of RF and Microwave Computer-Aided Engineering,* vol. 14, no. 4, pp. 317-328, 2004.

[22] P. Burgaud, L. Constancias, G. Martel *et al.*, "Preliminary reliability assessment and failure physical analysis on AlGaN/GaN HEMTs COTS," *Microelectronics Reliability,* vol. 47, no. 9-11, pp. 1653-1657, 2007.

[23] F. Bernardini, V. Fiorentini, and D. Vanderbilt, "Spontaneous polarization and piezoelectric constants of III-V nitrides," *Physical Review B,* vol. 56, no. 16, pp. R10024, 1997.

[24] H. Morkoc, and L. Liu, "GaN-Based Modulation-Doped FETs and Heterojunctin Bipolar Transistors," *Nitride Semiconductors: Handbook on Materials and Devices*, P. Ruterana, M. Albrecht and J. Neugebauer, eds., pp. 547-626, Weinheim: Wiley, 2003.

[25] O. Ambacher, B. Foutz, J. Smart *et al.*, "Two dimensional electron gases induced by spontaneous and piezoelectric polarization in undoped and doped AlGaN/GaN heterostructures," *Journal of Applied Physics,* vol. 87, no. 1, pp. 334-344, 2000.

[26] Y. F. Wu, B. P. Keller, P. Fini *et al.*, "High Al-content AlGaN/GaN MODFETs for ultrahigh performance," *Electron Device Letters, IEEE,* vol. 19, no. 2, pp. 50-53, 1998.

[27] Y. F. Wu, S. Keller, P. Kozodoy *et al.*, "Bias dependent microwave performance of AlGaN/GaN MODFET's up to 100 V," *Electron Device Letters, IEEE,* vol. 18, no. 6, pp. 290-292, 1997.

[28] In class-A amplification operation, the maximum power of the HEMT is defined by P-max=Imax(Vb-Vkn)/8 where Imax is the maximum "On" current, Vb the beakdown voltage, and Vkn the knee voltage.

[29] A. Asgari, M. Kalafi, and L. Faraone, "A quasi-two-dimensional charge transport model of AlGaN/GaN high electron mobility transistors (HEMTs)," *Physica E: Low-dimensional Systems and Nanostructures,* vol. 28, no. 4, pp. 491-499, 2005.

[30] T.-H. Yu, and K. F. Brennan, "Theoretical study of a GaN-AlGaN high electron mobility transistor including a nonlinear polarization model," *Electron Devices, IEEE Transactions on,* vol. 50, no. 2, pp. 315-323, 2003.

[31] O. Ambacher, J. Smart, J. R. Shealy *et al.*, "Two-dimensional electron gases induced by spontaneous and piezoelectric polarization charges in N- and Ga-face AlGaN/GaN heterostructures," *Journal of Applied Physics,* vol. 85, no. 6, pp. 3222-3233, 1999.

[32] V. Fiorentini, F. Bernardini, and O. Ambacher, "Evidence for nonlinear macroscopic polarization in III--V nitride alloy heterostructures," *Applied Physics Letters,* vol. 80, no. 7, pp. 1204-1206, 2002.

[33] Y. Chang, K. Y. Tong, and C. Surya, "Numerical simulation of current–voltage characteristics of AlGaN/GaN HEMTs at high temperatures," *Semiconductor Science and Technology*, no. 2, pp. 188, 2005.

[34] A. Koudymov, M. S. Shu, G. Simin *et al.*, "Current collapse and reliability of III-N heterostructure field effect transistors," *physica status solidi (RRL) - Rapid Research Letters,* vol. 1, no. 3, pp. 116-118, 2007.

[35] D. Gotthold, S. Guo, R. Birkhahn *et al.*, "Time-dependent degradation of AlGaN/GaN heterostructures grown on silicon carbide," *Journal of Electronic Materials,* vol. 33, no. 5, pp. 408-411, 2004.

[36] J. Joh, and J. A. del Alamo, "Mechanisms for Electrical Degradation of GaN High-Electron Mobility Transistors." pp. 1-4.

[37] D. L. Blackburn, "Temperature measurements of semiconductor devices-a review," *Semiconductor Thermal Measurement and Management Symposium, 2004. Twentieth Annual IEEE*, pp. 70-80, 2004.

[38] J. Park, M. W. Shin, and C. C. Lee, "Thermal Modeling and Measurement of GaN-Based HFET Devices," *IEEE ELECTRON DEVICE LETTERS,* vol. 24, no. 7, 424-426, 2004.

[39] J. Lee, T. Beechem, T. L. Wright *et al.*, "Electrical, Thermal, and Mechanical Characterization of Silicon Microcantilever-Heaters," *Journal of Microelectromechanical Systems,* vol. 15, pp. 1644-1655, 2006.

[40] R. Aubry, J.-C. Jacquet, J. Weaver *et al.*, "SThM Temperature Mapping and Nonlinear Thermal Resistance Evolution With Bias on AlGaN/GaN HEMT Devices," *Electron Devices, IEEE Transactions on,* vol. 54, no. 3, pp. 385-390, 2007.

[41] J. G. Felbinger, M. V. S. Chandra, S. Yunju *et al.*, "Comparison of GaN HEMTs on Diamond and SiC Substrates," *Electron Device Letters, IEEE,* vol. 28, no. 11, pp. 948-950, 2007.

[42] A. V. Vertiatchikh, L. F. Eastman, W. J. Schaff *et al.*, "Effect of surface passivation of AlGaN/GaN heterostructure field-effect transistor," *Electronics Letters,* vol. 38, no. 8, pp. 388-389, 2002.

[43] A. Majumdar, "Scanning thermal microscopy," *Annual Review of Materials Science,* vol. 29, no. 1, pp. 505-585, 1999.

[44] J. Kuzmik, R. Javorka, A. Alam *et al.*, "Determination of channel temperature in AlGaN/GaN HEMTs grown on sapphire and silicon substrates using DC characterization method," *Electron Devices, IEEE Transactions on,* vol. 49, no. 8, pp. 1496-1498, 2002.

[45] S. P. McAlister, J. A. Bardwell, S. Haffouz *et al.*, "Self-heating and the temperature dependence of the dc characteristics of GaN heterostructure field effect transistors," *Journal of Vacuum Science & Technology A: Vacuum, Surfaces, and Films,* vol. 24, pp. 624-628, 2006.

[46] Z. Zhang, "Surface Temperature Measurement Using Optical Techniques," *Annual Review of Heat Transfer,* vol. 11, pp. 351-411, 2000.

[47] A. N. Smith, and P. M. Norris, "Microscale Heat Transfer," *Handbook of Heat Transfer*, A. Bejan and A. Krauss, eds., pp. 1309-1358: John Wiley & Sons, Inc., 2003.

[48] P. W. Webb, "Thermal imaging of electronic devices with low surface emissivity," *Circuits, Devices and Systems, IEE Proceedings G,* vol. 138, no. 3, pp. 390, 1991.

[49] H. Hirori, T. Tachizaki, O. Matsuda *et al.*, "Electron dynamics in chromium probed with 20-fs optical pulses," *Physical Review B,* vol. 68, no. 11, pp. 113102, 2003.

[50] A. Sarua, J. Hangfeng, M. Kuball *et al.*, "Integrated micro-Raman/infrared thermography probe for monitoring of self-heating in AlGaN/GaN transistor structures," *Electron Devices, IEEE Transactions on,* vol. 53, no. 10, pp. 2438-2447, 2006.

[51] W. Claeys, S. Dilhaire, S. Jorez *et al.*, "Laser probes for the thermal and thermomechanical characterisation of microelectronic devices," *Microelectronics Journal,* vol. 32, no. 10, pp. 891-898, 2001.

[52] D. S. Green, B. Vembu, D. Hepper *et al.*, "GaN HEMT thermal behavior and implications for reliability testing and analysis," *Physica status solidi (c),* vol. 5, no. 6, pp. 2026-2029, 2008.

[53] I. Ahmad, V. Kasisomayajula, M. Holtz *et al.*, "Self-heating study of an AlGaN/GaN-based heterostructure field-effect transistor using ultraviolet micro-Raman scattering," *Applied Physics Letters,* vol. 86, pp. 173503, 2005.

[54] M. Kuball, J. M. Hayes, M. J. Uren *et al.*, "Measurement of temperature in active highpower AlGaN/GaN HFET's using Raman spectroscopy," *IEEE Electron Device Letters,* vol. 23, pp. 7-9, 2002.

[55] B. Bhushan, *Springer Handbook of Nanotechnology*, New York: Springer, 2004.

[56] I. Ahmad, M. Holtz, N. N. Faleev *et al.*, "Dependence of the stress--temperature coefficient on dislocation density in epitaxial GaN grown on alpha-Al[sub 2]O[sub 3] and 6H--SiC substrates," *Journal of Applied Physics,* vol. 95, no. 4, pp. 1692-1697, 2004.

[57] A. Torabi, W. E. Hoke, J. J. Mosca *et al.*, "Influence of AlN nucleation layer on the epitaxy of GaN/AlGaN high electron mobility transistor structure and wafer curvature," *Journal of Vacuum Science & Technology B: Microelectronics and Nanometer Structures,* vol. 23, pp. 1194-1198, 2005.

[58] C. Kittel, *Introduction to Solid State Physics*, 8th ed., Hoboken, NJ: Wiley, 2005.

[59] V. Y. Davydov, N. S. Averkiev, I. N. Goncharuk *et al.*, "Raman and photoluminescence studies of biaxial strain in GaN epitaxial layers grown on 6H--SiC," *Journal of Applied Physics,* vol. 82, no. 10, pp. 5097, 1997.

[60] C. Kisielowski, J. Kruger, S. Ruvimov *et al.*, "Strain-related phenomena in GaN films," *Physical Review B,* vol. 54, no. 24, pp. 17745, 1996.

[61] P. Puech, F. Demagenot, J. Frandon *et al.*, "GaN nanoindentation: A micro-Raman spectroscopy study of local strain fields," *Journal of Applied Physics,* vol. 96, no. 5, pp. 2853, 2004.

[62] S. Tripathy, S. J. Chua, P. Chen *et al.*, "Micro-Raman investigation of strain in GaN and Al xGa1- xN/GaN heterostructures grown on SiN (1110)," *Journal of Applied Physics,* vol. 92, no. 7, pp. 3503-3510, 2002.

[63] R. Aubry, C. Dua, J. C. Jacquet *et al.*, "Temperature measurement in AlGaN/GaN High-Electron-Mobility Transistors using micro-Raman scattering spectroscopy," *Eur. Phys. J. Appl. Phys,* vol. 30, pp. 77-82, 2005.

[64] F. Bertram, T. Riemann, J. Christen *et al.*, "Strain relaxation and strong impurity incorporation in epitaxial laterally overgrown GaN: Direct imaging of different growth domains by cathodoluminescence microscopy and micro-Raman spectroscopy," *Applied Physics Letters,* vol. 74, no. 3, pp. 359, 1999.

[65] M. Holtz, M. Seon, T. Prokofyeva *et al.*, "Micro-Raman imaging of GaN hexagonal island structures," *Applied Physics Letters,* vol. 75, no. 12, pp. 1757, 1999.

[66] T. Kozawa, T. Kachi, H. Kano *et al.*, "Thermal stress in GaN epitaxial layers grown on sapphire substrates," *Journal of Applied Physics,* vol. 77, no. 9, pp. 4389, 1995.

[67] M. Kuball, S. Rajasingam, A. Sarua *et al.*, "Measurement of temperature distribution in multifinger AlGaN/GaN heterostructure field-effect transistors using micro-Raman spectroscopy," *Applied Physics Letters,* vol. 82, pp. 124, 2002.

[68] J. Pomeroy, M. Kuball, D. Wallis *et al.*, "Thermal mapping of defects in AlGaN/GaN heterostructure field-effect transistors using micro-Raman spectroscopy," *Applied Physics Letters,* vol. 87, pp. 103508, 2005.

[69] S. Rajasingam, A. Sarua, M. Kuball *et al.*, "High-temperature annealing of AlGaN: Stress, structural,and compositional changes," *Journal of Applied Physics,* vol. 94, no. 10, pp. 6366-6371, 2003.

[70] R. Loudon, "The Raman effect in crystals," *Advances in Physics,* vol. 13, no. 52, pp. 423, 1964.

[71] D. A. Long, *Raman Spectroscopy*: McGraw-Hill, 1977.

[72] G. Chen, *Nanoscale Energy Transport and Conversion*, New York, NY: Oxford University Press, 2005.

[73] M. Balkanski, R. F. Wallis, and E. Haro, "Anharmonic effects in light scattering due to optical phonons in silicon," *Physical Review B,* vol. 28, no. 4, pp. 1928, 1983.

[74] T. R. Hart, R. L. Aggarwal, and B. Lax, "Temperature Dependence of Raman Scattering in Silicon," *Physical Review B,* vol. 1, no. 2, pp. 638, 1970.

[75] R. Tsu, and J. G. Hernandez, "Temperature dependence of silicon Raman lines," *Applied Physics Letters,* vol. 41, no. 11, pp. 1016-1018, 1982.

[76] S. Todoroki, M. Sawai, and K. Aiki, "Temperature distribution along the striped active region in high-power GaAlAs visible lasers," *Journal of Applied Physics,* vol. 58, pp. 1124, 1985.

[77] T. Beechem, A. Christensen, S. Graham *et al.*, "Micro-Raman thermometry in the presence of complex stresses in GaN devices," *Journal of Applied Physics,* vol. 103, no. 12, pp. 124501, 2008.

[78] M. R. Abel, S. Graham, J. R. Serrano *et al.*, "Raman Thermometry of Polysilicon Microelectro-mechanical Systems in the Presence of an Evolving Stress," *Journal of Heat Transfer,* vol. 129, pp. 329, 2007.

[79] A. Sarua, J. Hangfeng, K. P. Hilton *et al.*, "Thermal Boundary Resistance Between GaN and Substrate in AlGaN/GaN Electronic Devices," *Electron Devices, IEEE Transactions on,* vol. 54, no. 12, pp. 3152-3158, 2007.

[80] G. Lucazeau, "Effect of pressure and temperature on Raman spectra of solids: anharmonicity," *Journal of Raman Spectroscopy,* vol. 34, pp. 478-496, 2003.

[81] T. Beechem, S. Graham, S. P. Kearney *et al.*, "Invited Article: Simultaneous mapping of temperature and stress in microdevices using micro-Raman spectroscopy," *Review of Scientific Instruments,* vol. 78, no. 6, pp. 061301-9, 2007.

[82] J. Kim, J. A. Freitas, J. Mittereder *et al.*, "Effective temperature measurements of AlGaN/GaN-based HEMT under various load lines using micro-Raman technique," *Solid State Electronics,* vol. 50, no. 3, pp. 408-411, 2006.

[83] M. Kuball, J. W. Pomeroy, S. Rajasingam *et al.*, "High spatial resolution micro-Raman temperature measurements of nitride devices(FETs and light emitters)," *Physica Status Solidi(a),* vol. 202, no. 5, pp. 824-831, 2005.

[84] Y. Ohno, M. Akita, S. Kishimoto *et al.*, "Temperature Distribution Measurement in AlGaN/GaN High-Electron-Mobility Transistors by Micro-Raman Scattering Spectroscopy," *Jpn. J. Appl. Phys., Part,* vol. 2, pp. 41, 2002.

[85] Y. Ohno, M. Akito, S. Kishimotoa *et al.*, "Temperature distribution in AlGaN/GaN HEMT's measured by micro-Raman Scattering Spectroscopy," *physica status solidi(c),* vol. 0, no. 1, pp. 57-60, 2002.

[86] S. Rajasingam, J. W. Pomeroy, M. Kuball *et al.*, "Micro-Raman temperature measurements for electric field assessment in active AlGaN-GaN HFETs," *Electron Device Letters, IEEE,* vol. 25, no. 7, pp. 456-458, 2004.

[87] I. Ahmad, V. Kasisomayajula, D. Y. Song *et al.*, "Self-heating in a GaN based heterostructure field effect transistor: Ultraviolet and visible Raman measurements and simulations," *Journal of Applied Physics,* vol. 100, pp. 113718, 2006.

[88] H. Ji, M. Kuball, A. Sarua *et al.*, "Three-dimensional thermal analysis of a flip-chip mounted AlGaN/GaN HFET using confocal micro-Raman spectroscopy," *Electron Devices, IEEE Transactions on,* vol. 53, no. 10, pp. 2658-2661, 2006.

[89] M. Kuball, G. J. Riedel, J. W. Pomeroy *et al.*, "Time-Resolved Temperature Measurement of AlGaN/GaN Electronic Devices Using Micro-Raman Spectroscopy," *Electron Device Letters, IEEE,* vol. 28, no. 2, pp. 86-89, 2007.

[90] G. J. Riedel, J. W. Pomeroy, K. P. Hilton *et al.*, "Nanosecond Timescale Thermal Dynamics of AlGaN/GaN Electronic Devices," *Electron Device Letters, IEEE,* vol. 29, no. 5, pp. 416-418, 2008.

[91] R. J. T. Simms, J. W. Pomeroy, M. J. Uren *et al.*, "Channel Temperature Determination in High-Power AlGaN/GaN HFETs Using Electrical Methods and Raman Spectroscopy," *Electron Devices, IEEE Transactions on,* vol. 55, no. 2, pp. 478-482, 2008.

[92] B. Di Bartolo, *Optical Interactions in Solids*, New York: John Wiley & Sons 1968.

[93] L. Bergman, D. Alexson, P. Murphy *et al.*, "Raman analysis of phonon lifetimes in AlN and GaN of wurtzite structure," *Physical Review B,* vol. 59, no. 20, pp. 12977-12982, 1999.

[94] T. Beechem, and S. Graham, "Temperature and doping dependence of phonon lifetimes and decay pathways in GaN," *Journal of Applied Physics,* vol. 103, no. 9, pp. 093507, 2008.

[95] W. S. Li, Z. X. Shen, Z. C. Feng *et al.*, "Raman scattering and transverse effective charge of MOCVD-grown GaN films between 78 and 870 K," *Surface and Interface Analysis,* vol. 28, no. 1, pp. 173-176, 1999.

[96] D. Y. Song, S. A. Nikishin, M. Holtz *et al.*, "Decay of zone-center phonons in GaN with A[sub 1], E[sub 1], and E[sub 2] symmetries," *Journal of Applied Physics,* vol. 101, no. 5, pp. 053535, 2007.

[97] S. Ganesan, A. Maradudin, and J. Oitmaa, "A Lattice Theory of Morphic Effects in Crystals of the Diamond Structure," *Annals of Physics,* vol. 56, pp. 556-594, 1970.

[98] S. Tripathy, S. Chua, and A. Ramam, "Electronic and vibronic properties of n-type GaN: the influence of etching and annealing," *Journal of Physics: Condensed Matter,* vol. 14, pp. 4461-4476, 2002.

[99] S. C. Hsu, B. J. Pong, W. H. Li *et al.*, "Stress relaxation in GaN by transfer bonding on Si substrates," *Applied Physics Letters,* vol. 91, no. 25, pp. 251114, 2007.

[100] W. Rieger, T. Metzger, H. Angerer *et al.*, "Influence of substrate-induced biaxial compressive stress on the optical properties of thin GaN films," *Applied Physics Letters,* vol. 68, no. 7, pp. 970, 1996.

[101] H. J. Park, C. Park, S. Yeo *et al.*, "Epitaxial strain energy measurements of GaN on sapphire by Raman spectroscopy," *phys. stat. sol. (c),* vol. 2, no. 7, pp. 2446–2449, 2005.

[102] A. Sarua, J. Hangfeng, M. Kuball *et al.*, "Piezoelectric strain in AlGaN/GaN heterostructure field-effect transistors under bias," *Applied Physics Letters,* vol. 88, no. 10, pp. 103502, 2006.

[103] T. Beechem, and S. Graham, "Temperature Measurement of Microdevices using Thermoreflectance and Raman Thermometry," *BioNanoFluidic MEMS*, P. Hesketh, ed., p. 375: Springer, 2007.

[104] J. Kim, J. A. Freitas Jr, P. B. Klein *et al.*, "The Effect of Thermally Induced Stress on Device Temperature Measurements by Raman Spectroscopy," *Electrochemical and Solid-State Letters,* vol. 8, pp. G345, 2005.

[105] H. Harima, T. Hosoda, and S. Nakashima, "Temperature Measurement in a Silicon Carbide Light Emitting Diode by Raman Scattering," *Journal of Electronic Materials,* vol. 28, no. 3, pp. 141-143, 1999.

[106] T. Beechem, S. Graham, S. Kearney *et al.*, "Simultaneous Mapping of Temperature and Stress in Microdevices Using Micro-Raman Spectroscopy," *Review of Scientific Instruments,* vol. 78, no. 5, 2007.

[107] A. Sarua, M. Kuball, and J. E. V. Nostrand, "Phonon deformation potentials of the E2ÑhighÖ phonon mode of Al xGa1− xN," *APPLIED PHYSICS LETTERS,* vol. 85, no. 12, pp. 2217-2219, 2004.

[108] G. Burns, F. Dacol, J. C. Marinace *et al.*, "Raman scattering in thin-film waveguides," *Applied Physics Letters,* vol. 22, no. 8, pp. 356, 1973.

[109] G. Abstreiter, "Micro-Raman Spectroscopy for Characterization of Semiconductor Devices," *Applied Surface Science,* vol. 50, pp. 73-78, 1991.

[110] F. LaPlant, G. Laurence, and D. Ben-Amotz, "Theoretical and Experimental Uncertainty in Temperature Measurement of Materials by Raman Spectroscopy," *Applied Spectroscopy,* vol. 50, pp. 1034, 1996.

[111] J. D. Brown, S. Gibb, J. McKenna *et al.*, "Performance, Reliability, and Manufacturability of AlGaN/GaN High Electron Mobility Transistors on Silicon Carbide Substrates," *ECS Transactions,* vol. 3, no. 5, pp. 161-179, 2006.

[112] J. D. Brown, S. Lee, D. Lieu *et al.*, "Voltage Dependent Characteristics of 48V AlGaN/GaN High Electron Mobility Transistor Technology on Silicon Carbide." p. 303.

[113] Daniel C. Harris, and M. D. Bertolucci, *Symmetry and Spectroscopy*: Courier Dover Publications, 1989.

[114] J. R. Serrano, L. M. Phinney, and S. P. Kearney, "Micro-Raman thermometry of thermal flexure actuators," *Journal of Micromechanics and Microengineering,* vol. 16, no. 7, pp. 1128-1134, 2006.

[115] J. M. Wagner, and F. Bechstedt, "Phonon deformation potentials of alpha-GaN and -AlN: An ab initio calculation," *Applied Physics Letters,* vol. 77, no. 3, pp. 346-348, 2000.

[116] The ANSYS model was developed and implemented by fellow member of the Electronics Manufacturing and Reliability Laboratory, Adam Christensen.

[117] A. Christensen, "Thermal Transport in III-V Semiconductors and Devices," Mechanical Engineering, Georgia Institute of Technology, Atlanta, 2006.

[118] A. Jezowski, B. A. Danilchenko, M. Bockowski *et al.*, "Thermal conductivity of GaN crystals in 4.2-300 K range," *Solid State Communications,* vol. 128, no. 2-3, pp. 69-73, 2003.

[119] B. W. Olson, S. Graham, and K. Chen, "A practical extension of the 3 omega method to multilayer structures," *Review of Scientific Instruments,* vol. 76, no. 5, pp. 053901, 2005.

[120] O. Nilsson, H. Mehling, R. Horn *et al.*, "Determination of the thermal diffusivity and conductivity of monocrystalline silicon carbide (300-2300 K)," *High Temperatures High Pressures,* vol. 29, no. 1, pp. 73-79, 1997.

[121] Y. D. Kim, N. L. Oh, S. T. Oh *et al.*, "Thermal conductivity of W-Cu composites at various temperatures," *Materials Letters,* vol. 51, no. 5, pp. 420, 2001.

[122] F. Bernardini, and V. Fiorentini, "First-principles calculation of the piezoelectric tensor d-tensor of III--V nitrides," *Applied Physics Letters,* vol. 80, no. 22, pp. 4145, 2002.

[123] J. F. Nye, *Physical Properties of Crystals: Their Represenation by Tensors and Matrices*: Oxford at the Clarendon Press, 1979.

[124] S. J. Kline, and F. A. McClintock, "Describing uncertainties in single sample experiments," *Mechanical Engineering,* vol. 75, pp. 3-8, 1953.

[125] J. P. Holman, *Experimental Methods for Engineers*, 7th ed., 2001.

[126] S. P. Kearney, L. M. Phinney, and M. S. Baker, "Spatially Resolved Temperature Mapping of Electrothermal Actuators by Surface Raman Scattering," *Microelectromechanical Systems, Journal of,* vol. 15, no. 2, pp. 314-321, 2006.

[127] D. M. Lipkin, and D. R. Clarke, "Sample-probe interactions in spectroscopy: Sampling microscopic property gradients," *Journal of Applied Physics,* vol. 77, no. 5, pp. 1855-1863, 1995.

[128] A. F. M. Anwar, R. T. Webster, and K. V. Smith, "Bias induced strain in AlGaN/GaN heterojunction field effect transistors and its implications," *Applied Physics Letters,* vol. 88, no. 20, pp. 203510, 2006.

[129] B. Jogai, J. D. Albrecht, and E. Pan, "Effect of electromechanical coupling on the strain in AlGaN/GaN heterojunction field effect transistors," *Journal of Applied Physics,* vol. 94, no. 6, pp. 3984-3989, 2003.

[130] E. Anastassakis, A. Pinczuk, E. Burstein *et al.*, "Effect of static uniaxial stress on the Raman spectrum of silicon," *Solid State Communications,* vol. 8, no. 2, pp. 133, 1970.

[131] I. De Wolf, "Micro-Raman spectroscopy to study local mechanical stress in silicon integrated circuits," *Semiconductor Science and Technology*, no. 2, pp. 139, 1996.

[132] W. Zhu, J. Zhu, S. Nishino *et al.*, "Spatially resolved Raman spectroscopy evaluation of residual stresses in 3C-SiC layer deposited on Si substrates with different crystallographic orientations," *Applied Surface Science,* vol. 252, no. 6, pp. 2346-2354, 2006.

[133] T. Beechem, A. Christensen, D. Green *et al.*, "Micro-Raman Thermometry in the Presence of Complex Stresses in GaN Devices," *IEEE Transactions on Electron Devices,* vol. In Review, 2008.

[134] As this is the same model previously mentioned, Adam Christensen must be recognized for his sole effort on the simulation.

[135] M. Abel, and S. Graham, "Thermometry of Polycrystalline Silicon Structures Using Raman Spectroscopy," in ASME InterPACK 2005, San Francisco, CA, 2005, pp. 1-8.

[136] M. Abel, "Thermal Metrology of Polysilicon MEMS Using Raman Spectroscopy," Georgia Institute of Technology, Atlanta, GA, 2005.

[137] M. Abel, T. Wright, E. Sunden *et al.*, "Thermal Metrology of Silicon Microstructures using Raman Spectroscopy," *Proceedings of IEEE Semi-Therm,* vol. 21, pp. 235-242, 2005.

[138] J. W. Pomeroy, M. Kuball, H. Lu *et al.*, "Phonon lifetimes and phonon decay in InN," *Applied Physics Letters,* vol. 86, no. 22, pp. 223501, 2005.

[139] G. Viera, S. Huet, and L. Boufendi, "Crystal size and temperature measurements in nanostructured silicon using Raman spectroscopy," *Journal of Applied Physics,* vol. 90, no. 8, pp. 4175-4183, 2001.

[140] I. De Wolf, "Raman spectroscopy: about chips and stress," *Spectroscopy Europe,* vol. 15, no. 2, pp. 6-13, 2003.

[141] V. Srikar, A. Swan, M. S. Unlu *et al.*, "Micro-Raman Measurement of bending stresses in micromachined silicon flexures," *Journal of Microelectromechanical Systems,* vol. 12, no. 6, pp. 779-787, 2003.

[142] Y. S. Toulokian, and C. Y. Ho, "Thermal Conductivity of Nonmetallic Solid," *Thermophysical Properties of Matter, Eds YS Touloukian and CY Ho, New York: IFI/Pleun), 1972, 2*.

[143] Adam Christensen should be credited for the development and implementation of this model.

[144] R. B. Schwarz, K. Khachaturyan, and E. R. Weber, "Elastic moduli of gallium nitride," *Applied Physics Letters,* vol. 70, no. 9, pp. 1122, 1997.

[145] W. Qian, M. Skowronski, and G. S. Rohrer, "Structural defects and their relationship to nucleation of GaN thin films," *Materials Research Society Symposium - Proceedings.* p. 475.

[146] M. A. Moram, Z. H. Barber, and C. J. Humphreys, "Accurate experimental determination of the Poisson's ratio of GaN using high-resolution x-ray diffraction," *Journal of Applied Physics,* vol. 102, no. 2, pp. 023505, 2007.

[147] M. Yamaguchi, T. Yagi, T. Sota *et al.*, "Brillouin scattering study of bulk GaN," *Journal of Applied Physics,* vol. 85, no. 12, pp. 8502, 1999.

[148] E. L. H. Kern, D.W., H. W. Deem, and H. D. Sheets, "Thermal Properties of Beta Silicon Carbide from 20° to 200°C," *Materials Research Bulletin,* vol. 4, no. 25, 1969.

[149] J. P. Calame, R. E. Myers, S. C. Binari *et al.*, "Experimental investigation of microchannel coolers for the high heat flux thermal management of GaN-on-SiC semiconductor devices," *International Journal of Heat and Mass Transfer,* vol. 50, no. 23-24, pp. 4767, 2007.

[150] H. Harima, “Properties of GaN and related compounds studied by means of Raman scattering,” *Journal of Physics: Condensed Matter*, no. 38, pp. R967, 2002.

[151] R. Nowak, and M. Pessa, “Elastic and plastic properties of GaN determined by nano-indentation of bulk crystal,” *Applied Physics Letters,* vol. 75, no. 14, pp. 2070, 1999.

[152] J. Joh, L. Xia, and J. A. del Alamo, "Gate Current Degradation Mechanisms of GaN High Electron Mobility Transistors." pp. 385-388.

[153] M. Kuball, “Raman spectroscopy of GaN, AlGaN and AlN for process and growth monitoring/control,” *Surface and Interface Analysis,* vol. 31, no. 10, pp. 987-999, 2001.

[154] J. L. Hudgins, G. S. Simin, E. Santi *et al.*, “An assessment of wide bandgap semiconductors for power devices,” *Power Electronics, IEEE Transactions on,* vol. 18, no. 3, pp. 907-914, 2003.

[155] A. Matulionis, J. Liberis, L. Ardaravicius *et al.*, “Hot-phonon lifetime in AlGaN/GaN at a high lattice temperature,” *Semicond. Sci. Technol,* vol. 19, no. 4, pp. S421-S423, 2004.

[156] B. K. Ridley, W. J. Schaff, and L. F. Eastman, “Hot-phonon-induced velocity saturation in GaN,” *Journal of Applied Physics,* vol. 96, no. 3, pp. 1499, 2004.

[157] A. Matulionis, “Hot phonons in GaN channels for HEMTs,” *physica status solidi (a),* vol. 203, no. 10, pp. 2313-2325, 2006.

[158] K. T. Tsen, J. G. Kiang, D. K. Ferry *et al.*, “Subpicosecond time-resolved Raman studies of LO phonons in GaN: Dependence on photoexcited carrier density,” *Applied Physics Letters,* vol. 89, no. 11, pp. 112111-112111, 2006.

[159] M. Kuball, J. M. Hayes, S. Ying *et al.*, “Phonon lifetimes in bulk AlN and their temperature dependence,” *Applied Physics Letters,* vol. 77, no. 13, pp. 1958-1960, 2000.

[160] K. T. Tsen, R. P. Joshi, D. K. Ferry *et al.*, “Nonequilibrium electron distributions and phonon dynamics in wurtzite GaN,” *Applied Physics Letters,* vol. 68, no. 21, pp. 2990-2992, 1996.

[161] A. Matulionis, J. Liberis, I. MatulionienÄ— *et al.*, “Hot-phonon temperature and lifetime in a biased Al_{x}Ga_{1-x}N/GaN channel estimated from noise analysis,” *Physical Review B,* vol. 68, no. 3, pp. 035338, 2003.

[162] Z. C. Feng, “Micro-Raman scattering and microphotoluminescence of GaN thin films grown on sapphire by metal-organic chemical vapor deposition,” *Optical Engineering* vol. 41, no. 8, pp. 2022-2031, 2002.

[163] F. Demangeot, J. Frandon, M. A. Renucci *et al.*, "Interplay of electrons and phonons in heavily doped GaN epilayers," *Journal of Applied Physics,* vol. 82, pp. 1305, 1997.

[164] C. J. Eiting, P. A. Grudowski, and R. D. Dupuis, "Growth of low resistivity p-type GaN by metal organic chemicalvapour deposition," *Electronics Letters,* vol. 33, no. 23, pp. 1987-1989, 1997.

[165] K. Shiojima, J. M. Woodall, C. J. Eiting *et al.*, "Effect of defect density on the electrical characteristics of n-type GaN Schottky contacts," *Journal of Vacuum Science & Technology B: Microelectronics and Nanometer Structures,* vol. 17, pp. 2030, 1999.

[166] J. C. Carrano, T. Li, P. A. Grudowski *et al.*, "Comprehensive characterization of metal–semiconductor–metal ultraviolet photodetectors fabricated on single-crystal GaN," *Journal of Applied Physics,* vol. 83, no. 11, pp. 6148-6160, 1998

[167] B. H. Armstrong, "Spectrum line profiles: the Voigt function," *J. Quant. Spectrosc. Radiat. Transfer,* vol. 7, pp. 61-88, 1967.

[168] D. Posener, "The Shape of Spectral Lines: Tables of the Voigt Profile," *Australian Journal of Physics,* vol. 12, pp. 184, 1959.

[169] B. D. Bartolo, *Optical Interactions in Solids*: Wiley, New York, 1968.

[170] P. G. Klemens, "Anharmonic Decay of Optical Phonons," *Physical Review,* vol. 148, no. 2, pp. 845-848, 1966.

[171] S. Gokden, R. Baran, N. Balkan *et al.*, "The effect of interface roughness scattering on low field mobility of 2D electron gas in GaN/AlGaN heterostructure," *Physica E: Low-dimensional Systems and Nanostructures,* vol. 24, no. 3-4, pp. 249-256, 2004.

[172] C. E. Martinez, N. M. Stanton, A. J. Kent *et al.*, "Energy relaxation by hot 2D electrons in AlGaN/GaN heterostructures: the influence of strong impurity and defect scattering," *Semiconductor Science and Technology*, no. 12, pp. 1580, 2006.

[173] B. K. Ridley, B. E. Foutz, and L. F. Eastman, "Mobility of electrons in bulk GaN and Al_{x}Ga_{1-x}N/GaN heterostructures," *Physical Review B,* vol. 61, no. 24, pp. 16862, 2000.

[174] T. Kozawa, T. Kachi, H. Kano *et al.*, "Raman scattering from LO phonon-plasmon coupled modes in gallium nitride," *Journal of Applied Physics,* vol. 75, no. 2, pp. 1098-1101, 1994.

[175] B. K. Ridley, "The LO phonon lifetime in GaN," *J. Phys.: Condens. Matter,* vol. 8, no. 37, pp. L511-L513, 1996.

[176] K. T. Tsen, D. K. Ferry, A. Botchkarev *et al.*, "Time-resolved Raman studies of the decay of the longitudinal optical phonons in wurtzite GaN," *Applied Physics Letters,* vol. 72, no. 17, pp. 2132-2134, 1998.

[177] H. Siegle, G. Kaczmarczyk, L. Filippidis *et al.*, "Zone-boundary phonons in hexagonal and cubic GaN," *Physical Review B,* vol. 55, no. 11, pp. 7000-7004, 1997.

[178] K. A. Filippov, and A. A. Balandin, "The effect of the thermal boundary resistance on self-heating of AlGaN/GaN HFETs," *MRS Internet Journal of Nitride Semiconductor Research,* vol. 8, pp. 8, 2003.

[179] E. T. Swartz, and R. O. Pohl, "Thermal Boundary Resistance," *Review of Modern Physics,* vol. 61, no. 3, pp. 605-665, 1989.

[180] R. M. Costescu, M. A. Wall, and D. G. Cahill, "Thermal conductance of epitaxial interfaces," *Physical Review B,* vol. 67, pp. 054302, 2003.

[181] R. J. Stevens, A. N. Smith, and P. M. Norris, "Measurement of Thermal Boundary Conductance of a Series of Metal-Dielectric Interfaces by the Transient Thermoreflectance Technique," *Journal of Heat Transfer,* vol. 127, no. 3, pp. 315, 2005.

[182] R. J. Stoner, and H. J. Maris, "Kaptiza Conductance and heat flow between solids at temperatures from 50 to 300 K," *Physical Review B,* vol. 48, no. 22, pp. 16373-16387, 1993.

[183] S. R. Phillpot, P. K. Schelling, and P. Keblinski, "Interfacial thermal conductivity: Insights from atomic level simulation," *Journal of Materials Science,* vol. 40, no. 12, pp. 3143, 2005.

[184] R. J. Stevens, P. M. Norris, and L. V. Zhigilei, "Molecular-Dynamics Study of Thermal Boundary Resistance: Evidence of Strong Inelastic Scattering Transport Channels." pp. IMECE2004-60334.

[185] C.-J. Twu, and J.-R. Ho, "Molecular-dynamics study of energy flow and the Kapitza conductance across an interface with imperfection formed by two dielectric thin films," *Physical Review B,* vol. 67, pp. 205422, 2003.

[186] P. E. Phelan, "Application of diffuse mismatch theory to the prediction of thermal boundary resistance in thin-film high-T/sub c/ superconductors," *Transactions of the ASME. Journal of Heat Transfer,* vol. 120, no. 1, pp. 37, 1998.

[187] R. S. Prasher, and P. E. Phelan, "A scattering-mediated acoustic mismatch model for the prediction of thermal boundary resistance," *Transactions of the ASME. Journal of Heat Transfer,* vol. 123, no. 1, pp. 105, 2001.

[188] P. Reddy, K. Castelino, and A. Majumdar, "Diffuse mismatch model of thermal boundary conductance using exact phonon dispersion," *Applied Physics Letters,* vol. 87, no. 21, pp. 211908, 2005.

[189] B. Abeles, "Lattice Thermal Conductivity of disordered semi-conductor materials at high temperature," *Physical Review,* vol. 131, no. 5, pp. 1906-1911, 1963.

[190] A. Majumdar, and P. Reddy, "Role of electron-phonon coupling in thermal conductance of metal-nonmetal interfaces," *Applied Physics Letters,* vol. 84, no. 23, pp. 4768, 2004.

[191] P. Hopkins, and P. Norris, "Thermal boundary conductance response to a change in Cr/Si interfacial properties," *Applied Physics Letters,* vol. 89, no. 13, pp. 131909, 2006.

[192] P. E. Hopkins, P. M. Norris, and R. J. Stevens, "Influence of Inelastic Scattering at Metal-Dielectric Interfaces," *Journal of Heat Transfer,* vol. 130, no. 2, pp. 022401, 2008.

[193] J. L. Hostetler, A. N. Smith, D. M. Czajkowsky *et al.*, "Measurement of the electron-phonon coupling factor dependence on film thickness and grain size in Au, Cr, and Al," *Applied Optics,* vol. 38, no. 16, pp. 3614-3620, 1999.

[194] A. Christensen, and S. Graham, "Heat Dissipation in GaN Power Semiconductor Devices," *Proceedings of IMECE '04: 2004 International Mechanical Engineering Conference and Exposition*, no. IMECE 2004-61525, 2004.

[195] A. Christensen, S. Graham, and W. Doolittle, "Heat Dissipation in High Power GaN Electronics on Thermally Resistive Substrates," *IEEE transactions on electron devices,* vol. 52, no. 8, pp. 1683, 2005.

[196] Intel, "First the Tick, Now the Tock: Next Generation Intel® Microarchitecture (Nehalem)," 2008.

[197] N. Fang, H. Lee, C. Sun *et al.*, "Sub-Diffraction-Limited Optical Imaging with a Silver Superlens," *Science,* vol. 308, no. 5721, pp. 534-537, April 22, 2005, 2005.

[198] It would be a deficiency if I did not properly acknowledge Patrick Hopkins for his indispensable part in properly identifying this point.

[199] H. Kim, V. Tilak, B. M. Green *et al.*, "Degradation characteristics of AlGaN-GaN high electron mobility transistors." pp. 214-218.

[200] Y. Liu, J. A. Bardwell, S. P. McAlister *et al.*, “Bias Stress Measurements on High Performance AlGaN/GaN HFET Devices,” *physica status solidi (a),* vol. 188, no. 1, pp. 233-237, 2001.

[201] J. Zou, D. Kotchetkov, A. A. Balandin *et al.*, "The effect of defects and dopants on thermal conduction in GaN films," *Materials Research Society Symposium - Proceedings.* p. 481.

[202] H. Kim, R. M. Thompson, V. Tilak *et al.*, “Effects of SiN passivation and high-electric field on AlGaN-GaN HFET degradation,” *Electron Device Letters, IEEE,* vol. 24, no. 7, pp. 421-423, 2003.

[203] A. P. Edwards, J. A. Mittereder, S. C. Binari *et al.*, “Improved reliability of AlGaN-GaN HEMTs using an NH/sub 3/ plasma treatment prior to SiN passivation,” *Electron Device Letters, IEEE,* vol. 26, no. 4, pp. 225-227, 2005.

[204] D. Pavlidis, P. Valizadeh, and S. H. Hsu, “AlGaN/GaN High Electron Mobility Transistor (HEMT) Reliability,” in 13th GaAs Symposium, Paris, France, 2005, pp. 265-268.

[205] A. Sozza, C. Dua, E. Morvan *et al.*, “A 3000 hours DC Life Test on AlGaN/GaN HEMT for RF and microwave applications,” *Microelectronics and Reliability,* vol. 45, no. 9-11, pp. 1617-1621, 2005.

[206] P. Valizadeh, and D. Pavlidis, “Investigation of the impact of Al mole-fraction on the consequences of RF stress on Al/sub x/Ga/sub 1-x/N/GaN MODFETs,” *Electron Devices, IEEE Transactions on,* vol. 52, no. 9, pp. 1933-1939, 2005.

[207] R. Coffie, Y. C. Chen, I. Smorchkova *et al.*, "Impact of A1N Interalayer on Reliability of AlGaN/GaN HEMTS." pp. 99-102.

[208] S. Singhal, J. C. Roberts, P. Rajagopal *et al.*, "GaN-ON-Si Failure Mechanisms and Reliability Improvements." pp. 95-98.

[209] A. Sozza, A. Curutchet, C. Dua *et al.*, “AlGaN/GaN HEMT Reliability Assessment by means of Low Frequency Noise Measurements,” *Microelectronics and Reliability,* vol. 46, no. 9-11, pp. 1725-1730, 2006.

[210] R. Coffie, Y. Chen, I. P. Smorchkova *et al.*, "Temperature and Voltage Dependent RF Degradation Study in Algan/gan HEMTs." pp. 568-569.

[211] A. M. Conway, M. Chen, P. Hashimoto *et al.*, "Accelerated RF life Testing of Gan Hfets." pp. 472-475.

[212] M. Faqir, G. Verzellesi, F. Fantini *et al.*, “Characterization and analysis of trap-related effects in AlGaN-GaN HEMTs,” *Microelectronics Reliability,* vol. 47, no. 9-11, pp. 1639-1642, 2007.

[213] P. Saunier, C. Lee, A. Balistreri *et al.*, "Progress in GaN Performances and Reliability." pp. 35-36.

[214] C. P. Wen, "Proposed GaN HFET current collapse mechanism," in Microwave Conference Proceedings, 2005. APMC 2005. Asia-Pacific Conference Proceedings, 2005, pp. 4 pp.

[215] R. Vetury, N. Q. Zhang, S. Keller *et al.*, "The impact of surface states on the DC and RF characteristics of AlGaN/GaN HFETs," *Electron Devices, IEEE Transactions on,* vol. 48, no. 3, pp. 560-566, 2001.

[216] U. Chowdhury, J. L. Jimenez, C. Lee *et al.*, "TEM Observation of Crack- and Pit-Shaped Defects in Electrically Degraded GaN HEMTs," *Electron Device Letters, IEEE,* vol. 29, no. 10, pp. 1098-1100, 2008.

[217] R. P. Feynman, "There's plenty of room at the bottom [data storage]," *Microelectromechanical Systems, Journal of,* vol. 1, no. 1, pp. 60-66, 1992.

[218] C. A. Arguello, D. L. Rousseau, and S. P. S. Porto, "First-Order Raman Effect in Wurtzite-Type Crystals," *Physical Review,* vol. 181, no. 3, pp. 1351, 1969.

[219] J. M. Hayes, "Raman Scattering in GaN, AlN, and AlGaN: Basic Material Properties, Processing, and Devices," PhD, University of Bristol, 2002.